

*Alma Mater Studiorum – Università di Bologna*

**DOTTORATO DI RICERCA IN  
INGEGNERIA ENERGETICA, TERMO-MECCANICA E  
NUCLEARE**

**Ciclo XXVII**

**Settore Concorsuale di afferenza: 09/C2**

**Settore Scientifico disciplinare: ING-IND/18**

**Improvement of photon transport model  
by including coupled photon-electron  
transport and kernel refinement**

Presentata da

**Eugenio Di Giulio**

Coordinatore Dottorato

Tutor

**Prof. Vincenzo Parenti Castelli   Prof. Jorge Eduardo Fernandez**

**Esame finale anno 2015**



# Table of contents

Introduction.....	6
1 Inverse problem solution in X-ray spectrometry process.....	10
1.1 MAXED unfolding method.....	14
1.2 GRAVEL unfolding method.....	16
1.3 UMESTRAT operative strategy.....	18
1.4 UMESTRAT interface.....	21
1.4.1 Input mode tab.....	21
1.4.2 Measured spectrum tab.....	22
1.4.3 Detector response tab.....	23
1.4.4 Chi-square tab.....	24
1.4.5 Default spectrum tab.....	26
1.4.6 Unfolding MAXED tab.....	30
1.4.7 UMESTRAT plot window.....	32
1.5 UMESTRAT unfolding result.....	34

2 Kernel refinement in X-rays Boltzmann transport model.....	40
2.1 The Boltzmann scalar transport equation.....	42
2.2 Rayleigh single process kernel.....	44
2.3 Compton single process kernel.....	46
2.3.1 Compton scattering function in the Waller-Hartree approximation.....	48
2.3.2 Compton scattering function in the Impulse approximation.....	49
2.4 Photoelectric effect kernel.....	53
2.5 Atomic Relaxation process.....	55
2.6 XRF contribution from Compton ionization.....	56
2.6.1 Single shell Compton cross section.....	57
2.6.2 Single shell photoelectric cross section.....	76
2.6.3 Single shell photoelectric- Compton cross section ratio.....	80
2.7 XRF Compton ionization kernel refinement.....	102
3 Electrons' radiative contribution in X-ray transport processes.....	104
3.1 The Monte Carlo code PENELOPE.....	108
3.1.1 Inner shell impact ionization process.....	109
3.1.2 Bremsstrahlung process.....	112
3.2 The program KERNEL.....	114
3.2.1 KERNEL input files.....	116
3.2.2 KERNEL output files.....	120
3.3 Radiative contribution of inner shell impact ionization.....	124
3.4 Radiative contribution of bremsstrahlung.....	127
3.4.1 Bremsstrahlung spatial distribution.....	127
3.4.2 Bremsstrahlung angular distribution.....	128
3.4.3 Bremsstrahlung energy distribution.....	130
3.4.4 Bremsstrahlung new kernel.....	132
3.4.5 Application to a synchrotron experiment.....	135

Conclusion.....	141
Appendix A. The UMESTRAT files format.....	143
Bibliography.....	151
Other Ph.D. activities.....	161
Acknowledgments.....	165



# Introduction

Starting from the results obtained during my Master degree thesis, in the first part of this work it is approached the study of the inverse (or unfolding) problem solution in the X-ray spectroscopy field. The solution of this particular problem consists in recovering of the missing of information that affects the result of an X-ray spectrometry measurement. It is well known in fact that in any measurement process the detection system introduces a series of effects which modify the measured distributions. This interference causes a loss of information which can be partially recovered through the inverse problem solution. To solve this problem it is necessary to use some particularly unfolding methods. In this work it is developed an operative strategy which solves the unfolding problem by using the maximum entropy method. This technique allows the introduction of all the a priori known information on the solution, such as the positivity of the unfolded distribution. The developed strategy is based on a mixed use of the two codes MAXED and GRAVEL, and give also the possibility to have an indirect evaluation of the quality of the model used to describe the detector response function, giving a quantification of the consistency between the used detector response model and the measurement accuracy. It is developed the code UMESTRAT, which allows the application of the cited unfolding strategy in a semiautomatic way to any X-ray spectrometry measurement. UMESTRAT gives the possibility to introduce in an iterative way the complex input needed to solve the inverse problem, also giving a graphical representation of all the intermediate results of the unfolding computation.

The second part of this work deal with the improvement of the Boltzmann model used to describe a generic X-ray transport process, by studying some of the radiative interactions neglected in this model, and including these contributions in the Boltzmann equations system by characterize their interaction kernels. This part of the work it is divided in two sections: in a first stage it is studied the characteristic line emission due to Compton ionization processes; in a second stage it is characterized the bremsstrahlung radiative contribution due the secondary electrons generated during a generic X-ray transport process.

It is known that three main photon interactions processes are considered in the Boltzmann model: the Rayleigh scattering (which modify the direction of the interacting photon), the Compton scattering (which modify the direction and the energy of the interacting photon) and the photoelectric effect (in which the interacting photon is absorbed by the target). In this model, the photoelectric effect is traditionally considered as the only ionization interaction which involves the ejection of a secondary electron from the ionized shell. The created atomic vacancy is filled by an atomic relaxation process which can be radiative (by lead to the creation of a characteristic photons emission) or radiationless (leading to the ejection of an Auger electron). The X-ray fluorescence contribution due to Compton inner shell ionization is usually neglected in the Boltzmann model because of the Compton cross section reduced magnitude respect to the photoelectric one. In this work it is done an exhaustively description of the characteristic contribution due to the Compton ionization for the single atomic shells. The radiative contribution due to atomic relaxation processes involved after Compton ionization is studied by developing a deterministic code with which it is evaluated the energy dependences of the single shell Compton cross section for the shells K, L1, L2, L3, M1, M2, M3, M4 and M5 of all elements with Z from 11 to 92, in the energy range 1-1000 keV. It is evaluated the extend of the Compton correction in percentage respect to the photoelectrical ionization contribution, by using two different database to evaluate the single shell photoelectric cross section (the EPDL97 database and the McMaster database) proving that the XRF Compton contribution may introduce, in some special cases, a significant correction to the Boltzmann model. It is implemented a semi-empirical formula which allows to compute the energy values for which the XRF Compton correction is equal to a generic fixed values for a generic shell (from K to M5) of all the considered elements. Finally a new interaction kernel is developed for the characteristic lines emission which takes into account both of the Compton and photoelectric ionization processes, improving the precision of the photonic Boltzmann model used until now.

An additional limitation of the Boltzmann model consists into the impossibility to evaluate the radiative contributes due to the secondary electrons interactions involved in an X-ray transport process. Secondary electrons in fact are produced after any ionizing photon interaction such as the Compton scattering and photoelectric effect. These charged particles may contribute to the radiation field by producing X-rays through two main interaction processes: the inner shell impact ionization (in which the electron ionize the interacting atom creating an electronic vacancy filled through a relaxation process) and the bremsstrahlung (in which the electron produces a continuum radiative spectrum). To have a complete description of the radiative contribution generated by secondary electrons it would be necessary to use the coupled photon-electron transport equation model. However, the solution of this coupled problem is



really complex and time consuming because electrons interact continuously in the medium. For this reason the secondary electrons contribution is frequently neglected, causing a miss of information in the reconstruction of the radiative spectrum produced in a photon transport process. In this part of the work it is introduced a new photon transport model which comprise the bremsstrahlung contribution due to the coupled photon-electron transport process as external sources terms in the Boltzmann equation. The bremsstrahlung of secondary electrons it is studied, in a similar way as done for the inner shell impact ionization by Fernandez [Fernandez, 2014-2]. The main program KERNEL is adapted to simulate the coupled photon-electron transport by using the Monte Carlo code PENELOPE. The bremsstrahlung radiation is characterized in terms of space, angle and energy, for all elements whit  $Z=1-92$  and for a fixed set of photonic source energies in the range 1–150 keV. It is demonstrated that bremsstrahlung radiative contribution can be well approximated with an isotropic point photon source. The bremsstrahlung energetic contribution is characterized separately for each interaction from which the secondary electron is been created during an X-ray transport process. It is created data library comprising the energetic distributions of bremsstrahlung for a fixed set of source energies and for all elements with  $Z=1-92$ . For arbitrary energy values the contribution is computed using a 2D ad hoc interpolation method, giving optimal results. It is developed finally a new bremsstrahlung kernel which allows the introduction of this contribution in the modified Boltzmann equation through the use of the crated data library. The obtained results allow the refinement of the radiation field description by using a new pure photon transport model which allows the elimination of the computational costs and complexity typical of the solution of the coupled photon-electron problem.



# Chapter 1

## Inverse problem solution in X-ray spectrometry process

An X-ray spectrometry measurement consists in collecting the energy distribution of the outgoing radiation from an irradiated target, by using an X-ray detector. It is well known that the measured spectra differ from the original one because of additional phenomena introduced in the process by the detection system, causing a loss of information in the quantities of interest. To recover the original spectrum from the measured one it is necessary to remove the influence of the detector solving the so-called inverse (or unfolding) problem. The whole influences of the detector is quite complex to characterize and it is usually expressed as the convolution of different effects such as the radiation transport inside the detector, the energy resolution and all the contributions related to the signal formation and processing [Knoll, 2000] forming the detector response function (DRF).

Mathematically the measured intensity  $I(E)$  is related to the DRF  $R(E)$  and to the original spectrum  $f(E)$  through a convolution integral:

$$I(E) + \varepsilon(E) = \int R(E)f(E)dE \quad (1.1)$$

where  $\varepsilon(E)$  represents the (unknown) measurement error which depends on the measurement time and contains all the statistical errors of the measurement process.

The equation Eq. 1.1 can be discretized leading to the following linear equation system:

$$I_k + \varepsilon_k = \sum_{i=1}^n R_{i,k} f_i \quad \text{with} \quad k = 1, m \quad (1.2)$$

where  $m$  is the number of discrete energy bins. It is easy to see that Eq. 1.2 has a unique solution only if the number of channels  $m$  in the measurement is equal to the number of energy groups  $n$  considered in the original spectrum discretization, i. e. ( $m = n$ ).

Solving the unfolding problem also requires to estimate the measurement error  $\varepsilon_k$  by means, for instance, of some assumption about the counting statistic. Generally it is assumed that the measurement errors are normally distributed with zero mean and standard deviation  $\sigma_k$ . Thus, the chi-square per degree of freedom  $\chi^2$  can be introduced as follows:

$$\chi^2 = \frac{1}{n} \sum_{k=1}^m \left( \frac{\varepsilon_k}{\sigma_k} \right)^2 \quad (1.3)$$

The DRF is expressed as a ( $m \times n$ ) matrix operator where each column represents the discretized response for a unitary monochromatic excitation at the  $i$ -th energy channel. An example of a single column distribution for the DRF is shown in Fig. 1.1. An example of a schematic representation of the DRF is shown in Fig 1.2.

As shown in Fig 1.1 and Fig. 1.2 all the effects introduced by the detection system (the escape peaks, the Compton continuum and the detector resolution and efficiency) strongly modify the ideal DRF (a unitary diagonal matrix) causing the ill-conditioning of Eq. 1.2. Because of this ill-conditioning some specific deconvolution methods must be used to solve Eq. 1.2, like, for example, Fourier transform methods, least-squares methods, iterative methods, Tikhonov methods, maximum entropy methods, neural networks methods and Monte Carlo methods [Hussein, 2011]. Most of these are purely mathematical criteria and may lead to unphysical solutions, such as the presence of negative values in the intensity of the recovered spectrum. The maximum entropy technique is a deconvolution algorithm which solves the inverse problem by taking advantage of all the physical a priori information known on the considered spectrometry processes and ensuring in this way the conservation of some physical characteristic of the recovered spectrum such as the positive-defined character of its distribution.

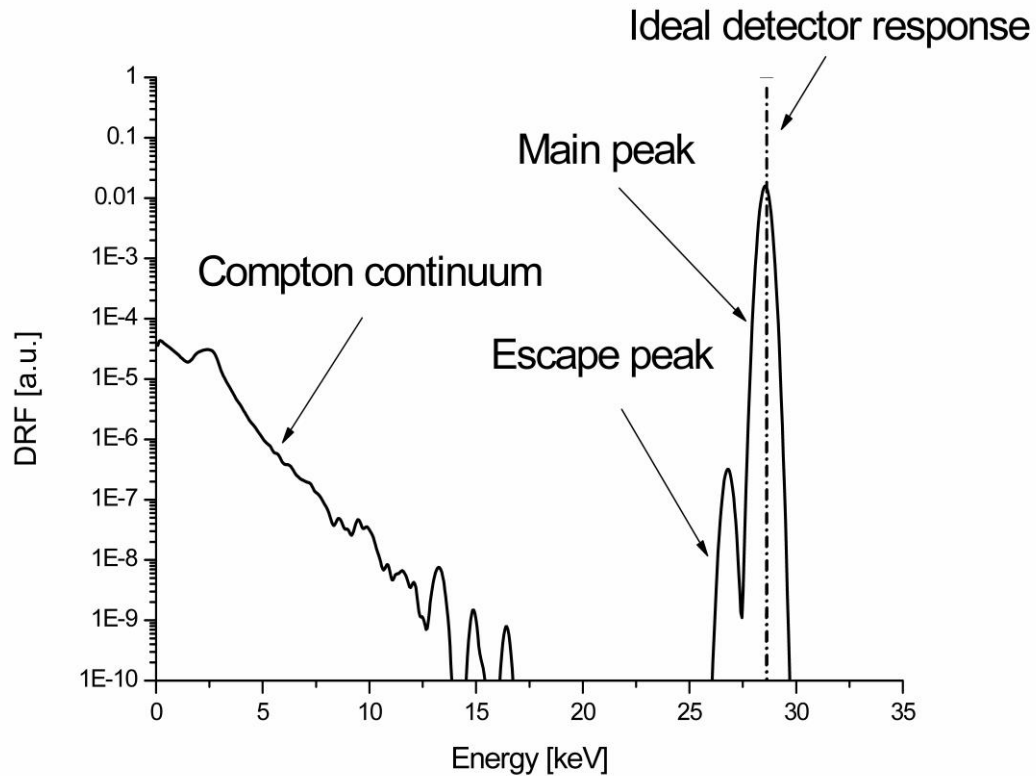


Fig. 1.1. Comparison between an ideal DRF (dash dot line), and the DRF of a Si-PIN detector (solid line) for a monochromatic source energy of 28.65 keV. The Si-PIN DRF is computed by using the two codes MCSHAPE e RESOLUTION [Fernandez, 2009], [Fernandez, 2014-3]. In the figure it is possible to see the different effects due to the detection system: the presences of the Compton continuum and the escape peak; the spread of the distribution due to the detector resolution; the decrease of the DRF intensity due to the detector efficiency.

The maximum entropy method is adopted in the deconvolution code MAXED (MAXimum Entropy Deconvolution) developed by Marcel Reginatto [Reginatto, 1999]. MAXED, together with GRAVEL, a deconvolution code based on an iterative method and developed by Manfred Matzke [Matzke, 2002], are contained in the UMG package (Unfolding with MAXED and GRAVEL) version 3.3 [Reginatto, 2003] released in March 2003 by the Physikalisch Technische Bundesanstalt (PTB) and distributed by NEA Data Bank. During my master thesis [Di Giulio, 2011] these two codes have been used together to study the solution of the inverse problem solution in X-ray spectrometry, giving good results. In particular it was shown that MAXED is capable to remove the detector influences from the measured spectrum conserving some physical characteristics of the expected original spectrum, but it needs some input parameter on the estimated deconvolution result accuracy which can be computed with GRAVEL.

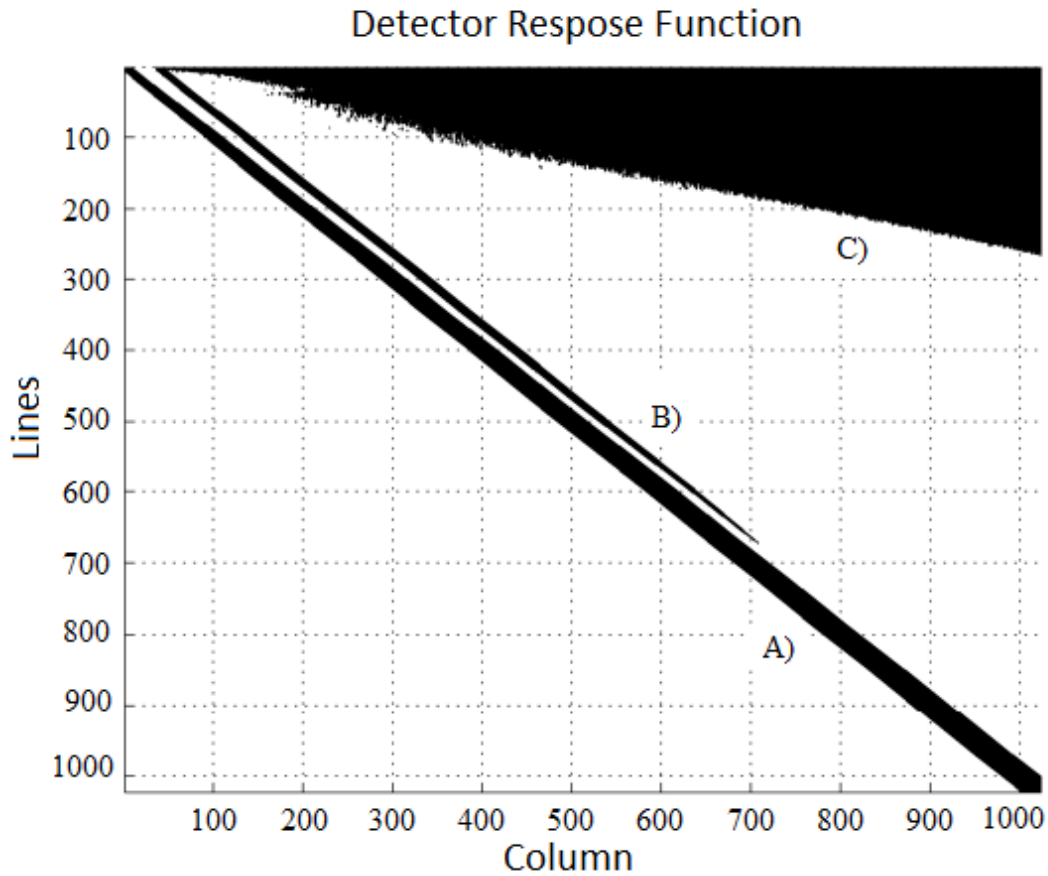


Fig. 1.2. Schematic representation of the DRF matrix for a Si-PIN detector where: A) the main diagonal is the full energy peak; B) the secondary diagonal is due to the escape peaks; C) is the Compton continuum.

During the first part of my Ph.D. an unfolding strategy to the inverse problem by using a suitable combination of the codes MAXED and GRAVEL was developed and implemented in the code UMESTRAT (Unfolding Maximum Entropy STRATegy). In what follows the strategy used by UMESTRAT is presented together with a brief description of the regularization techniques used by MAXED and GRAVEL. An example of the applications of UMESTRAT to X-ray measurement is shown.

## 1.1 MAXED unfolding method

The code MAXED (developed by Marcel Reginatto) represents the state of art for unfolding of neutron spectra [Reginatto, 1999]. This code solves the inverse problem by using the maximum entropy regularization technique, a method widely used in data analysis as a general and powerful technique for reconstructing positive distributions in situations where only incomplete information is available. In [Fernandez, 2014-1] MAXED was applied for the first time in X-ray spectrometry. The maximum entropy technique solves the inverse problem by imposing a set of physical constraints introduced through the so-called Cross Entropy equation.

$$S = - \sum_{i=1}^n \left[ f_i \ln \left( \frac{f_i}{f_i^{DEF}} \right) + (f_i^{DEF} - f_i) \right] \quad (1.4)$$

where  $f_i^{DEF}$  is the default spectrum which contains all the a priori information on the searched original spectrum. The Cross Entropy is always  $S \leq 0$  for every  $f_i$ , and the condition  $S = 0$  is verified only when the original spectrum reconstruction is equal to the default spectrum.

By introducing this constraint, the inverse problem solution turns into the following task: reconstruct an original spectrum distribution which solves the convolution system Eq. 1.2, by maximizing the Cross Entropy in Eq. 1.4 with constraints given by Eq. 1.3. This can be done by using the Lagrange multipliers equation:

$$L(f_i, \varepsilon_k, \lambda_k, \mu) = - \sum_{i=1}^n \left[ f_i \ln \left( \frac{f_i}{f_i^{DEF}} \right) + (f_i^{DEF} - f_i) \right] - \sum_{k=1}^m \lambda_k \left[ \sum_{i=1}^n R_{i,k} f_i - I_k - \varepsilon_k \right] - \mu \sum_{k=1}^m \left[ \left( \frac{\varepsilon_k}{\sigma_k} \right)^2 - \chi^2 \right] \quad (1.5)$$

where  $\lambda_k$  and  $\mu$  are  $(m + 1)$  Lagrange multipliers. Solving the Eq. 1.5 is equivalent to maximizing the potential function

$$Z = - \sum_{i=1}^n \left\{ f_i^{DEF} \cdot \exp \left[ - \sum_{k=1}^m (\lambda_k R_{i,k}) \right] \right\} - \mu \left[ \chi^2 \cdot \sum_{k=1}^m (\lambda_k \sigma_k)^2 \right]^{\frac{1}{2}} - \sum_{k=1}^m \lambda_k I_k \quad (1.6)$$

with respect to the Lagrange Multipliers  $\lambda_k$ .

Eq. 1.6 is maximized in MAXED by using an iterative L-BFGS-B algorithm (Limited memory software Broyden–Fletcher–Goldfarb–Shanno for large-scale Bound-constrained optimization) [Byrd, 1995]. In the maximum entropy method, using good a priori information is then a crucial point of the unfolding process, since the default spectrum distribution participate in all the computational steps of the iteration method. The chi-square per degree of freedom of the unfolded solution is evaluated at each  $j$ -th iterative step though the equation

$$(\chi^2)^j = \frac{1}{n} \sum_{k=1}^m \frac{\{I_k - \sum_{i=1}^n R_{i,k} \cdot f_i^j\}^2}{\sigma_k^2} \quad (1.7)$$

The built-in stop conditions for the code are the maximum number of iterative steps or the minimum chi-square per degree of freedom reached by the unfolded solution.



## 1.2 GRAVEL unfolding method

The code GRAVEL, written by Manfred Matzke [Matzke, 2002], is a modified version of the unfolding code SAND-II [McElroy, 1967]. This code solves the inverse problem by using a special iterative method aimed to minimize the chi-square per degree of freedom of the unfolded solution and imposing positivity of the recovered distribution. In order to impose the positivity of the inverse problem solution, Eq. 1.2 and Eq. 1.3 are reformulated in GRAVEL as

$$\begin{cases} I_k + \varepsilon_k = \sum_{i=1}^n R_{i,k} \cdot \exp[\ln(f_i)] \\ \chi^2 = \frac{1}{n} \sum_{k=1}^m \frac{\{I_k - \sum_{i=1}^n R_{i,k} \cdot \exp[\ln(f_i)]\}^2}{\sigma_k^2} \end{cases} \quad (1.8)$$

The inverse problem solution  $f_i$ , at the  $(j + 1)$ -the iteration is computed through the iterative equation

$$f_i^{j+1} = f_i^j \exp \left[ \frac{\sum_{k=1}^m W_{i,k}^j \cdot \ln \left( \frac{I_k}{\sum_{i'=1}^n R_{i',k} f_{i'}^j} \right)}{\sum_{k=1}^m W_{i,k}^j} \right] \quad (1.9)$$

where  $W_{i,k}^j$  is a weight function defined as

$$W_{i,k}^j = \frac{R_{i,k} f_i^j}{\sum_{i'=1}^n R_{i',k} f_{i'}^j} \cdot \left( \frac{I_k}{\sigma_k} \right)^2 \quad (1.10)$$

By means of Eq. 1.9, GRAVEL reaches an unfolding solution characterized by a positive distribution with a chi-square which is lower and lower as the number of iterative steps increases. The a priori information contained in the default spectrum  $f_i^{DEF}$  is used in GRAVEL only in the first iteration by setting  $f_i^1 = f_i^{DEF}$ . The built-in stop conditions for the code are the maximum number of iterative steps or the minimum chi-square per degree of freedom reached by the unfolded solution.

### 1.3 UMESTRAT operative strategy

As shown in the previous sections 1.2 and 1.3, both MAXED and GRAVEL use as input parameters the measured spectrum ( $f_i$ ) with its variance ( $\sigma_k$ ), the computed DRF ( $R_{i,k}$ ) and an estimate of the unfolding solution called default spectrum ( $f_i^{DEF}$ ) which contains the a priori information known about the considered X- spectrum. The a priori information contained in the default spectrum is used in each code in a different way: while MAXED considers the default spectrum in every computational step, GRAVEL uses it only as initial value for the first iteration. Additional input parameters used by the codes as built-in stop condition are the maximum number of iterations and the desired precision of the solution defined by the requested final value of the chi-square per degree of freedom ( $\chi^2$ ). The classical input format of both codes is shown in Appendix A. For more details about the unfolding algorithm and the input file format used in both MAXED and GRAVEL, see the UMG package manual [Reginatto, 2003].

In my master degree thesis [Di Giulio, 2011], it was show that both MAXED and GRAVEL solves the unfolding problem in X-ray spectrometry giving good results and that the a priori information introduced by the default spectrum is preserved in the MAXED results. However it was seen that an incorrect value of the chi-square per degree of freedom in MAXED leads to meaningless results (or no results at all). This problem is due to the consistency between the used DRF and the measurement accuracy. It is assumed in fact that the DRF error is comprised within the measurement error. If the used measurement is too accurate, its variance cannot contain the DRF error. It was demonstrated that the inverse problem solved by GRAVEL always provides a suitable estimate of the reachable minimum of the chi-square per degree of freedom, giving also an indirect evaluation of the DRF goodness.

Starting from these results, it is developed a new operative strategy which allows the solution of the unfolding problem in X-ray spectrometry by using a suitable combination of MAXED and GRAVEL. The main aim of this strategy is to optimize the introduction of the known a priori information, also assessing the convergence of the code to a physically significant result. For this purpose, the unfolding code UMESTRAT (Unfolding Maximum Entropy STRATegy), a graphical tool which applies the implemented strategy in a semiautomatic way, is developed.

The UMESTRAT strategy consists in three main steps:

Step 1: GRAVEL is used to compute the initial value of the chi-square per degree of freedom in order to ensure the later convergence of MAXED, and to evaluate the DRF goodness. The unfolding procedure is solved using a positive unitary distribution as an initial default spectrum and, as build-in stop condition, a unitary chi-square per degree of freedom. The maximum number of iterations can be chosen by the user. The indirect evaluation of the DRF fitness is done by computing the so called mean relative error defined as

$$\varepsilon_r = \frac{\sqrt{\chi^2 \sigma^2}}{I_m} \quad (1.11)$$

where  $I_m$  is the main number of counts of the measured spectrum. If this value is too high, the measurement error can be amplified by using an amplification factor and the GRAVEL computation can be repeated.

Step 2: MAXED is used together with a selective smoothing process to build an optimized default spectrum. The unfolding procedure is solved using a positive unitary distribution as an initial default spectrum and, as build-in stop condition, the unitary chi-square per degree of freedom found at step 1. This default spectrum can be improved by cleaning the noise by means of a selective smoothing process. Smoothing in selected region of interest (ROI) can use alternatively a Savitzky-Golay filter [Press, 1996] or a moving average filter [Press, 1996]. ROI selection is done interactively by the user. The cleaned default spectrum is used in the next step.

Step 3 The final solution is computed with MAXED by using the final chi-square per degree of freedom obtained in step 1 and the optimal default spectrum obtained in step 2.

A flowchart of the described strategy is shown in Fig 1.3.

## UMESTRAT Operative Strategy

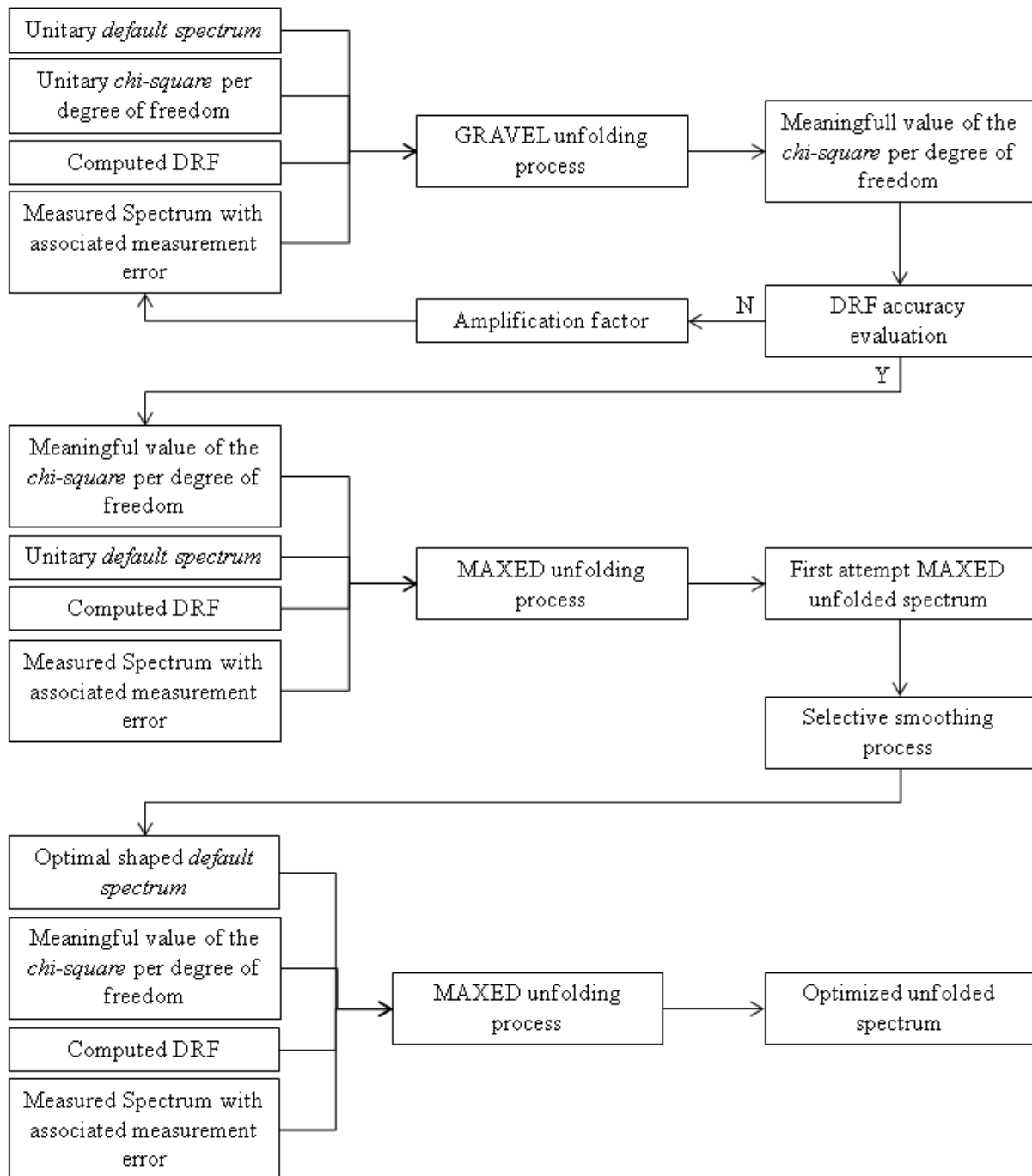


Fig. 1.3. Flowchart of the UMESTRAT operative strategy

## 1.4 UMESTRAT interface

The UMESTRAT interface it is developed in FORTRAN 90/95 by using the graphical library Winteracter (*Interactive Software Services Ltd.*). The UMESTRAT code is composed by 6 tabs, each one for a specific computational stage.

### 1.4.1 Input mode tab

The tab “**Input Mode**” is the first tab of the UMESTRAT interface. In this tab the user can choose whether to start a new work or load the input file of a previous computation. A screenshot of this first tab is shown below in Fig 1.4.

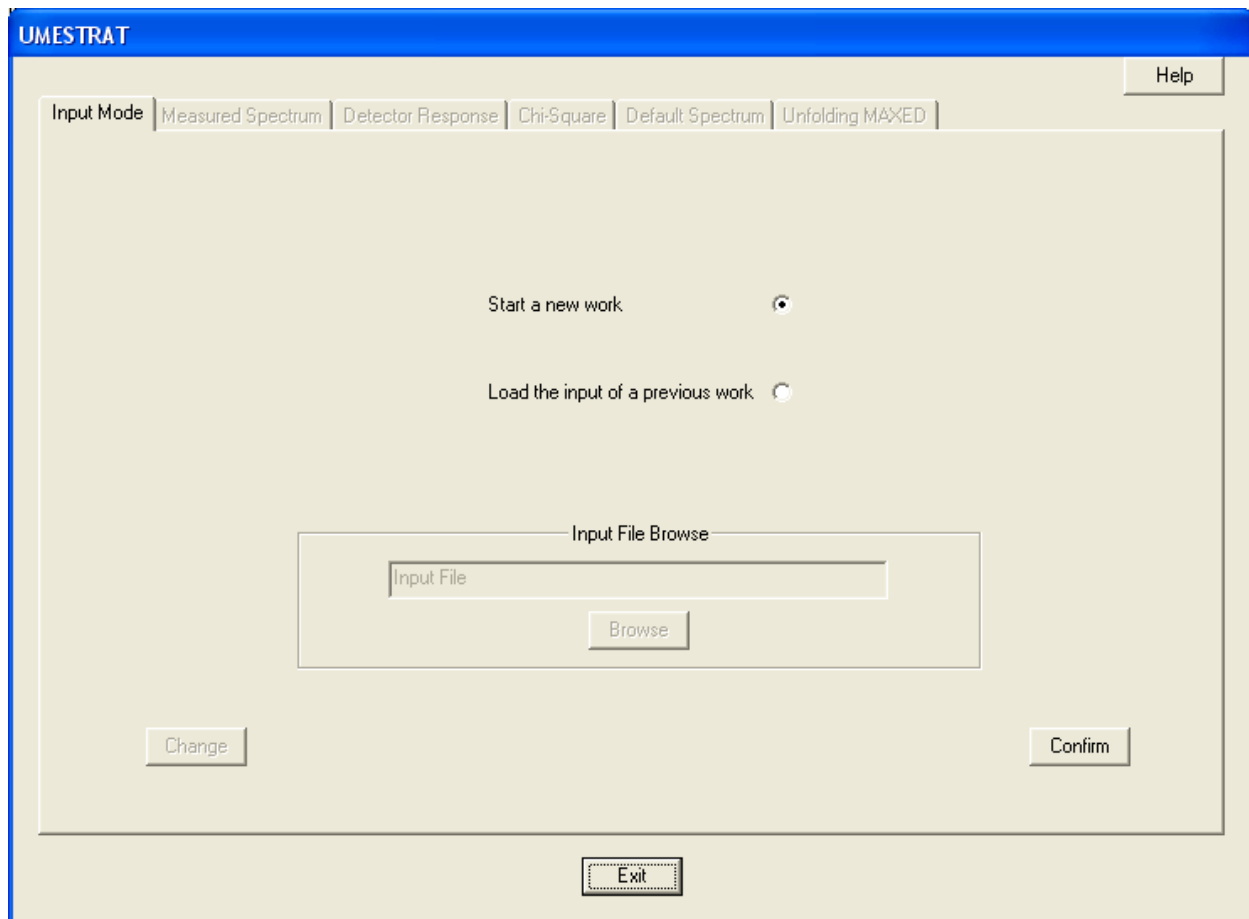


Fig 1.4. Screenshot of the code UMESTRAT, “**Input Mode**” tab.

In this tab, if the user wants to start a new work he has to:

1. Check the radio button “**Start a new work**”.
2. Click on the “**Confirm**” button to enable the next tab “**Measured Spectrum**” and continue with the UMESTRAT computation.

If the user wants to load the input file of a previous work, he has to:

1. Check the radio button “**Load the input of a previous work**”.
2. Click on the “**Browse**” button in the “**Input File Browse**” section to load the file of a previous work. This is a specific file in the “.ume” format which can be created at the end of the UMESTRAT computation (a description of this file is shown in Appendix A).
3. Click on the “**Continue**” button to enable all the code tabs and load the data of the selected previous work inside the code.

The “**Change**” button allows to steps back to the choice of the input mode selection.

## 1.4.2 Measured spectrum tab

The tab “**Measured Spectrum**” is the second tab of the UMESTRAT interface. In this tab the user can load the measurement data file. A screenshot of this first tab is shown below in Fig 1.5. Two file formats are available, the “.phs” file format [Reginatto, 2003] (the file format used by MAXED and GRAVEL) and the “.mca” file format (multichannel analyzer output).

If the user wants to load the measurement data in the “.phs” format, he has to:

1. Check the “**File phs**” radio button in the “**Measured Spectrum File**” section.
2. Click on the “**Browse**” button in the “**Meas File Browse**” section to load the “.phs” desired file.
3. Click on the “**Confirm**” button to enable the next tab “**Detector Response**” and continue with the UMESTRAT computation.

If the user wants to load the measurement data in the “.mca” file format, he has to:

1. Check the “**File mca**” radio button in the “**Measured Spectrum File**” section.
2. Insert the calibration parameters in the “**Calibration Parameters**” section.
3. Click the “**Confirm Parameters**” button in the “**Calibration Parameters**” section to confirm the entered values for the calibration parameters (the “**Change Parameters**” button allows to step back to the choice of the calibration parameters).
4. Click on the “**Browse**” button in the “**Meas File Browse**” section to load the “.mca” desired file.
5. Click on the “**Confirm**” button to enable the next tab “**Detector Response**” and continue with the UMESTRAT computation.

The “**Change**” button allows to steps back to the choice of the measurement data file to load. The “**View Meas File**” button allows to views a graphical representation of the loaded measured file data.

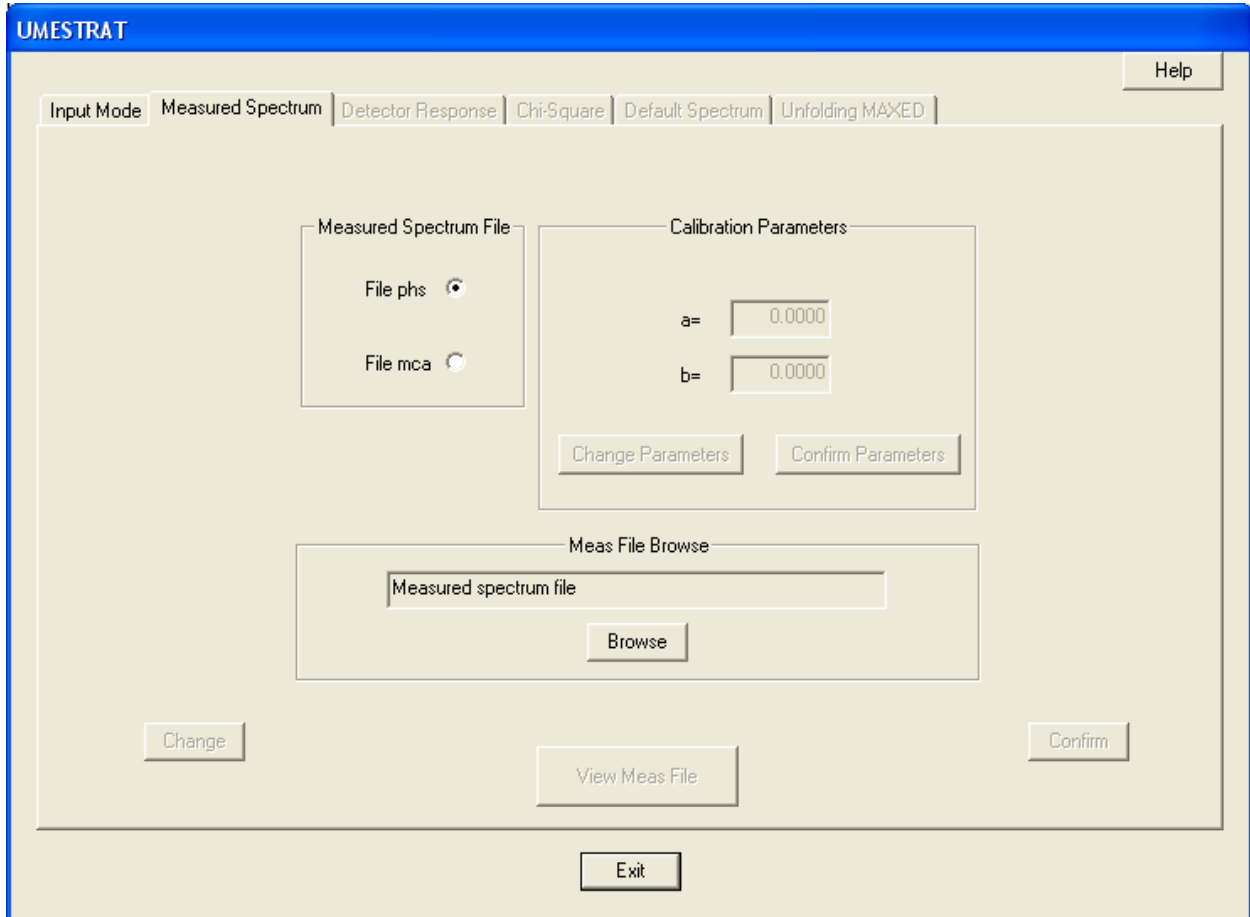


Fig 1.5. Screenshot of the code UMESTRAT, “**Measured Spectrum**” tab.

### 1.4.3 Detector response tab

The “**Detector Response**” tab is the third tab of the UMESTRAT interface. In this tab the user can load the detector response matrix file. A screenshot of this tab is shown in Fig 1.6. The detector response function file must be in the “.rsp” file format [Reginatto, 2003] (the file formats used by MAXED and GRAVEL). To load the DRF matrix file the user has to:

1. Click on the “**Browse**” button in the “**Detector File Browse**” section to load the “.rsp” desired file.
2. Click on the “**Confirm**” button to enable the next tab “**Chi-Square**” and continue with the UMESTRAT computation.



The “**Change**” button allows to steps back to the choice of the DRF data file to load.

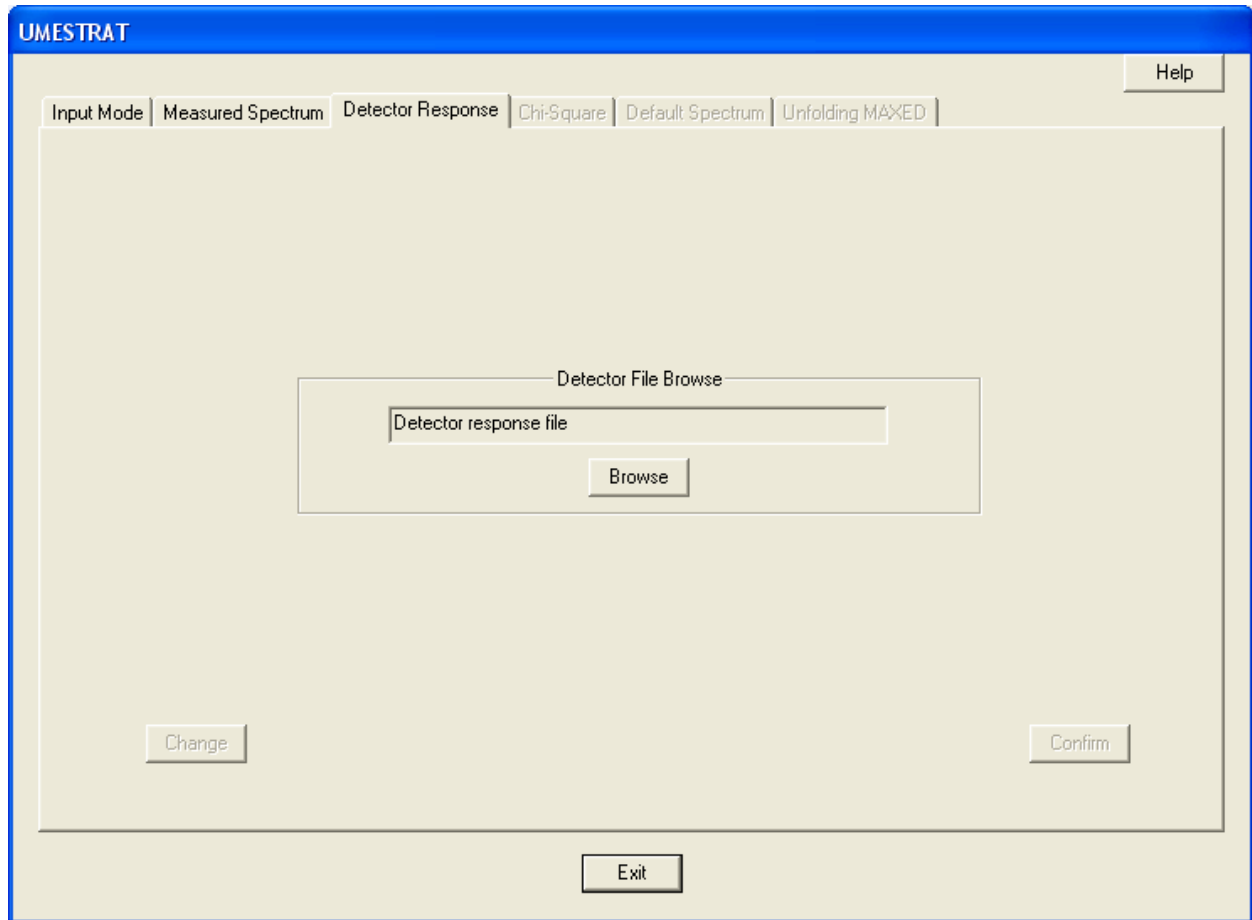


Fig 1.6. Screenshot of the code UMESTRAT, “**Detector Response**” tab.

#### 1.4.4 Chi-square tab

The tab “**Chi-Square**” is the fourth tab of the UMESTRAT interface. This tab allows to compute the initial value of the chi-square per degree of freedom in order to ensure the later convergence of MAXED, also giving an evaluation of the DRF accuracy. The code GRAVEL is used for this purpose. The unfolding procedure is solved using a positive unitary distribution as default spectrum and, as built-in stop condition, a unitary chi-square per degree of freedom. A screenshot of this tab is shown in Fig 1.7.

In this tab, the user has to:

1. Insert the data input for the GRAVEL computation [Reginatto, 2003] in the “**GRAVEL input**” section which comprise: the “**Maximum Number of GRAVEL Iterations**”, the

“**Frequency of Intermediate GRAVEL Iterative Steps**”, the “**Name of GRAVEL Output**” file and the “**Amplification Factor for the Standard Deviation**”.

2. Click on the “**Confirm Input**” button to confirm the entered values of the GRAVEL input.
3. Click on the “**Compute Chi-Square**” button to start the GRAVEL computation and wait until the calculation is over.

Once finished the calculation step with GRAVEL, is possible to perform the evaluation of the DRF fitness trough the main relative error as expressed in Eq. 1.11:

1. If this value is acceptable the user can click on the “**Confirm**” button to enable the next tab “**Default Spectrum**” and continue with the UMESTRAT computation.
2. If the obtained mean relative error is too high the user can click on the “**Change Input**” button and repeat the GRAVEL computation changing the used amplification factor.

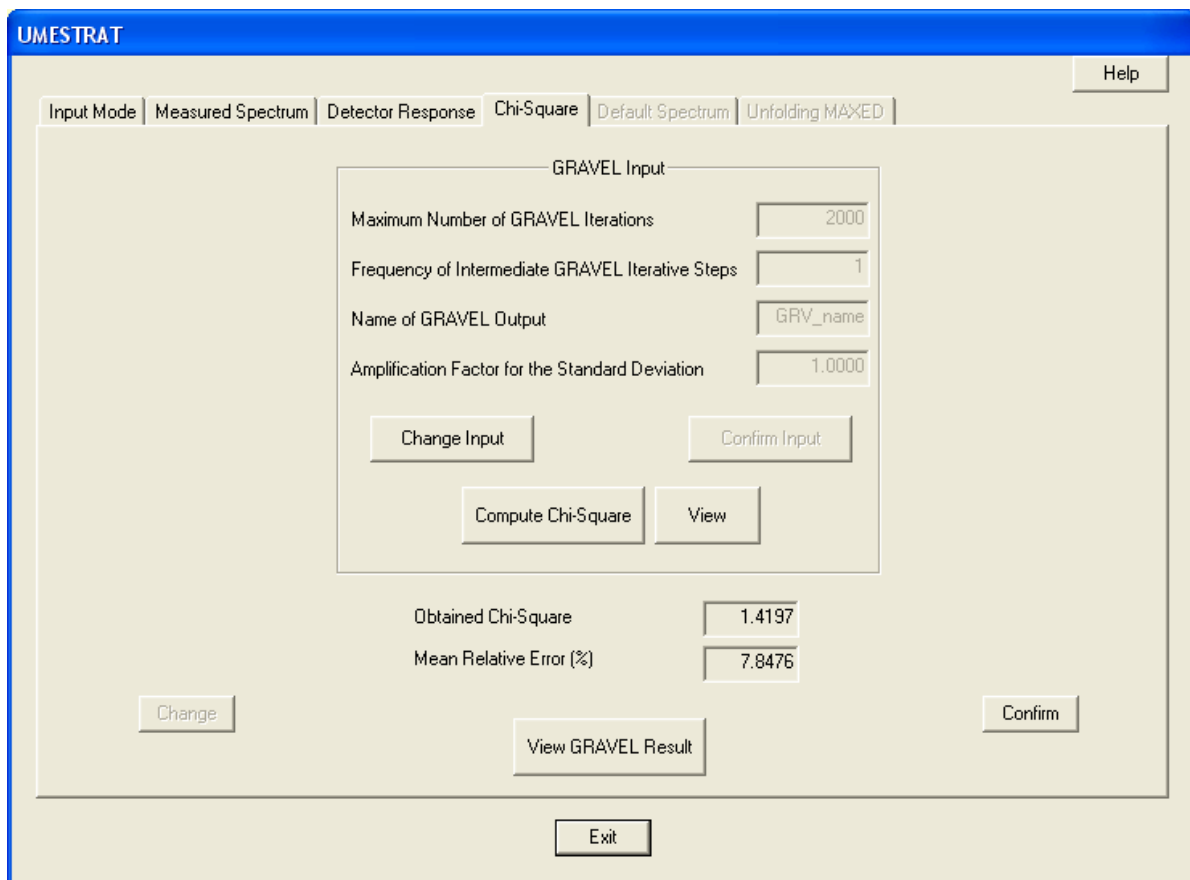


Fig 1.7 Screenshot of the code UMESTRAT, “**Chi-Square**” tab.

The “**View**” button opens the report file of the GRAVEL computation. The “**Change**” button allows to steps back to the computation of the chi-square per degree of freedom with GRAVEL. The “**View GRAVEL Results**” button allows to views a graphical representation of the unfolded spectrum obtained with GRAVEL.

### 1.4.5 Default spectrum tab

The tab “**Default Spectrum**” is the fifth tab of the UMESTRAT interface. In this tab the user can load or build an optimally shaped default spectrum. The code MAXED together with a selective smoothing process is used for this purpose. The unfolding procedure is solved using, as built-in stop condition, the chi-square per degree of freedom found in the “**Chi-Square**” tab. A screenshot of this tab is shown in Fig 1.8. The default spectrum file must be in the “.flu” file format [Reginatto, 2003].

To load the default spectrum, the user has to:

1. Check the “**Browse Default Spectrum**” button in the “**Default Spectrum File**” section.
2. Click on the “**Browse**” button in the “**Default File Browse**” section to load the “.flu” desired file.
3. Click on the “**Confirm**” button to enable the next tab “**Unfolding MAXED**” and continue with the UMESTRAT computation.

To build the default spectrum, the user has to:

1. Check the “**Compute Default Spectrum**” radio button in the “**Default Spectrum File**” section
2. Insert the data input for the MAXED computation in the “**MAXED Input**” section which comprise: the “**Maximum Number of MAXED Iterations**” and the “**Name of MAXED Output**” file.
3. Click on the “**Confirm Input**” button to confirm the entered values of the MAXED input.
4. Click on the “**Compute Default Spectrum**” button to start the MAXED computation and wait until the calculation is over.

Once that the computation step with MAXED is finished, it is possible to choose if to use directly the obtained distribution or improve it by applying a selective smoothing procedure.

To use directly the obtained MAXED result, the user has to:

1. Click on the “**Use Directly the MAXED Result**” button to enable the “**Confirm**” button.
2. Click on the “**Confirm**” button to enable the next tab “**Unfolding MAXED**” and continue with the UMESTRAT computation.

To apply a selective smoothing procedure to the obtained MAXED result, the user has to:

1. Click on the “**Smooth the Default Spectrum**” button to open the “**Default Spectrum Smoothing**” window.
2. Apply the desired smoothing procedure in the “**Default Spectrum Smoothing**” window.
3. Click on the “**Confirm**” button to enable the next tab “**Unfolding MAXED**” and continue with the UMESTRAT computation.

The “**View**” button opens the report file of the MAXED computation. The “**Change**” button allows to steps back to the building process of the default spectrum. The “**View Default File**” button allows to view a graphical representation of the obtained optimally shaped default spectrum.

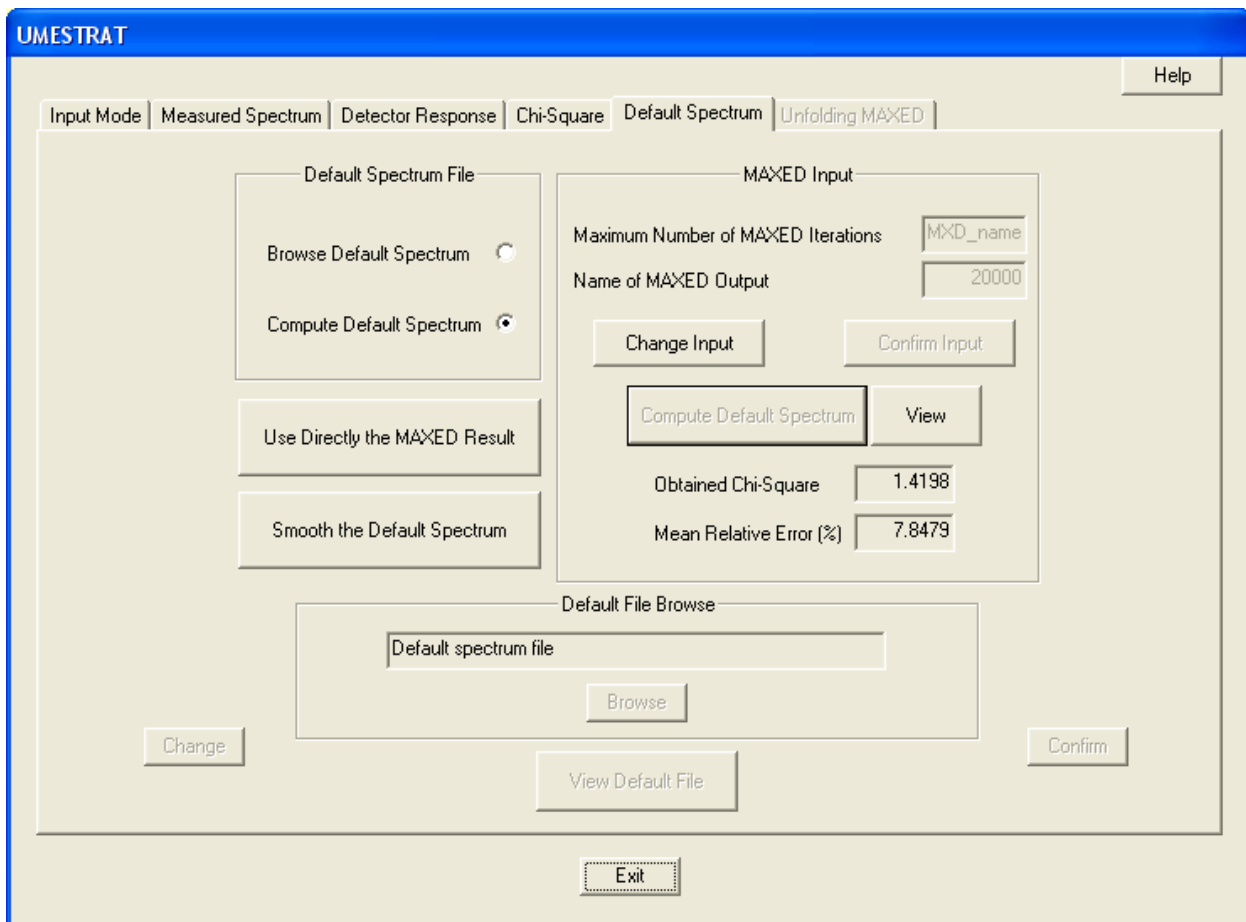


Fig 1.8 Screenshot of the code UMESTRAT, “**Default Spectrum**” tab.

The “**Default Spectrum**” window allows to apply a selective smoothing procedure to the MAXED result obtained in the “**Default Spectrum**” tab. The applied smoothing procedures are designed in order to clean the noise without changing the characteristics of the spectrum. The applied smoothing procedures can be either a moving average smoothing process [Press, 1996] or a Savitzky-Golay smoothing process [Press, 1996]. The Default Spectrum window is opened when the user clicks on the “**Smooth the Default Spectrum**” button in the “**Default Spectrum**” tab. A screenshot of this window is shown in Fig. 1.9.

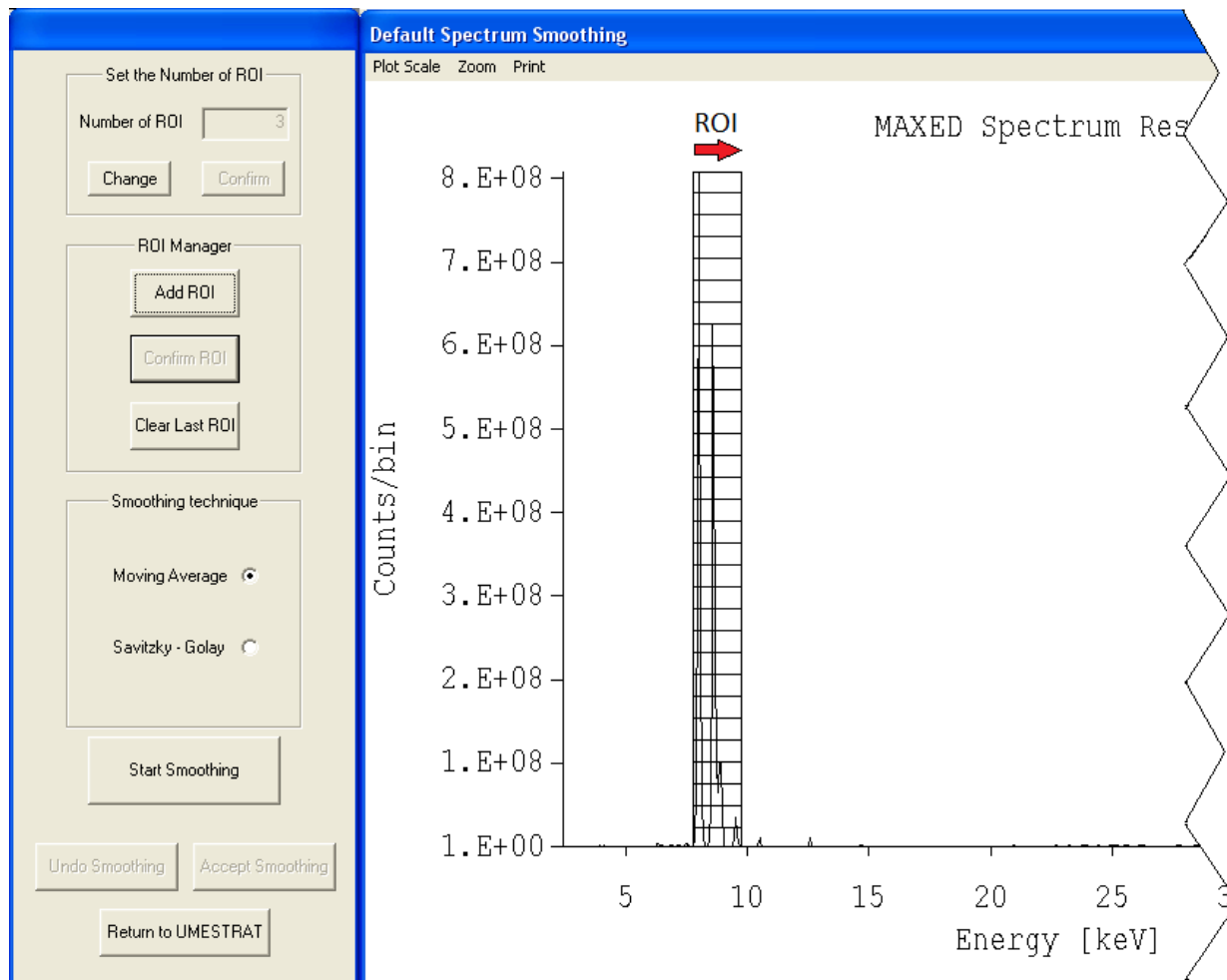


Fig. 1.9. Screenshot of the code UMESTRAT, “**Default Spectrum**” window.

To apply the selective smoothing procedures in the “**Default Spectrum**” window, the user has to:

1. Set the number of ROI in the “**Number of ROI**” string.
2. Click on the “**Confirm**” button to confirm the entered value of number of ROI (the “**Change**” button allows to step back to the setting of the Number of ROI).
3. Selecting interactively the desired ROI in the plot window, by means of the following steps:
  - a. Click on the “**Add ROI**” button in the “**ROI Manager**” section to enable the ROI selection cursors.
  - b. Select the desired ROI by directly clicking on the plot window (the selected ROI is highlighted in the plot window with a grid, as is shown in Fig. 1.9).
  - c. Click on the “**Confirm ROI**” button in the ROI Manager section to confirm the ROI selections (this selection procedure must be repeated for every ROI). The “**Clear Last ROI**” button deletes the last selected ROI.
4. Mark the desired smoothing technique in the “**Smoothing technique**” section.
5. Click on the “**Start Smoothing**” button to start the smoothing process.

Depending on the selected smoothing technique, it is possible to continue the smoothing application through two different ways:

1. If the user has selected the “**Moving Average**” radio button in the “**Smoothing technique**” section, the dialog “**Moving Average Smoothing Parameter**” will open. A screenshot of this dialog is shown in Fig. 1.10. In the opened dialog the user has to enter the numbers of right/left channels to consider in the moving average smoothing process. The smoothing starts by clicking on the “**Accept Parameter**” button.

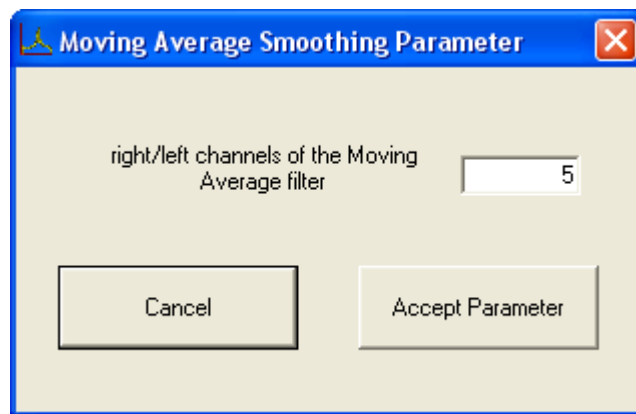


Fig. 1.10. Screenshot of the code UMESTRAT, “**Moving Average Smoothing Parameter**” dialog.

- If the user has selected the “**Savitzky-Golay**” radio button in the “**Smoothing technique**” section, the dialog “**Savitzky-Golay Smoothing Parameters**” will open. The user has to enter the order of the smoothing polynomial and the numbers of right/left channels to consider in the Savitzky-Golay smoothing process. The smoothing starts by clicking on the “**Accept Parameters**” button. A screenshot of this dialog is shown in Fig 1.11.

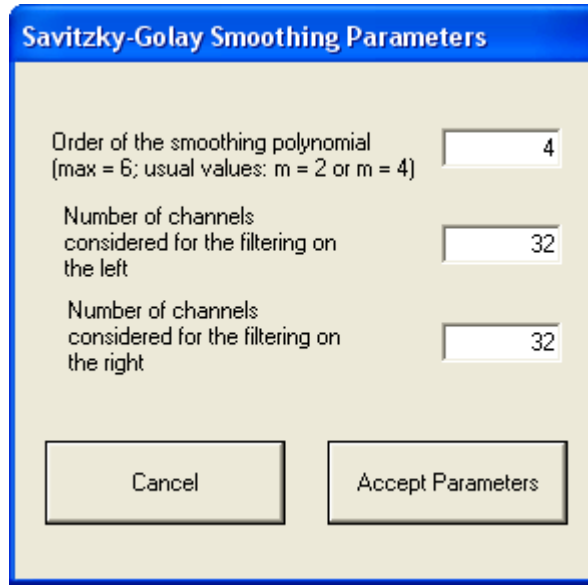


Fig. 1.11. Screenshot of the code UMESTRAT, “**Savitzky-Golay Smoothing Parameters**” dialog.

After clicking on the “**Accept Parameter**” button in the smoothing dialogs, the plot in the “**Default Spectrum Smoothing**” window is updated with the smoothed spectrum. To accept the obtained distribution the user must click on the “**Accept Smoothing**” button. The “**Undo Smoothing**” button allows to steps back to the smoothing technique selection. The “**Return to UMESTRAT**” button allows to steps back to the “**Default Spectrum**” tab.

### 1.4.6 Unfolding MAXED tab

The tab “**Unfolding MAXED**” is the last tab of the UMESTRAT interface. In this tab the user can compute the final distribution of the considered unfolding problem. The code MAXED is used for this purpose. The unfolding procedure is solved using the distribution obtained in the tab “**Default Spectrum**” as default spectrum and the chi-square obtained in the “**Chi-square**” tab as built in stop condition. In this tab it is also possible to save the current computation in a specific input file. A screenshot of this tab is shown in Fig 1.12.

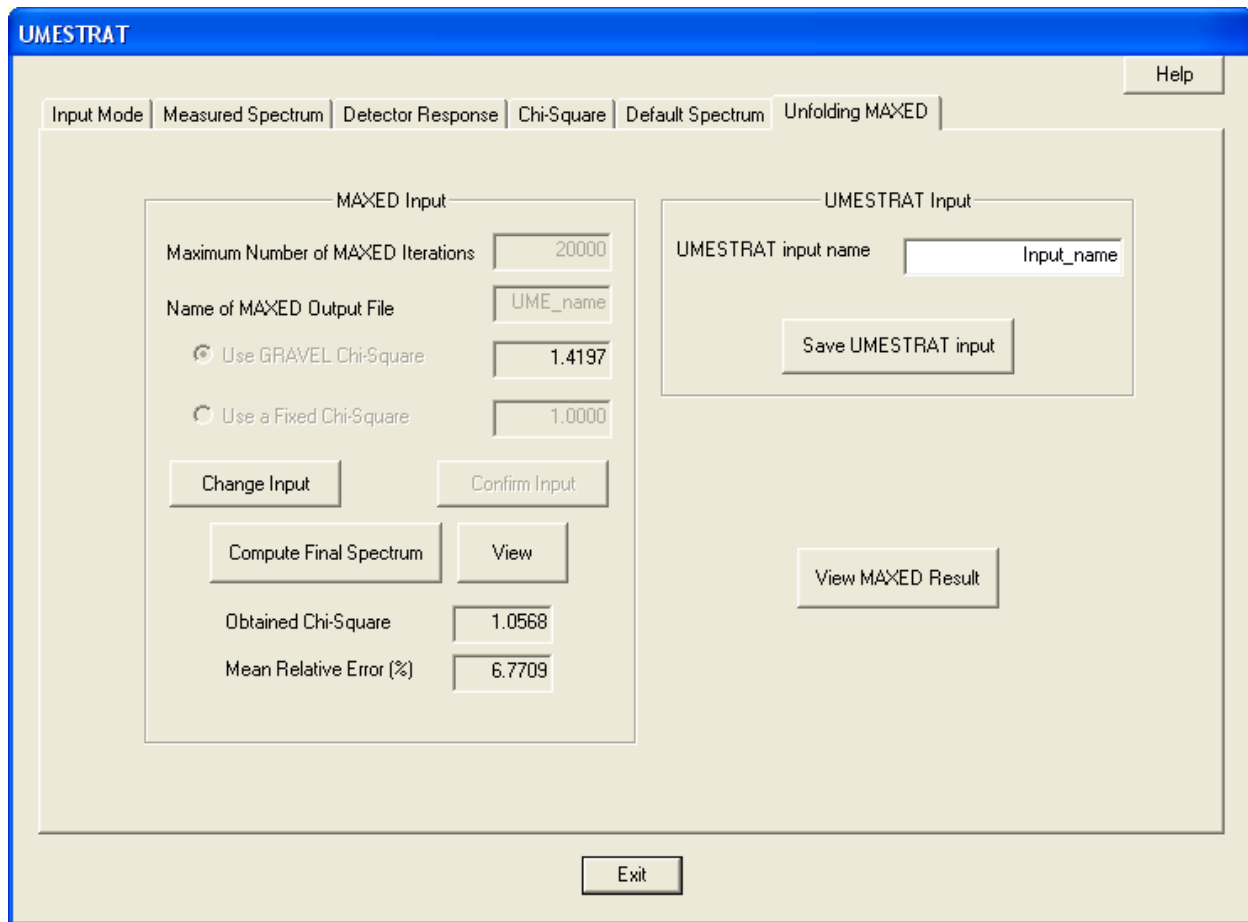


Fig 1.12 Screenshot of the code UMESTRAT, “**Unfolding MAXED**” tab.

To compute the unfolding solution, the user has to:

1. Insert the data input for the MAXED computation in the “**MAXED input**” section which comprise: the “**Maximum Number of MAXED Iterations**”, the “**Name of the MAXED Output File**” and the chi-square per degree of freedom to use as built-in stop condition by choose if to use the chi-square per degree of freedom computed in the tab “**Chi-Square**” by check the “**Use GRAVEL Chi-Square**” radio button or use a freely chosen chi-square per degree of freedom by check the “**Use a Fixed Chi-Square**” radio button.
2. Click on the “**Confirm Input**” button to confirm the entered values of the MAXED input.
3. Click on the “**Compute Final Spectrum**” button to start the MAXED computation and wait until the calculation is over.



The “**View**” button opens the report file of the MAXED computation. The “**View MAXED Result**” button allows to views a graphical representation of the obtained final unfolded distribution.

To save an input file of the current computation, the user has to:

1. Insert the desired name of the input file in the “**UMESTRAT input name**” string of the “**UMESTRAT Input**” section.
2. Click on the “**Save UMESTRAT Input**” button in the “**UMESTRAT Input**” section.

This procedure produces a specific input file in the “.ume” format, which can be loaded in a subsequent computation.

### 1.4.7 UMESTRAT plot window

At each computational stage the code UMESTRAT produces a graphical representation of the intermediate spectrum. A screenshot of the UMESTRAT plot window is show in Fig 1.13.

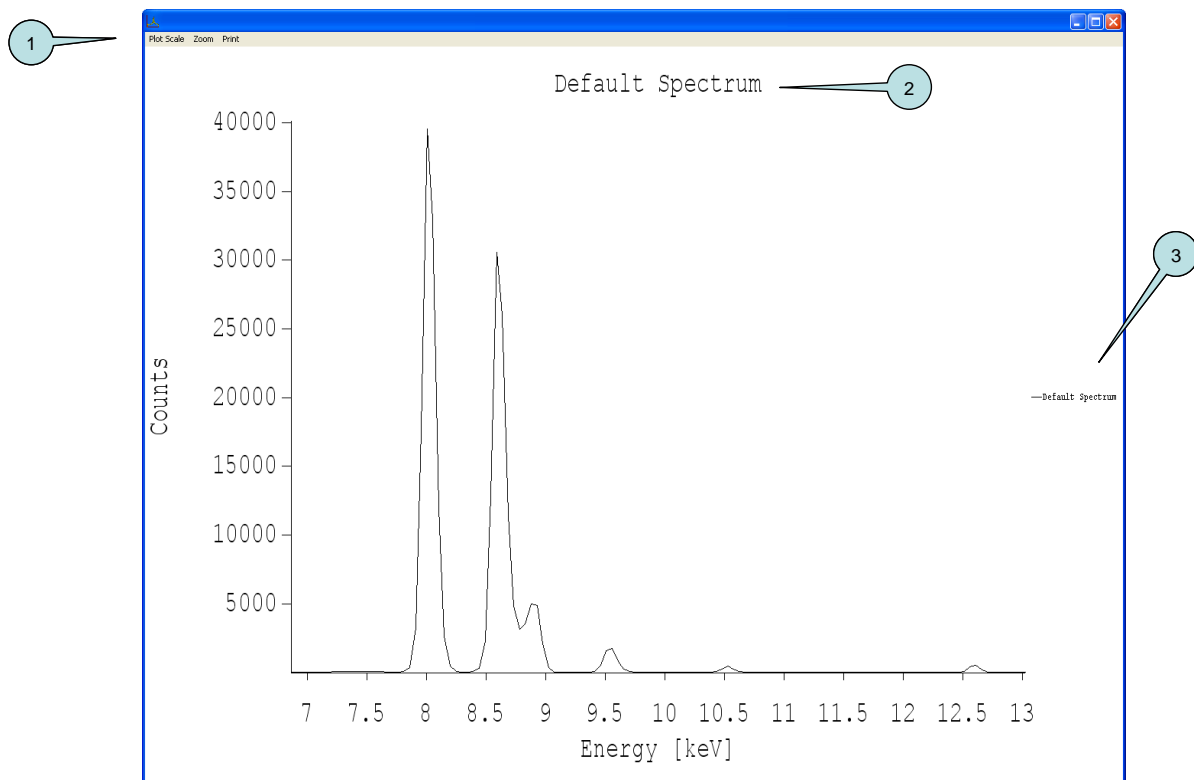


Fig 1.13. Screenshot of the code UMESTRAT, Plot window. In the figure, (1) is window menu, (2) is the plot name and (3) is the legend of the plotted distributions.

As shown in Fig 1.13 the plot window contains:

1. A menu that allows to:
  - a. Set the plot scale as linear or logarithmic.
  - b. Set a zoom in the plot (this can be done interactively by the user, selecting with the mouse the area to zoom).
  - c. Save the current plot as “.eps” file
2. The title of the graphical representation.
3. A legend with the distributions currently plotted.

## 1.5 UMESTRAT unfolding result

In what follows an application of the code UMESTRAT is presented. The X-ray measurement was obtained by irradiating a brass target with a Hamamatsu X-ray tube for a time of 3000 s with 50 keV and 0.95 mA. The measurement system consists of an AMPTEK XR-100CR Si-PIN detector with a lead collimator with a 0.5 mm window, used together with and an AMPTEK MCA8000A multichannel analyzer. The experimental set-up is shown in Fig. 1.14.

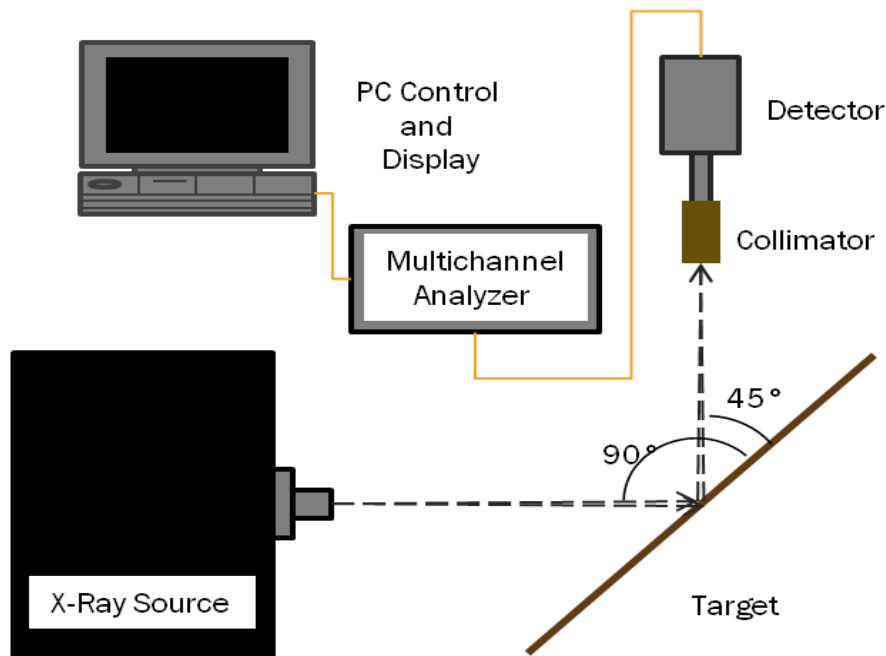


Fig 1.14. Experimental setup used for the XRF brass measurement.

The DRF matrix is estimated using the Monte Carlo code MCSHAPE and the code RESOLUTION [Fernandez, 2009]. MCSHAPE simulates the energy deposition spectrum inside the Si-PIN detector using  $10^6$  photon histories for each of the 1024 energy channel (from 0 keV to 50 keV) used to discretize the DRF (the used DRF discretization is the same used for the measurement). RESOLUTION adds the detector resolution to the MCSHAPE results. Fig. 1.1 shows an example for one DRF column. The measured spectrum distribution is shown in Fig 1.15.

From Fig. 1.15 it can be seen how the detection system cause the overlapping of the  $K\alpha$  peak of zinc and the  $K\beta$  peak of copper. The presence of the L peaks of lead is due to the collimator used during the measurement process.

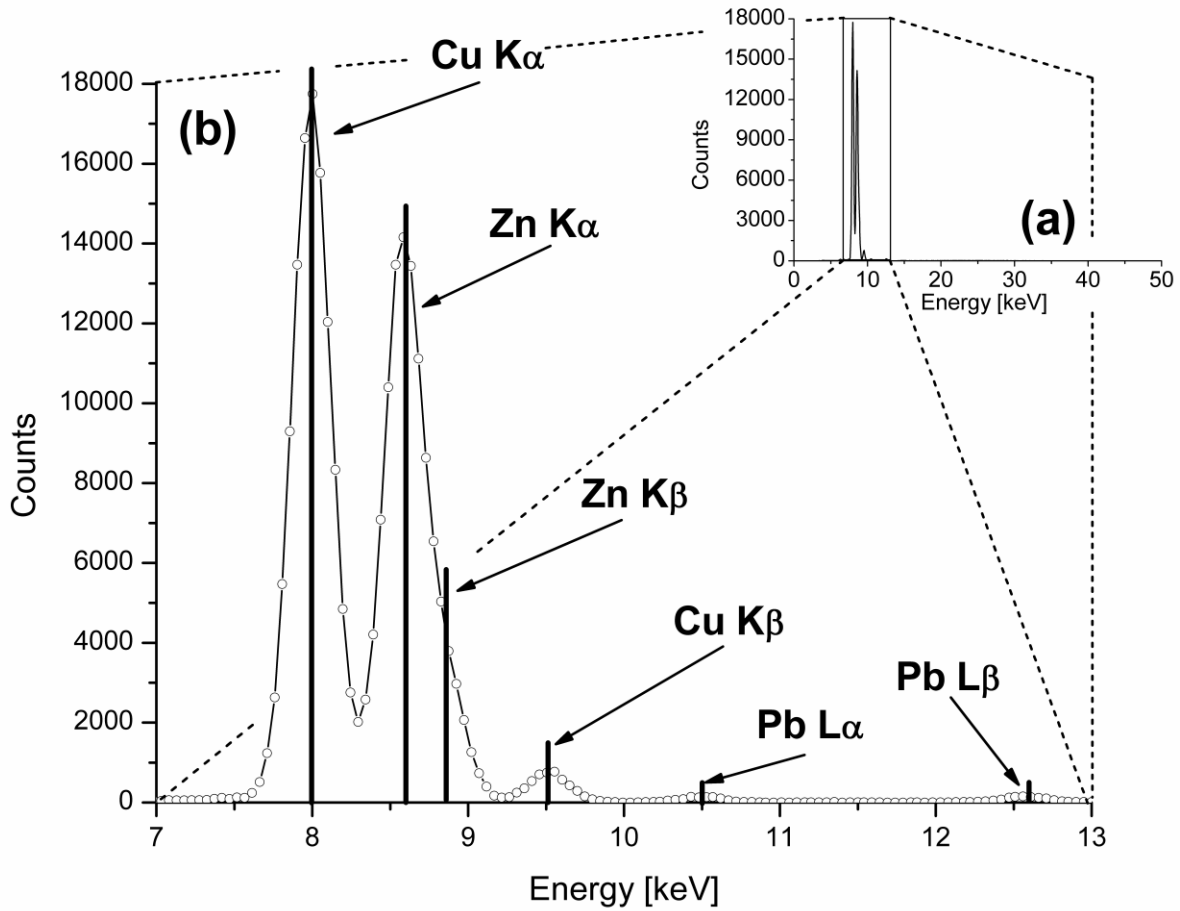


Fig. 1.15. Spectrum of a brass target. (a) Full energy range spectrum (0-50keV); (b) Zoom in the energy range where the characteristic peaks are located. The measured distribution (line plus circle) is presented with the theoretical position of each characteristic line (solid lines).

From the GRAVEL computation in the “**Chi-Square**” tab, using a maximum number of GRAVEL iteration equal to 2000, it is obtained the following results:

Chi-square per degree of freedom	$\chi^2 = 1.4197$
Mean relative error (%)	$\varepsilon_r = 7.8476$

Tab 1.1. Chi square per degree of freedom and main relative error obtained UMESTRAT in the “**Chi-square**” tab, for a brass target.

The optimal default spectrum was computed in the “**Default Spectrum**” tab, by using as building stop conditions the chi-square just found with GRAVEL (Tab 1.1) and 2000 maximum number of iterative steps. The MAXED result is then processed in the “**Default Spectrum**” window. Three ROIs are selected (Fig. 1.16): the first one containing the  $K\alpha$  and  $K\beta$  of zinc and copper, the second one containing the  $L\alpha$  lead peak, and the third one containing the  $L\beta$  lead peak. A moving average filter with 5 points is used to smooth the default spectrum. The obtained default spectrum is shown in Fig 1.17.

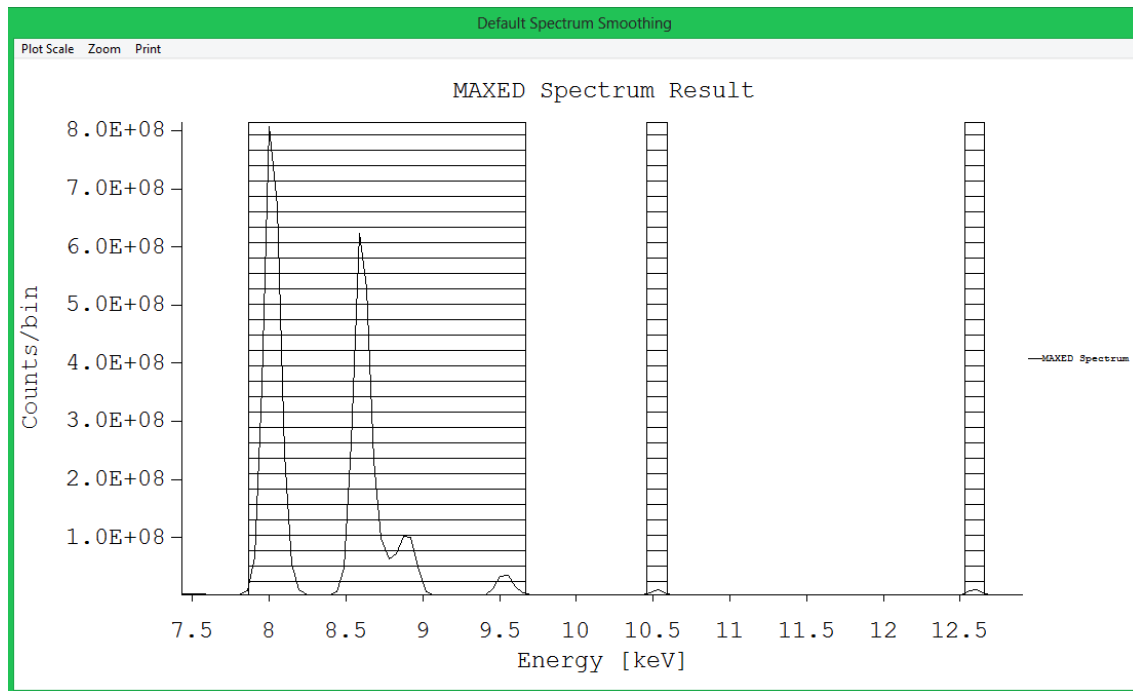


Fig 1.16. Screenshot from the code UESTRAT, ROI selection from the “**Default Spectrum**” window. The graph shows the distribution obtained with MAXED in the “**Default Spectrum**” tab for the considered brass example. Three ROI are selected.

From Fig 1.17 (a) it can be seen that in the default spectrum build with UESTRAT the peaks overlapping is well resolved. In Fig. 1.17 (b) it can be seen how the UESTRAT smoothing process cleans the noise in the distribution, leaving unchanged the ROI of the spectrum.

The final unfolded spectrum is computed in the “**Unfolding MAXED**” tab by using the chi-square per degree of freedom computed in the “**Chi-square**” tab, the default spectrum build in the “**Default Spectrum**” tab and by set the maximum number of MAXED iterations to 20000. The obtained result is shown in Fig 1.18.

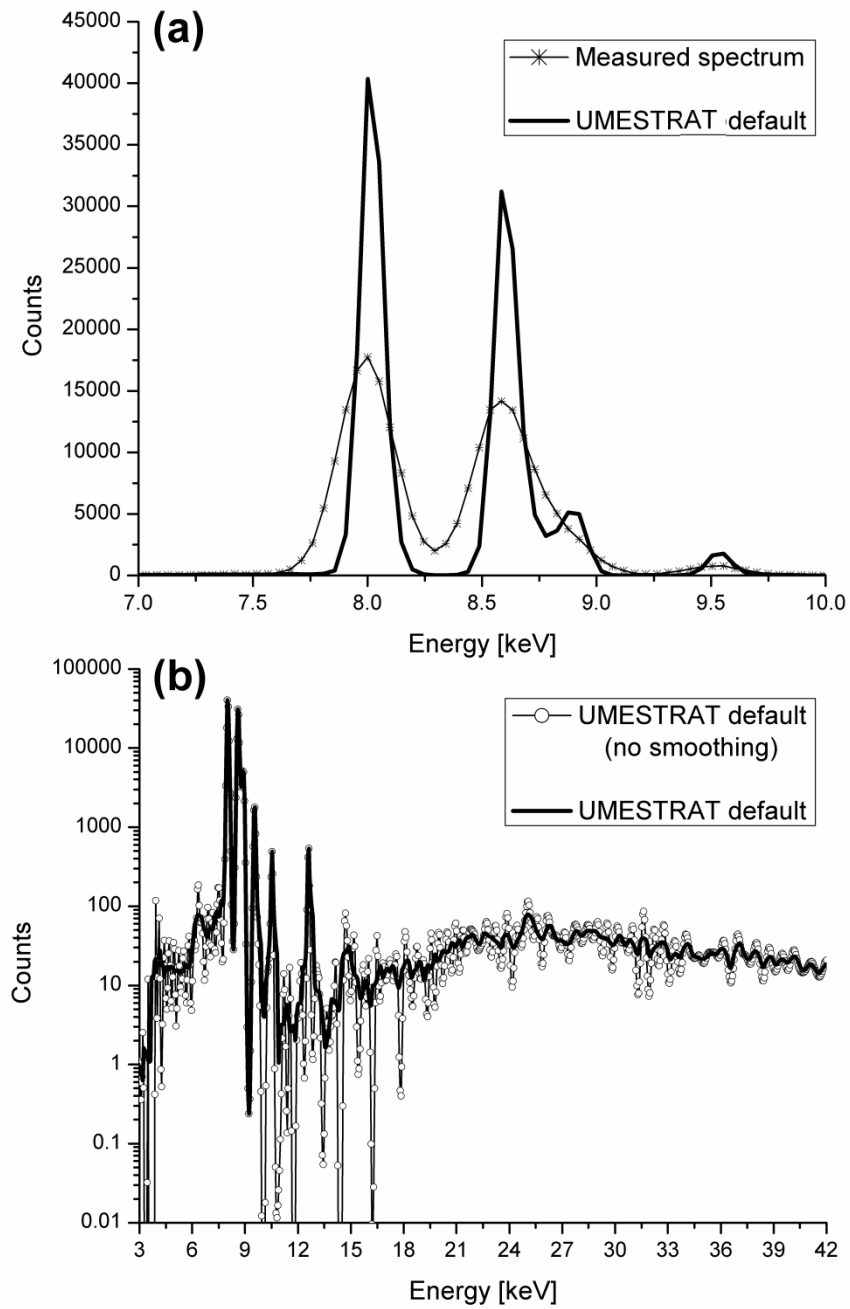


Fig 1.17. UMESTRAT default spectrum. The figures show: (a) the comparison between the measured spectrum and the default spectrum build with UMESTRAT; (b) the comparison of the smoothing effect on the default spectrum build with UMESTRAT (Logarithmic scale).

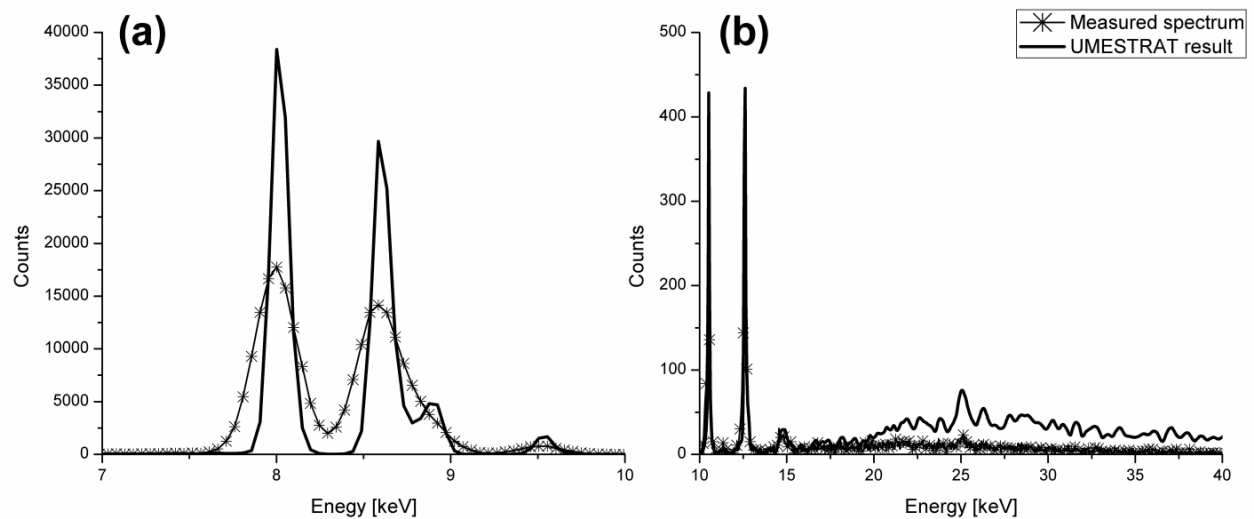


Fig 1.18 UMESTRAT unfolding of a brass spectrum. in the graph it is compared the measurement (line with star) with the unfolding result obtained with UMESTRAT: (a) in the energy range where the zinc and copper peaks in the measurement are overlapped; (b) in the energy range containing the lead peaks and the continuum part.

From Fig. 1.18 (a) it can be seen that the peaks in the solution are resolved. In Fig. 1.18 (b) it is shown how the noise in the continuum is successfully removed. The parameters of the final unfolded solution are:

Chi-square per degree of freedom	$\chi^2 = 1.3840$
Mean relative error (%)	$\varepsilon_r = 7.7483$

Tab 1.2. Chi square per degree of freedom and main relative error obtained UMESTRAT in the “**Unfolding MAXED**” tab, for a brass target.





## Chapter 2

# Kernel refinement in the X-ray Boltzmann transport model

X-rays are electromagnetic radiations which can interact with matter in different ways depending on their energy. There are three main photon interaction processes whose influence prevails in the X-ray regime [1~150 keV]: the coherent (or Rayleigh) scattering, the incoherent (or Compton) scattering, and the photoelectric effect [Evans, 1955], [Agarwal, 1991]. These interactions produce secondary photons that carry out useful information about the atoms comprising the interacting target. The produced secondary radiation can be characterized by using photon transport codes (deterministic or Monte Carlo) based on the Boltzmann transport equation model described by [Fernandez, 1992]. In this model, the flow of X-rays is determined by solving the Boltzmann integro-differential transport equation in the considered physical system. In the Boltzmann model, the behavior of photon interactions in an X-ray transport process is depicted through the use of functions called single interaction kernels. Despite the optimal results given by this model [Fernandez, 2007-1], not all the possible X-ray radiative processes are described by the kernels used in the Boltzmann model. It is well-known in fact that both the photoelectric effect and the Compton scattering are ionization mechanisms of inner shell in atoms causing a XRF emission through an atomic relaxation process. However, in the kernels used by the Boltzmann model the photoelectric effect is considered as the only ionizing interaction, and only atomic relaxation from the photoelectric effect is considered.

The XRF contribution due to Compton inner shell ionization is usually neglected because of the lower size of the Compton cross section compared to the photoelectric one. As shown in Fig. 2.1, in fact, the photoelectric absorption clearly dominates over Compton scattering in the low energy region since the photoelectric cross section goes to its maximum for energy values near the electron binding energy, the Compton cross section vanishes rapidly due to binding effects. The situation is reversed at high photon energies. The crossing point energy, at which the ionization is equally probable either by photoelectric absorption or by Compton scattering, depends on the atomic number and its value increases as the element atomic number increases. In a recent work by Stutz [Stutz, 2014] the XRF contribution due to atomic relaxation from Compton ionization of inner shells was studied in terms of single shell ionization probability for the K shell and the energy values where the Compton interaction becomes the main process of creation of K-shell vacancies are assessed for elements with  $Z$  equal to 6, 13, 29, 47 and 79.

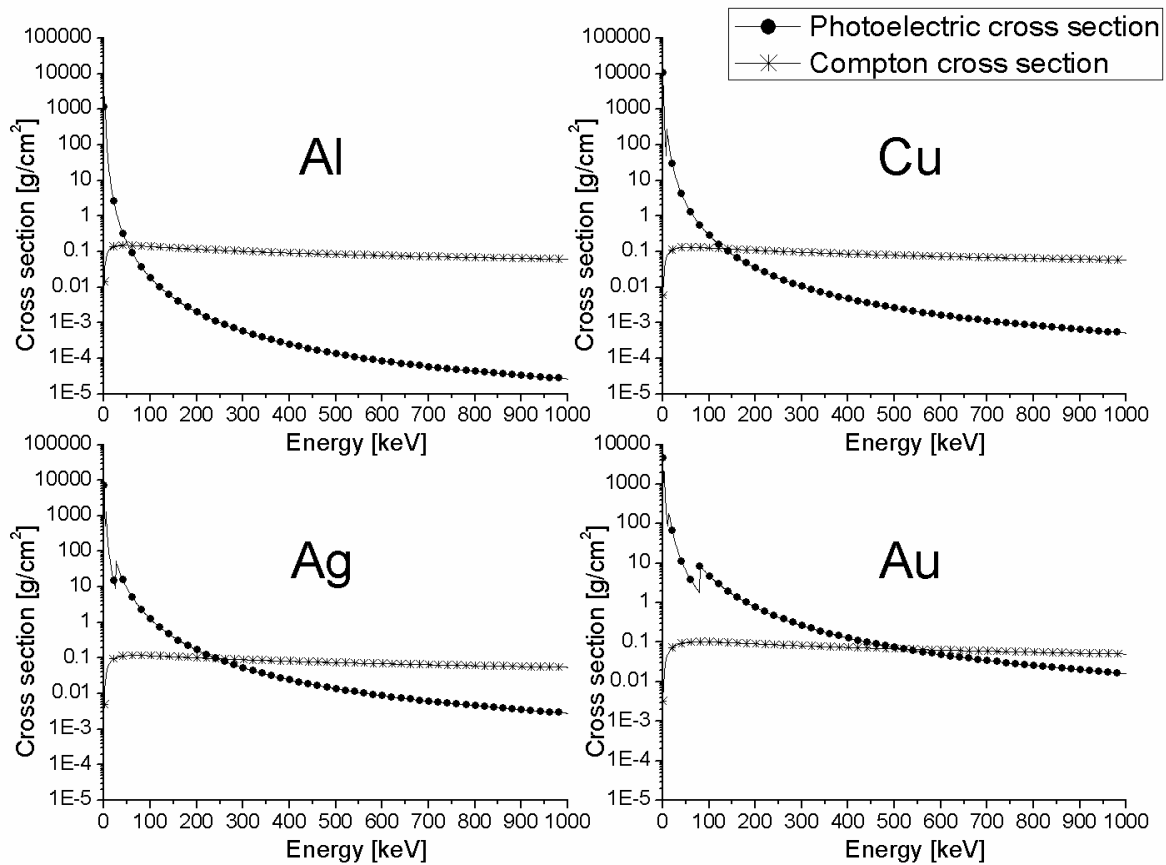


Fig 2.1. Photoelectric mass attenuation and Compton scattering mass attenuation for Al ( $Z=13$ ), Cu ( $Z=29$ ), Ag ( $Z=47$ ), and Au ( $Z=79$ ). Both Compton scattering and photoelectric effect distributions are taken from the EPDL 97 data library [Cullen, 1997]. From the figure it can be seen that Compton scattering becomes more important than photoelectric effect for energy greater than 53 keV for Al, 134 keV for Cu, 244 keV for Ag and 522 keV for Au.

In this thesis it is proposed a more detailed description of the XRF contribution due to Compton single shell ionization in the framework of the impulse approximation (IA). The XRF contribution due to Compton ionization is evaluated for the shells K, L and M for all elements with  $Z$  from 11 to 92 and in the energy range from 1 to 1000 keV by developing a deterministic code. A simple formula which allows the computation of the XRF Compton correction (in percentage of the XRF due to photoelectric) is implemented. The obtained results show that the XRF contributions from Compton single shell ionization may play an important role in the description of the radiation field in X-ray spectrometry for some special cases. Finally a new kernel which introduces the XRF Compton correction in the Boltzmann model, refining the kernel description of X-ray processes, is introduced. The computational strategy used to evaluate XRF correction from Compton single shell ionization is shown together with some examples of the obtained results.

## 2.1 The Boltzmann scalar transport equation

There exist different degrees of approximation to describe the diffusion of photons. The more popular is the scalar Boltzmann model, which considers a photon that does not modify its (average) polarization state. This model describes the balance between the number of photons of given energy and direction entering and leaving the considered volume element. This balance can be formulated for conditions where the X-ray source is constant in time (steady-state problem) and, therefore, also the flux of the photons in the medium.

If we consider a point  $\vec{r}$  and an infinitesimal right cylinder with a base area  $dA$  centered at  $\vec{r}$  and with height  $dl$ , whose lateral surface is parallel to the direction  $\vec{\omega}$ , the flux  $f(z, \vec{\omega}, E)dEd\omega$  is defined as the number of photons with energy between  $E$  and  $E + dE$ , and with direction between  $\vec{\omega}$  and  $\vec{\omega} + d\vec{\omega}$ , which cross a unit area of the base of the infinitesimal cylinder per unit time. The scalar integral-differential Boltzmann transport equation, for a simple model of backscattering from an infinitely thick target, is defined as:

$$\begin{aligned} \eta \frac{\partial}{\partial z} f(z, \vec{\omega}, E) &= -\mu(E)f(z, \vec{\omega}, E) \\ + \sum_i^{\text{all interactions}} \int_0^\infty \left( \int_{4\pi} \cup(z) k_i(\vec{\omega}', E', \vec{\omega}, E) f(z, \vec{\omega}', E') d\omega' \right) dE' & \quad (2.1) \\ &+ S(z, \vec{\omega}, E) \end{aligned}$$

where  $\vec{\omega}'$  and  $\vec{\omega}$  are the unit vectors defining the propagation direction of the photons respectively before and after a generic interaction,  $E'$  and  $E$  are the energy before and after a generic interaction,  $\eta$  denotes the directional cosine  $\omega_z$ ,  $d\omega' = d\eta' d\phi'$  is the differential of the solid angle in the direction of the unitary vector  $\vec{\omega}'$ ,  $\mu(E)$  is the total attenuation coefficient,  $\cup(z)$  the unitary step Heaviside function,  $k(\vec{\omega}', E', \vec{\omega}, E)$  is the single process kernel, and  $S(z, \vec{\omega}, E)$  is a generic source of photons in the considered volume. Although this equation is one-dimensional, it contains the full phase-space information about the incident and take-off directions and energy of the photons.

The influence of X-ray interactions in the transport process is taken into account in Eq. 2.1 through the total attenuation coefficient and the single process kernels. These two magnitudes are directly related with the interaction cross sections  $\sigma_T$ , which is defined, for a generic photon interaction  $T$ , as the probability density function that photons, with direction  $\vec{\omega}'$  and energy  $E'$ , undergo the considered interaction. The total attenuation coefficient  $\mu(E)$  describes the extent of which the intensity of the radiation beam is reduced as the photons passes through a specific material target. This magnitudes is defined as the sum of the cross sections of all the possible interaction that photons with energy  $E$  can involve along their path while crossing the considered medium, and is expressed as

$$\mu(E) = \sigma_R(E) + \sigma_C(E) + \tau(E) \quad (2.2)$$

where  $\sigma_R$  is the Rayleigh cross section,  $\sigma_C$  is the Compton cross section and  $\tau$  is the photoelectric effect cross section. The single process kernel is defined, per unit path through the medium and per unit of solid angle and energy of scattered photons, as the probability density function that photons scatter in  $(\vec{\omega}, E)$  from  $(\vec{\omega}', E')$ . Through its definition, the single process kernel for the generic interaction  $T$  can be expressed as the double differential cross section of the interaction:

$$k_T(\vec{\omega}', E', \vec{\omega}, E) = \frac{d\sigma_T}{d\vec{\omega}dE} \quad (2.3)$$

Then the cross sections for the process  $T$  can be obtained from the relation

$$\sigma_T(\vec{\omega}', E') = \int_0^\infty dE \int_{4\pi} k_T(\vec{\omega}', E', \vec{\omega}, E) d\vec{\omega} \quad (2.4)$$

In what follows the definition of the atomic interaction kernels for the three dominating interactions that participate in X-rays photon transport (Rayleigh scattering, Compton scattering, and photoelectric effect) is discussed. Polarization effect will be not introduced here.

## 2.2 Rayleigh single process kernel

Rayleigh (or coherent) scattering is a process where photons change direction (momentum transfer) but not energy. This scattering takes place with the most tightly bound electrons of the atom which behave rigidly during the interaction. In this interaction the atom is neither ionized nor excited. Rayleigh scattering occurs mostly at the low energies and for high-Z materials.

A first description of the coherent scattering was made by J. J. Thomson [Thomson, 1903], [Agarwal, 1991]. In this approximation the Rayleigh scattering is idealized as an interaction occurring between a photon and a free single electron. By this assumption, the double-differential cross section can be expressed through the relation:

$$\left(\frac{d^2\sigma_R}{d\vec{\omega}dE}\right)_{Thomson} = \frac{r_e^2}{2} [1 + (\vec{\omega} \cdot \vec{\omega}')^2] \delta(E - E') \quad (2.5)$$

where  $r_e^2$  is the classical radius of electron ( $2.81 \cdot 10^{-13}$  [cm]). The delta function in the relation stressed the monochromaticity of the scattering.

When we consider the scattering interaction with an atom, a cooperative effect from the whole electron's cloud is verified. The effects due to this constructive interference from the global atomic charge distribution are comprised in the kernel expression by using the square form factor  $F^2(E', \vec{\omega}, \vec{\omega}', Z)$ . By this approximation the atomic differential cross section can be expressed as

$$\begin{aligned} \left(\frac{d^2\sigma_R}{d\vec{\omega}dE}\right)_{at} &= F^2(E', \vec{\omega}, \vec{\omega}', Z) \left(\frac{d^2\sigma_R}{d\vec{\omega}dE}\right)_{Thomson} \\ &= \frac{r_e^2}{2} [1 + (\vec{\omega} \cdot \vec{\omega}')^2] F^2(E', \vec{\omega}, \vec{\omega}', Z) \delta(E - E') \end{aligned} \quad (2.6)$$

Hubbell et al. [Hubbell, 1975] reviewed exhaustively the computation of the form factor. By defining the transferred momentum as

$$x = \frac{hc}{E'} \sin\left(\frac{\theta}{2}\right) \quad (2.7)$$

for given energy  $E'$  and scattering angle  $\theta$  they computed tables of  $F^2(x, Z)$  for all the elements in the periodic table. In Eq. 2.7,  $h$  is the Plank constant ( $4.136 \cdot 10^{-15}$  [eV·s]), and  $c$  is the speed of light in vacuum ( $29.979 \cdot 10^9$  [cm·s<sup>-1</sup>]). Some special limits of the form factor are  $F(0, Z) = Z$ , and  $F(\infty, Z) = 0$ . Cullen et al. [Cullen, 1997] includes detailed photon interaction data from the Hubbell data base for all elements with atomic number  $Z$  from 1 to 100 over the energy range from 1 eV to 100 GeV. From this library, the Hubbell's non-relativistic values of  $F^2(x, Z)$  can be computed by means of logarithmic interpolation.

From Eq. 2.6 it is evident that the Rayleigh atomic kernel for unpolarized photons, with phase-space coordinates  $(\vec{\omega}', E')$ , scattered by a pure element target of atomic number  $Z$  into the coordinates  $(\omega, E)$ , can be expressed as

$$k_R(\vec{\omega}', E', \vec{\omega}, E) = \frac{\rho N}{A} \left( \frac{d^2\sigma}{d\omega dE} \right)_{at} = \sigma \delta(E - E') [1 + (\vec{\omega} \cdot \vec{\omega}')^2] F^2(E', \vec{\omega}, \vec{\omega}', Z) \quad (2.8)$$

where  $\sigma$  is the macroscopic attenuation coefficient [cm<sup>-1</sup>] defined as

$$\sigma = \rho N_A r_e^2 / (2A) \quad (2.9)$$

where  $N_A$  is the Avogadro number ( $6.022 \cdot 10^{23}$  [mol<sup>-1</sup>]), and  $A$  and  $\rho$  are respectively the atomic weight and the density of the considered element  $Z$ .

The kernel angular dependence in Eq. 2.8 is due to the last two factors: the Thomson angular factor, and the square of the atomic form factor comprising the constructive interferences from the whole atomic charge distribution.

## 2.3 Compton single process kernel

Compton (or incoherent) scattering is a photon interaction where the energy as well as the direction of the incident photon is changed. In this process the atom is ionized and the ejected electron (Compton electron) have energy  $E_{e_i}$  equal to the difference between the incoming photon energy  $E'$  and the outgoing photon energy  $E$  plus the binding energy of the shell  $i$  involved in the interaction  $U_i$ ; ( $E_{e_i} = E' - E - U_i$ ). As the Compton event occurs preferentially with the outer electrons of the atom (with electron's binding energy  $U_i$  small compared with the incoming photon energy  $E'$ ) the stuck electron can be considered, in first approximation, as a free electron at rest (mass rest energy  $m_e c^2$ , null momentum). By this assumption, a first study on the Compton scattering was made by Compton [Compton, 1923], [Evans, 1958]. In this approach, the conservation of energy and momentum during the hit establishes that, if the photon scatters with a scattering angle  $\theta$ , it carries an energy  $E'$  equal to

$$E' = E_p = \frac{E'}{1 + \frac{E'}{m_e c} (1 - \cos\theta)} \quad (2.10)$$

where  $\cos\theta = \vec{\omega} \cdot \vec{\omega}'$ ,  $\vec{\omega}'$  and  $\vec{\omega}$  are respectively the direction of the incoming and the outgoing photon, and  $E_p$  is called the Compton peak energy.

In this approximation, the differential electronic cross section for the described collision (average polarization) has been computed by Klein and Nishina [Klein, 1929], [Heitler, 1935] as

$$\left(\frac{d^2\sigma}{d\omega d\lambda}\right)_e = \frac{r_e^2}{2} k_{KN}(E, E', \theta) \delta(E - E_p) \quad (2.11)$$

where the angular dependence of the scattering is considered in the Klein-Nishina (KN) function  $k_{KN}(E, E', \theta)$  defined as

$$k_{KN}(E, E', \theta) = \left(\frac{E}{E'}\right)^2 \left\{ \frac{E'}{E} + \frac{E}{E'} + \sin^2\theta \right\} \quad (2.12)$$

It is apparent that for  $E' \approx E$ , Eq. 2.11 reduces to the classical Thomson expression for the elastic scattering of photons with free electrons expressed in Eq. 2.5. The Eq. 2.11 represents only a rough approximation for the Compton interaction of photons with atoms. The delta function in Eq. 2.11 fixes the integration path in the phase-space along the line  $E - E_p$ , and this condition does not account for the shift for bound electrons [Evans, 1958]. In fact in reality atomic electrons are not at rest but move with a certain momentum distribution which gives rise to the so called Doppler broadening of the Compton line. Moreover, ionization of bound electrons is allowed only if the energy transfer ( $E' - E$ ) is larger than the electron ionization energy  $U_i$  of the active shell (binding effect).

The KN cross section fails to describe the Compton interaction when the energy of the incoming photon becomes comparable with the electron binding energy and a departure from this approximation is verified. Atomic electrons binding effect and pre-collision motion of the electrons can be taken into account in the Compton single process kernel expression by introducing in Eq. 2.11 the so-called incoherent scattering function  $S(x, Z)$ , obtaining the equation

$$\left(\frac{d^2\sigma}{d\omega d\lambda}\right)_{at} = \frac{r_e^2}{2} k_{KN}(E, E', \theta) S(x, Z) \delta(E - E_p) \quad (2.13)$$

where  $Z$  is the element atomic number and  $x$  is the transferred momentum defined in Eq. 2.7.



The incoherent scattering function here introduced can be expressed through different approximations. In what follows the two main approximations used in the Boltzmann standard model are depicted.

### 2.3.1 Compton scattering function in the Waller-Hartree approximation

An evaluation of the incoherent scattering function was made by Waller and Hartree through the introduction of the Waller-Hartree (WH) scattering function  $S^{WH}(x, Z)$  [Waller, 1929]. By this approximation it is possible to take into account that the electron is not free but is part of the atom and to include in the Compton kernel the description of the effect due to the binding energies of whole electrons in the atom. The double-differential atomic cross-section in the WH approximation, for incident photons with phase-space coordinates  $(\vec{\omega}', E')$  scattered by a pure element target of atomic number  $Z$  into the coordinates  $(\vec{\omega}, E)$ , is expressed as

$$\left( \frac{d^2\sigma}{d\vec{\omega}dE} \right)_{at}^{WH} = \frac{r_e^2}{2} k_{KN}(E', E, \theta) S^{WH}(x, Z) \delta(E - E_p) \quad (2.14)$$

Therefore the Compton kernel in the WH approximation is defined as

$$k_C^{WH}(\vec{\omega}', E', \vec{\omega}, E) = \frac{\rho N}{A} \left( \frac{d^2\sigma}{d\vec{\omega}dE} \right)_{at}^{WH} = \sigma k_{KN}(E', E, \theta) S^{WH}(x, Z) \delta(E - E_p) \quad (2.15)$$

Hubbell et al. [Hubbell, 1975] reviewed exhaustively the computational technique for obtaining the scattering function, producing tables of  $S^{WH}(x, Z)$  for all the elements in the periodic table. Special limits of the scattering function are  $S^{WH}(0, Z) = 0$ , and  $S^{WH}(\infty, Z) = Z$ . The WH scattering function then can be interpolated from the tables in literature [Cullen, 1989] or computed by means of semi-empirical formulas provided by several authors [Veigele, 1966], [Smith 1975].

### 2.3.2 Compton scattering function in the impulse approximation

The WH approximation shown in Eq. 2.15 introduces in the Compton kernel description the binding effect of the atom but does not consider the pre-collision motion of the electron, limiting the Compton peak to a monochromatic line. DuMond [DuMond, 1929], [DuMond, 1930], [DuMond, 1930] shows that electrons momenta distribution during the Compton interaction are responsible of the so-called Doppler broadening of the Compton line. The description of a model able to outline this effect in the Compton single process kernel was illustrated by Ribberfors [Ribberfors, 1975]. In particular he derived, in a relativistic treatment within the limits of the impulse approximation (IA) for photon–electron interactions, an expression for the doubly differential cross section for Compton scattering, factorizing it into a kinematical factor and a scattering system-dependent function called the Compton profile. In the impulse approximation two assumptions was made on the Compton interaction:

- all electrons of the atom target are treated as free electrons with the same momentum distribution of bounds electrons;
- the Compton scattering interaction is considered as an impulsive interaction, i. e. the potential field generated by electrons not involved in the scattering process does not change immediately after and before the interaction (these electrons do not participate to the collision process and cannot occupy the produced vacancy until the Compton electron has left the system).

These assumptions are valid when the energy transfer is so large that binding effects for the electrons may be neglected. By these approximations the energy of the outgoing photon  $E$  is linked to the momentum of the interacting electron  $\vec{p}$  through the relativistic expression:

$$E = E' - \frac{EE'}{m_e c^2} (1 - \cos \theta) + \frac{p_z}{m_e c} (E^2 + E'^2 - EE' \cos \theta)^{1/2} \quad (2.16)$$

where  $p_z$  is the projection of the momentum  $\vec{p}$  of the interacting electron along the scattering vector  $\vec{q}$  defined as

$$\vec{q} = \frac{\vec{\omega}}{|\vec{\omega}|} - \frac{\vec{\omega}'}{|\vec{\omega}'|} \quad (2.17)$$

Electrons in the atom however do not hold a defined state of momentum as depicted in Eq. 2.16, but has a momentum distribution  $\rho_i(p)$  that depends on the atomic shell  $i$  occupied by the electron. If the target consists in electrons from the shell  $i$  with momenta distribution  $\rho_i(p)$ , the Compton double differential cross section for the considered shell will be proportional to the magnitude

$$J_i(p_z) = \int \int \rho_i(\vec{p}) dp_x dp_y \quad (2.18)$$

where  $J_i(p_z)$  is the so-called Compton profile of the considered atom's shell  $i$ . The constant of proportionality in the Compton double differential cross section expression is the KN cross section illustrated in Eq. 2.12. It is customary to use instead of  $p_z$  the dimensionless variable  $Q$  defined as [Biggs, 1975]

$$Q = \frac{4\pi\epsilon_0\hbar c}{m_e c e^2} p_z \rightarrow \frac{p_z}{m_e c} \cong \frac{Q}{137} \quad (2.19)$$

where  $e$  is the electron charge ( $1.602 \cdot 10^{-19}$  [C]),  $\epsilon_0$  is the vacuum permittivity ( $8.854 \cdot 10^{-12}$  [ $\text{F} \cdot \text{m}^{-1}$ ]), and  $\hbar$  is the reduced Plank constant ( $6.582 \cdot 10^{-16}$  [ $\text{eV} \cdot \text{s}$ ]).

It easy to see that from Eq. 2.16 and Eq. 2.18 the  $Q$  values can be expressed in terms of the scattering energies  $E$  and  $E'$  and the scattering angle  $\theta$  through the relation

$$Q = 137 \frac{E - E' + \frac{EE'}{mc^2} (1 - \cos \theta)}{(E^2 + E'^2 - EE' \cos \theta)^{1/2}} \quad (2.20)$$

by these assumptions the Compton profile for the shell  $i$  can be then expressed in function of  $Q$  through the relation

$$J_i(Q) = \frac{1}{2} \int_Q^\infty \frac{\rho_i(\vec{p}) dp}{p} \quad (2.21)$$

For each shell, it is also possible to add the binding effect in the profile description by express the maximum value of  $Q$  as a function of the incoming energy  $E'$  and the scattering angle  $\theta$  by setting  $E = E' - U_i$  in Eq. 2.20 obtaining:

$$Q_{i,MAX} = 137 \frac{\frac{E'(E' - U_i)}{mc^2} (1 - \cos \theta) - U_i}{[(E' - U_i)^2 + E'^2 - 2(E' - U_i)E' \cos \theta]^{1/2}} \quad (2.22)$$

This quantity allows to obtain the scattering function for the single shell  $i$  of the atom in the IA approximation as

$$S_i^{IA}(E', \theta, Z) = n_{e,i} \int_{-\infty}^{Q_{i,max}} J_i(Q) dQ \quad (2.23)$$

where  $n_{e,i}$  represents the number of electrons in the shell  $i$ . This theoretical approach allows both electron binding effects and Doppler broadening of the Compton line (through the Compton profile) to be taken into account.

Through Eq. 2.23 is the possible to express the Compton scattering function in the IA approximation as the sum of the contribution from all the shells of the atom

$$S^{IA}(E', \theta, Z) = \sum_{i=1}^{n_{shell}} n_{e,i} \int_{-\infty}^{Q_{i,max}} J_i(Q) dQ \quad (2.24)$$

where  $n_{shell}$  is the number of shell of the considered atom.

Tables of the orbital and total-atom Compton profiles (respectively  $J_i(Q)$  and  $J(Q)$ ) are tabulated for fixed values of the dimensionless variable  $Q$  in the range  $[-100,100]$  for all the elements for atomic numbers  $1 < Z < 102$  in Biggs et al. [Biggs, 1975].

The double-differential atomic cross-section in the IA approximation, for incident photons with phase-space coordinates  $(\vec{\omega}', E')$  scattered by a pure element target of atomic number  $Z$  into the coordinates  $(\vec{\omega}, E)$ , is expressed as

$$\left( \frac{d^2\sigma}{d\vec{\omega}dE} \right)_{at}^{IA} = \frac{r_e^2}{2} k_{KN}(E', E, \theta) S^{IA}(E', \theta, Z) \delta(E - E_P) \quad (2.25)$$

and therefore the Compton kernel in the IA approximation is defined as

$$k_C^{IA}(\vec{\omega}', E', \vec{\omega}, E) = \frac{\rho N}{A} \left( \frac{d^2\sigma}{d\vec{\omega}dE} \right)_{at}^{IA} = \sigma k_{KN}(E', E, \theta) S^{IA}(E', \theta, Z) \delta(E - E_P) \quad (2.26)$$

## 2.4 Photoelectric single process kernel

The third and last interaction considered in the Boltzmann transport model is the photoelectric effect. In this interaction a photon is absorbed by the interacting atom, ionizing it and releasing an electron with energy  $E_{e_i}$  equal to the difference between the energy of the absorbed photon  $E'$  and the binding energy of the ionized shell of the interacting atom  $U_i$ , ( $E_{e_i} = E' - U_i$ ). The vacancy left by this interaction will be spontaneously filled by an atomic relaxation process from electron transition from a higher energy level. The de-excitation energy is carried off with the emission of a characteristic photon or Auger electrons. Statistically, the two combined process (absorption-ejection) may be considered as a single interaction.

The single interaction kernel for the production of a characteristic line of energy  $E_i$  from a pure element target due to the photoelectric absorption of photons with wavelength  $E'$  is given by [Fernandez, 1989]

$$k_{P_{E_i}}(\vec{\omega}', E', \vec{\omega}, E) = \frac{1}{4\pi} Q_{E_i}(E') \delta(E - E_i) [1 - \cup(E_{e_i} - E')] \quad (2.27)$$

The kernel independence on  $\vec{\omega}'$  and the  $(4\pi)^{-1}$  normalization factor reflects the isotropy of the emitted X-rays. The Heaviside function allows the photoelectric interaction only for energy values of the primary photon greater than the threshold of the absorption edge energy  $E_{e_i}$  for the considered line  $i$ . The emitted line is assumed to be monochromatic with energy value  $E_i$  and monochromaticity of the emitted photon is described in Eq. 2.27 by the delta function. The  $Q_{E_i}(E')$  is the X-ray fluorescence (XRF) emission probability density for a line  $E_i$  which belongs to a series, and it is given by the relation

$$Q_{E_i}(E') = \tau_i(E') g_{e_i} \Gamma_{E_i} \quad (2.28)$$

where  $\tau_i(E')$  represents the photoelectric attenuation coefficient (in  $cm^{-1}$ ) of the emitter element  $Z$  for the corresponding line  $i$ ,  $\Gamma_{E_i}$  is the emission probability of the line  $E_i$  into its own spectral series and  $g_{e_i}$  denotes the radiative fraction for the given series.

The complete photoelectric single kernel interaction of an element Z is obtained by adding all the single lines photoelectric kernel expressed in Eq. 1.27 over the number of line  $n\_lines$  of the element

$$k_p(\vec{\omega}', E', \vec{\omega}, E) = \frac{1}{4\pi} \sum_{i=1}^{n\_lines} Q_{E_i}(E') \delta(E - E_i) [1 - U(E_{e_i} - E')] \quad (2.29)$$

Photoelectric total atomic cross section and partial cross sections for photoionization of K, L, M and N shells, for all elements with Z from 1 to 99, in the energy range from 50eV to 1TeV are reported in Cullen et al. [Cullen, 1997]. Theoretical values of the photoelectric cross sections were computed by Scofield [Scofield, 1973].

## 2.5 Atomic relaxation process

The atomic relaxation is a process that occurs after an ionizing interaction. In this process an excited ion with a vacancy in an inner shell relaxes to its ground state through a sequence of radiative and non-radiative transitions. Radiative transitions lead to a characteristic photon emission. Radiationless transitions can be of two types: Auger and Coster-Kronig. The Auger effect is produced when the X-ray photon originated in the transition is absorbed by an outer electron in the atom, which is subsequently ejected. Therefore, the Auger electron ejection produces a doubly ionized atom without photon emission. Coster-Kronig is a special Auger effect where the transitions occur within subshells of the same shell. If we represent the atom by adopting an independent-electron model, such as the Dirac-Hartree-Fock-Slater self-consistent model [Pratt, 1973] in which each electron occupies a single-particle orbital, with well-defined ionization energy  $U_i$ , the set of orbitals with the same principal and total angular momentum quantum numbers and the same parity constitute a shell  $i$  which can accommodate a finite number of electrons, with characteristic ionization energy  $U_i$ . To ionize a considered shell  $i$  the energy of the ionizing particle must be greater than the characteristic ionization energy  $U_i$ . Figure 2.2 shows the various notations used to designate the innermost atomic electron shells as well as their ordering in energy and their allowed occupancies and transitions.

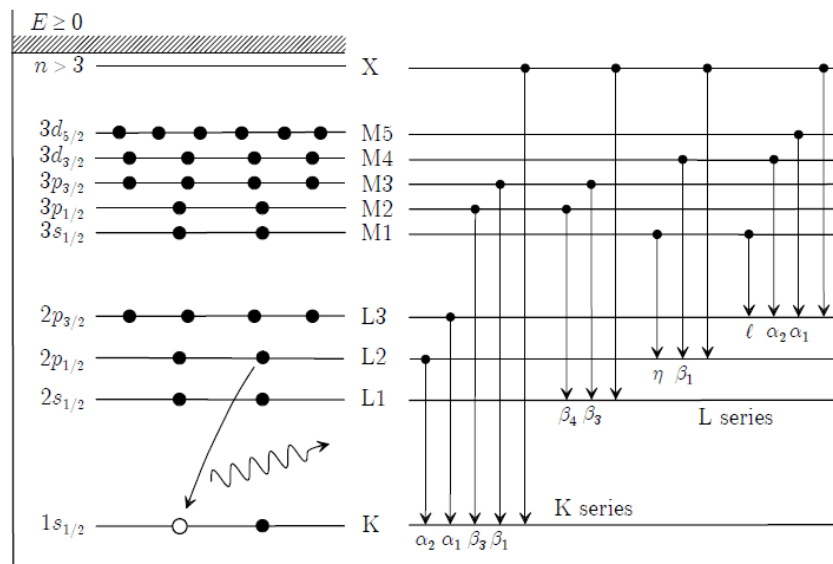


Fig. 2.2. The figure shows, for the atomic shells from K to M5, the electronic configuration (left), the energy level (mid) and the allowed transitions (right). Characteristic line emission can be described by using two different notations: the Siegbahn notation where the transition is expressed through the energy level of the ionized shell followed by the characteristic label of the transition (es.  $K\alpha_1$ ); the IUPAC notation where the transition is expressed by using the two labels of the interested shells (es. K-L3).



## 2.6 XRF contribution from Compton ionization

As shown in the previous sections, all atomic relaxation processes subsequent to a Compton scattering are not considered by the kernels involved in the Boltzmann model in which the characteristic photons production is related only to photoelectric effect events. Because of this simplification an error on the evaluation of the characteristic line intensity is introduced by all transport codes based on the Boltzmann model. The entity of this error may be not negligible in some special cases which need to be examined.

In a recent work by Pavlinsky and Portnoy [Pavlinsky, 2014] the contribution of Compton scattering in the formation of XRF from K-line for elements with low atomic numbers was studied. By expressing the single shell Compton ionization probability of the  $K$ -th shell for an element  $Z$  through the relation:

$$\sigma_{C_K} = \frac{n_K}{Z} \sigma_C \quad (2.30)$$

(where  $n_K$  is the number of electron of the  $K$ -shell), it was demonstrated that, for elements with  $Z$  from 5 to 9, the photo-absorption of primary X-rays from the  $K$ -shell becomes less significant than ionization due to Compton scattering interactions at energies above 60 keV. The crude approximation expressed by Eq. 2.30 can be assumed valid only for low- $Z$  elements where bound electrons of the  $K$ -shell can be regarded as free electrons with respect to the Compton scattering. For medium and high- $Z$  elements a more realistic approach, which takes into account the energy dependence of the single shell Compton ionization probability, has to be used.

In his work, Stutz [Stutz, 2014] computed the single shell Compton cross section for  $K$  and  $L$  shell on the basis of the impulse approximation for bound electrons states and assessed the energy values at which the Compton interaction becomes the main process of creation of  $K$ -shell vacancies for carbon, aluminum, copper, silver and gold.

In this thesis it is developed a strategy that allows the evaluation of XRF contribution due to Compton ionization for shells  $K$ ,  $L$  and  $M$ , also comparing the obtained Compton cross section with the corresponding photoelectrical one for each considered shell. The mentioned strategy can be summarized in three main points:

1. Compute the single shell Compton cross section  $\sigma_{C_i}$  by means of a mixed procedure involving both WH and IA approximation;
2. Compute the single shell photoelectric cross section  $\tau_i$  using different data libraries;
3. Evaluate the ratio  $\sigma_{C_i}/\tau_i$  in function of the primary photon energy  $E'$ .

The developed strategy is implemented in a FORTRAN deterministic code which allows the computation of the magnitude of interest in a simple way for all elements with  $Z$  from 11 to 92 and for a fixed grid of energies values in a range from 1 to 1000 keV. In what follows all the computational steps of the developed strategy are described.

### 2.6.1 Single shell Compton cross section

To evaluate the single shell Compton cross section a procedure based on the computation of the Compton cross section using both the WH and the IA approximation is used. This mixed procedure allows the evaluation of the magnitude of interest, preserving all the advantages of both approximations. To appreciate the quality of the computation, the obtained intermediate results are compared with the distribution shown by Stutz [Stutz, 2014].

Starting from Eq. 2.23, in a first step of the computation, the Compton scattering function is evaluated in the IA approximation for all shells of the considered elements by using Eq.2.22 to compute the  $Q_{i,MAX}$  for the generic shell  $i$ . The profiles values  $J_i(Q)$  and binding energy  $U_i$  are taken from tabulated data values from Biggs et al. [Biggs, 1975]. This data tabulates the Compton profiles for a fixed set of  $Q$  values ranging from 0 to 100. As the Compton profile is specular respect to the values  $Q=0$ , the distribution for negative  $Q$  values is obtained by simply upset the Biggs tabulated data. An example of the profiles distributions contained in the used data library is shown in Fig. 2.3.

To simplify the computation of the integral in Eq. 2.23, the Compton profiles are expressed as

$$\begin{cases} J_i(Q, Q_{i,MAX}) = J_i(Q) & \text{if } Q \leq Q_{i,MAX} \\ J_i(Q, Q_{i,MAX}) = 0 & \text{if } Q > Q_{i,MAX} \end{cases} \quad (2.31)$$

To evaluate values of the Compton profile at  $Q_{i,MAX}$ , which are not contained in the Biggs data library [Biggs, 1975], it is used the polynomial interpolation by means of the FORTRAN subroutine “**polint.f90**” from the numerical recipes by Press et al. [Press, 1996]. An example of the new Compton profiles expressed as show in Eq. 2.31 is shown in Fig. 2.4.

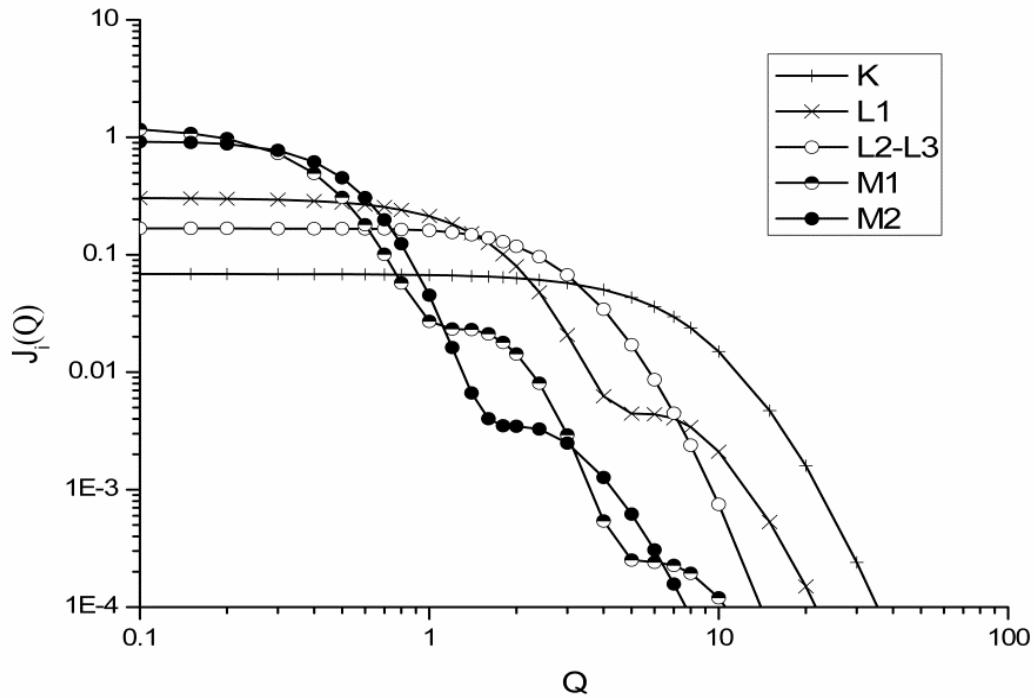


Fig 2.3 Single shells Compton profiles for aluminum. Each distribution is related to a single orbital of the considered atom. The graph is shown in a log-log scale to better appreciate the Profiles distributions. As the Compton profile it is specular with respect  $Q=0$  in the graph it is shown only the distribution related to positive  $Q$  values .

According with the Biggs data library [Biggs, 1975] and expressing the Compton profile as in Eq. 2.31, the single shell Compton scattering function is computed from Eq. 2.23 as

$$S_i^{IA}(E', \theta, Z) = n_{e,i} \int_{-100}^{+100} J_i(Q, Q_{i,MAX}) dQ \quad (2.32)$$

Some examples of the energy distributions obtained for the single shell Compton scattering function  $S_i^{IA}(E', \theta, Z)$  (for a fixed values of the scattering angle  $\theta$ ) are shown in Fig. 2.5.

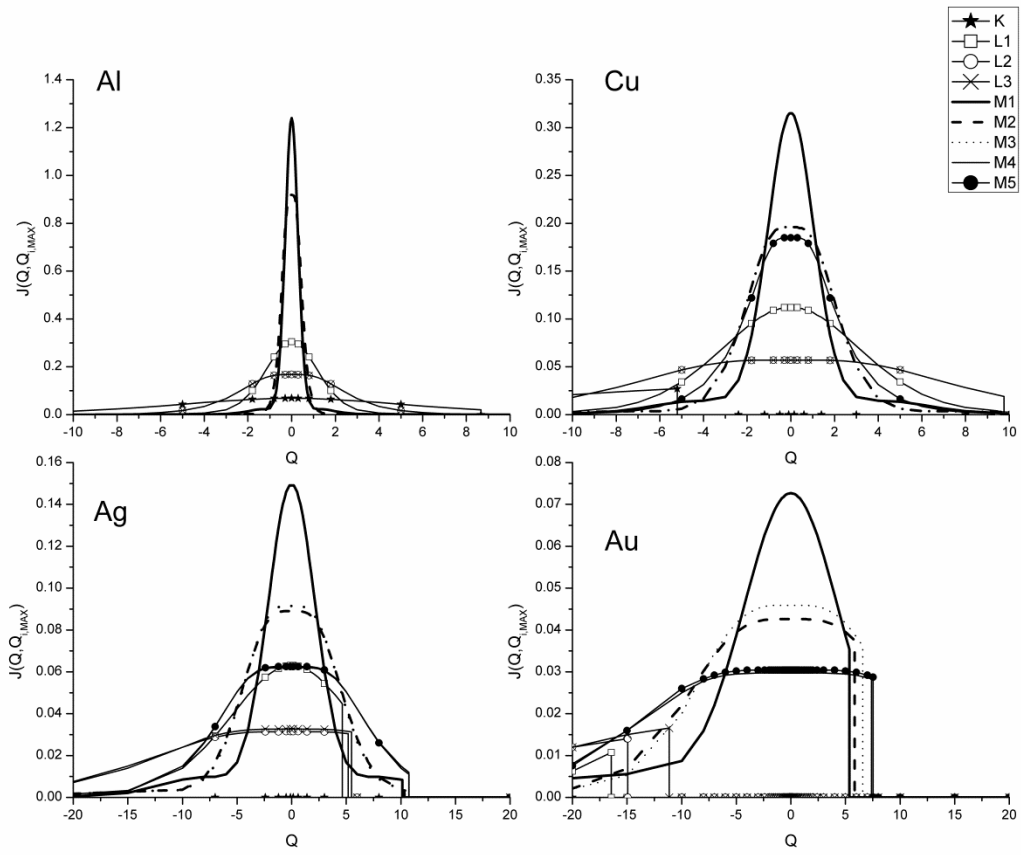


Fig .2.4 Compton profiles  $J_i(Q, Q_{i,MAX})$  of shells K, L1, L2, L3, M1, M2, M3, M4 and M5 computed for aluminum (Al), copper (Cu), silver (Ag) and gold (Au) at  $E' = 60$  keV and  $\theta = \pi/2$ .

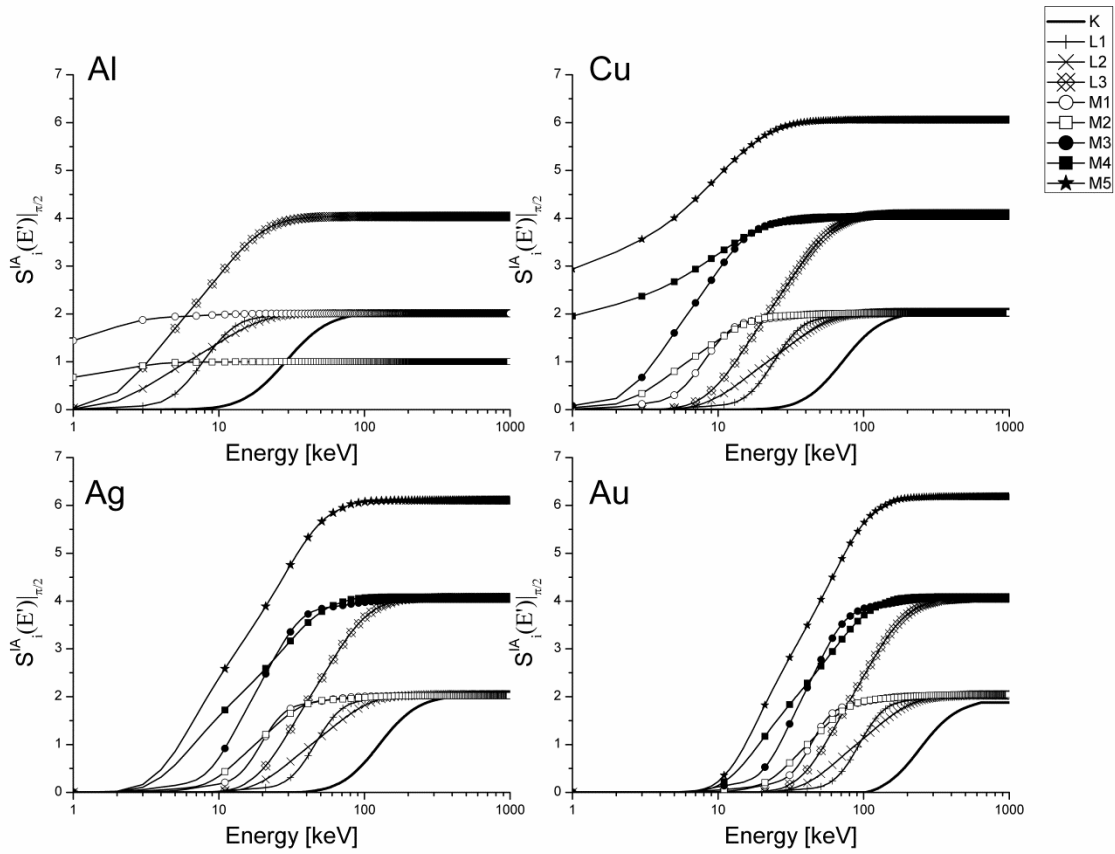


Fig. 2.5. Energy distributions of the single shell Compton scattering function  $S_i^{IA}(E', \theta, Z)$  with fixed scattering angle  $\theta = \pi/2$ , for aluminum (Al), copper (Cu), silver (Ag) and gold (Au). The distributions are related to the shells K, L1, L2, L3, M1, M2, M3, M4, and M5. In aluminum the M3, M4, and M5 shells are not present in the atomic structure of the considered element, and therefore do not appear in the graph.

The single shell scattering function is computed by considering 1000 values of the incoming photon energy  $E'$  ranging from 1 keV to 1000 keV with a constant spacing of 1 keV. As it can be seen from Fig. 2.5, the single shell Compton scattering function is strongly dependent on the energy of the incoming photon  $E'$ . In the plotted distributions it can be appreciated also that the single shell scattering function assumes a values equal to the number of electron belonging to the considered shell as the energy of the incoming photon tends to 1000 keV. This result is due to the property of the Compton profile, for which is valid the relation [Biggs, 1975]:

$$\int_{-\infty}^{+\infty} J_i(Q)dQ = 1 \rightarrow \lim_{E' \rightarrow \infty} S_i^{IA}(E', \theta, Z) = n_{e,i}|_Z \quad (2.33)$$

By computing the single shell scattering function with Eq. 2.32, it is possible to evaluate the single shell Compton cross section in the IA approximation through the relation

$$\sigma_{C_i}^{IA} = \pi r_e^2 \int_0^\pi k_{KN}(E', E_p, \theta) S_i^{IA}(E', \theta, Z) \sin\theta d\theta \quad (2.34)$$

where  $E_p$  is the Compton energy peak computed through Eq. 2.10 and  $k_{KN}(E', E_p, \theta)$  is the Klein-Nishina cross section computed through Eq. 2.12.

The integral in Eq. 2.34 was numerically resolved by using the trapezoidal rule, considering the following scattering angle discretization:

(0.0°, 0.05°, 0.10°, 0.15°, 0.20°, 0.30°, 0.40°, 0.50°, 0.60°, 0.70°, 0.80°, 1.00°, 1.20°, 1.40°, 1.60°, 1.80°, 2.00°, 2.40°, 3.00°, 4.00°, 5.00°, 6.00°, 7.00°, 8.00°, 10.00°, 15.00°, 20.00°, 30.00°, 40.00°, 50.00°, 60.00°, 70.00°, 80.00°, 90.00°, 100.00°, 120.00°, 130.00°, 140.00°, 150.00°, 160.00°, 170.00°, 180.00°).

Some examples of results obtained for the computed single shell Compton cross section are shown in Fig. 2.6, Fig. 2.7 and Fig 2.8. The graphs in Fig. 2.6 and Fig. 2.7 reproduce the distributions in Fig. 4 and Fig. 5, respectively, by Stutz in his work [Stutz, 2014]. It can be appreciated the perfect agreement between the distributions computed by Stutz and our results.

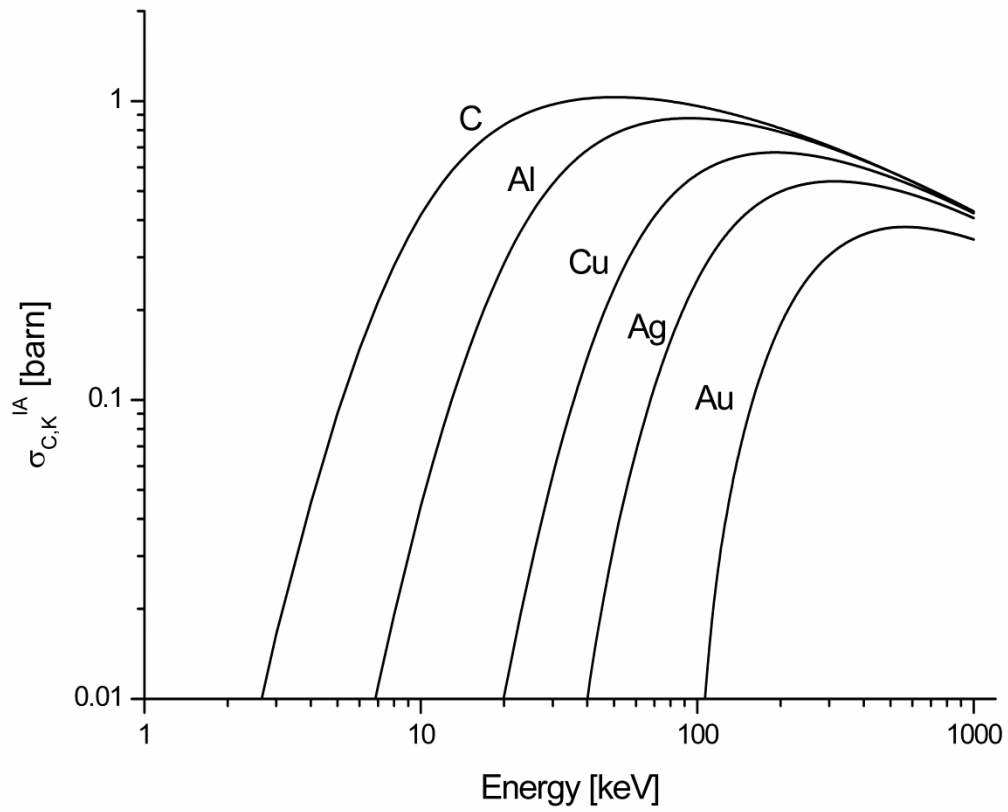


Fig. 2.6. Single shell Compton cross section in the IA approximation for the K shell of C, Al, Cu, Ag and Au. This plot reproduces Fig.4 in Stutz [Stutz, 2014].

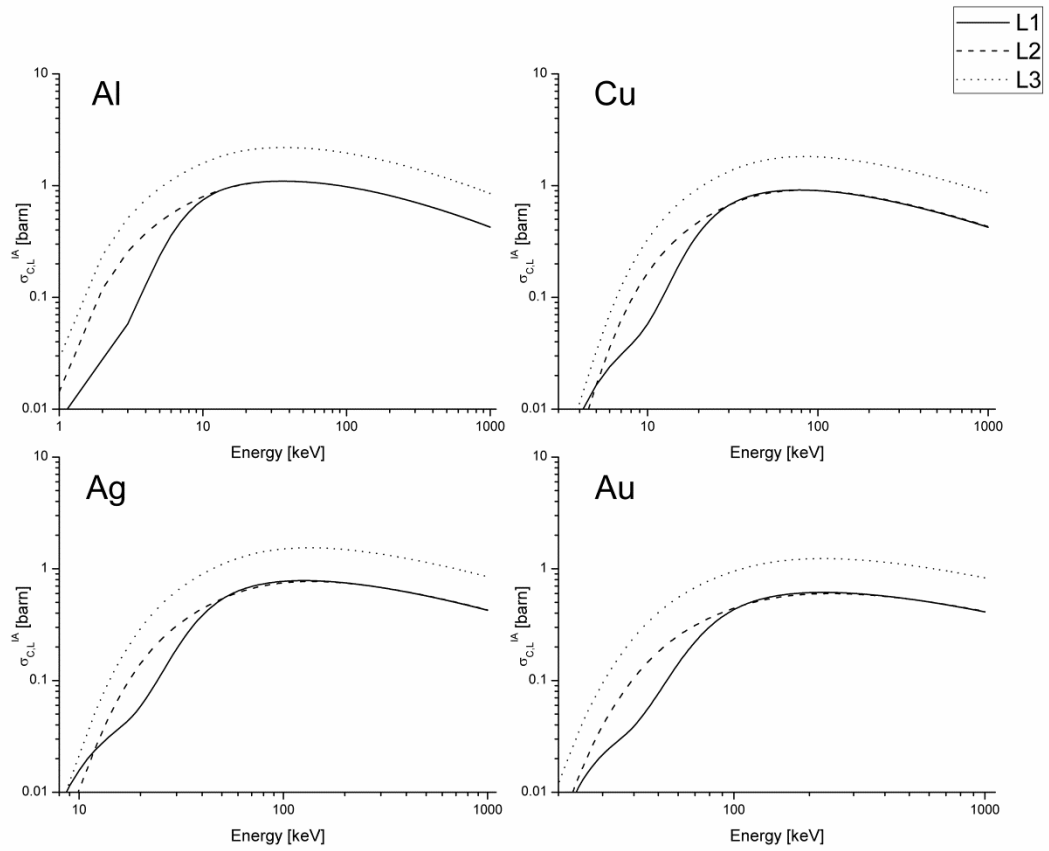


Fig 2.7. Single shell Compton cross section in the IA approximation for the L1 (solid line), L2 (dashed line) and L3 (dotted line) subshell of aluminum (Al), copper (Cu), silver (Ag) and gold (Au). This plot reproduces Fig.5 in Stutz [Stutz, 2014].



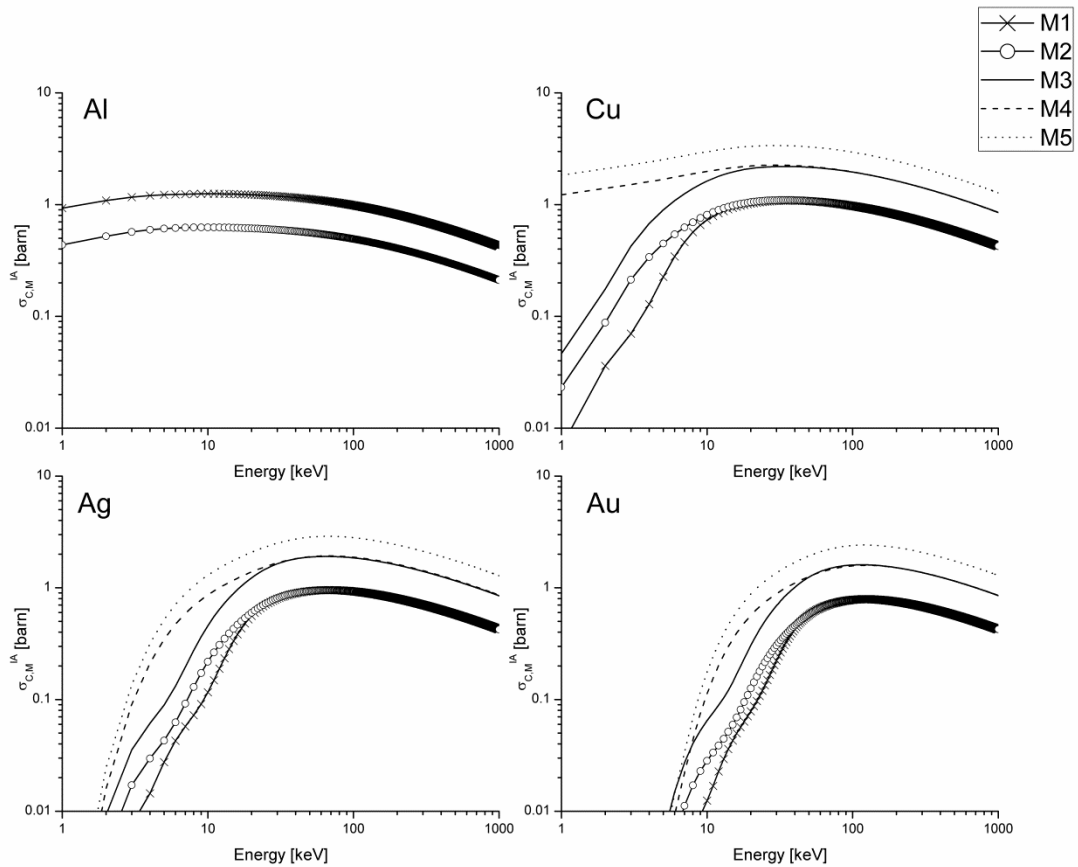


Fig 2.8. Single shell Compton cross section in the IA approximation for the M1 (solid line plus cross), M2 (solid line plus circle), M3 (solid line), M4 (dashed line) and M5 (dotted line) subshell of aluminum (Al), copper (Cu), silver (Ag) and gold (Au).

Even if the IA approximation allows the computation of the Compton cross section for each shell of the considered element in a rather simple way (by the use of the Compton profile) it is well-known that this description fails to evaluate the Compton Cross section when the energy of the primary photon moves closer to the binding energies of the atomic shells. Otherwise, the WH approximation gives a good description of the Compton cross section even in the energy ranges close to the binding energies of the considered element but precludes the possibility to depict the contribution of each single shell to the total Compton cross section.

If we call with  $\sigma_C^{IA}$  and  $\sigma_C^{WH}$  are respectively the total Compton cross section in the IA and in the WH approximation these magnitudes can be computed by integrating Eq. 2.15 and 2.16, over all the outgoing energy  $E$  and scattering angle  $\theta$ , giving the expressions:

$$\sigma_C^{WH} = \pi r_e^2 \int_0^\pi k_{KN}(E', E_p, \theta) S^{WH}(x(E', \theta), Z) \sin\theta d\theta \quad (2.35)$$

$$\sigma_C^{IA} = \pi r_e^2 \int_0^\pi k_{KN}(E', E_p, \theta) \left( \sum_{i=1}^{n\_shells} n_{e,i} \int_{-\infty}^{Q_{i,max}} J_i(Q) dQ \right) \sin\theta d\theta \quad (2.36)$$

where the WH scattering function  $S^{WH}(x(E', \theta), Z)$  in Eq. 2.35 is obtained by interpolating from tables by Cullen et al. [Cullen, 1997]. Some examples of the obtained results for the total Compton cross section in the WH and in the IA approximation are shown in Fig. 2.9. Both these magnitudes are compared with the Compton cross section computed by using attenuation coefficient data tables and fitting functions taken from McMaster [McMaster, 1969]. From the obtained distributions it can be clearly appreciate the good agreement between the McMaster approximation and the Compton cross section computed in the WH approximation. As expected, the distribution of the Compton cross section in the IA approximation shows a departure from the other approximations in the energy range where are located the binding energies of the considered elements. The gap between the two approximations becomes greater as the atomic number of the considered element increases.

To overcome all the possible inaccuracy due to the IA approximation limits, the single shell Compton cross is then computed through the expression:

$$\sigma_{C_i} = \frac{\sigma_{C_i}^{IA}}{\sigma_C^{IA}} \cdot \sigma_C^{WH} \quad (2.37)$$

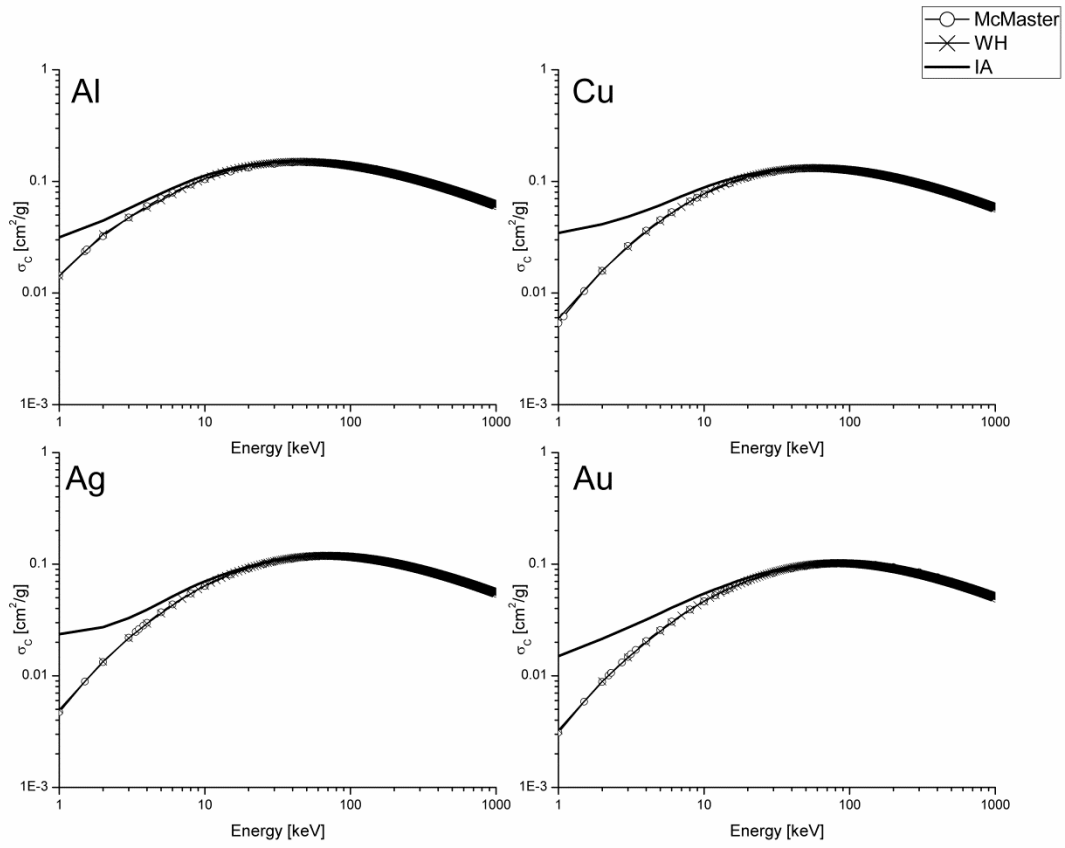


Fig. 2.9. Compton cross section in the McMaster approximation (line plus circle), in the WH approximation (line plus cross) and in the IA approximation for aluminum (Al), copper (Cu), silver (Ag) and gold (Au).

Some example of the final single shell Compton cross section distributions obtained from Eq.2.37 are shown in Fig. 2.10 for the K shell, Fig. 2.11, Fig 2.12, Fig. 2.13 for the L-shells and Fig 2.14, Fig 2.15, Fig 2.16, Fig. 2.17, and Fig 2.18 for the M-shells in comparison with the single shell Compton cross section computed in the IA approximation by using Eq. 2.34.

From the graph showed from Fig. 2.10 to Fig 2.18 it can be seen how the normalization in Eq. 2.37 introduces a correction on the single shell Compton cross section exactly in the low energy region where the IA approximation fails in describing the Compton cross section behavior.

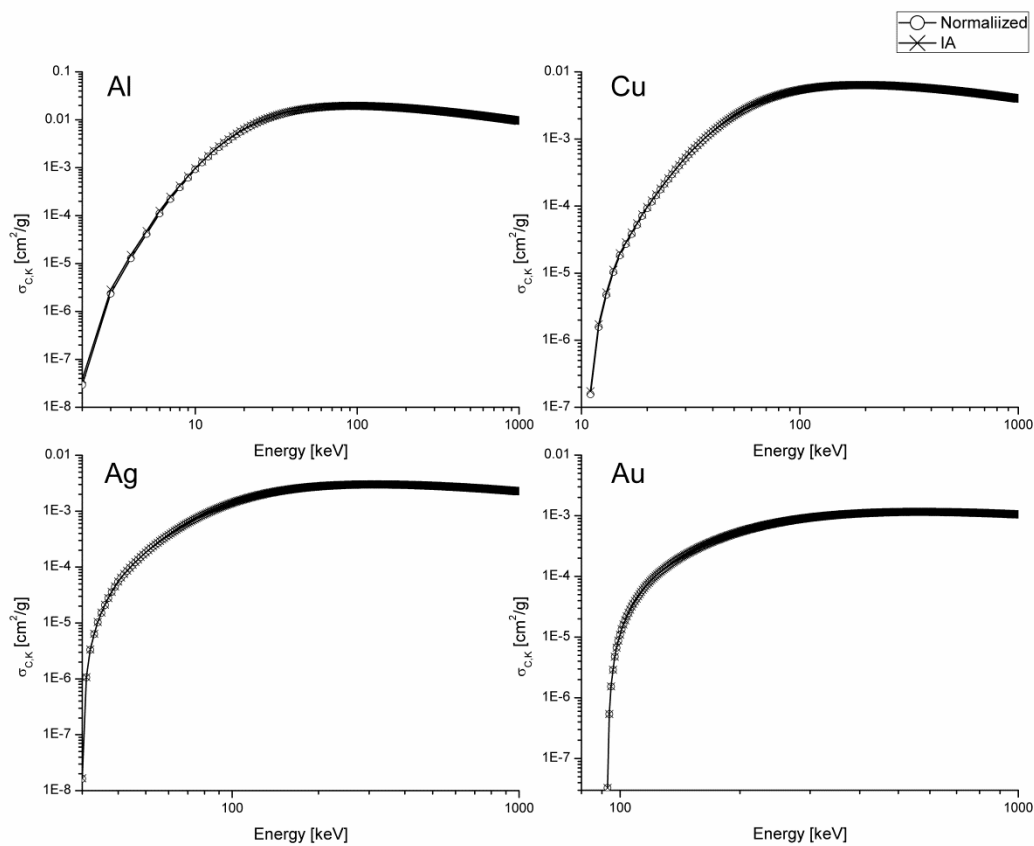


Fig 2.10. Comparison between the single shell Compton cross section computed in the IA approximation (line plus cross), and the normalized single shell Compton cross section computed with Eq. 2.37 (line plus circle). The graph show the single shell Compton cross section of the K-shell for aluminum (Al), copper (Cu), silver (Ag) and gold (Au).

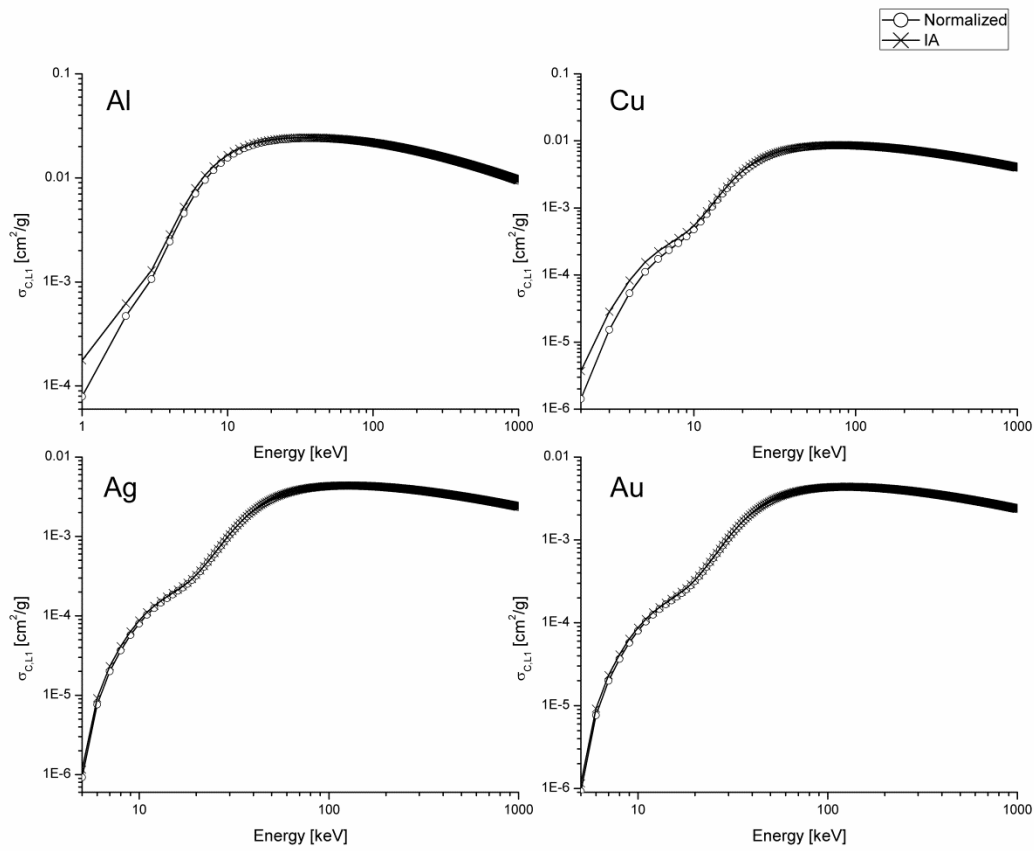


Fig 2.11. Comparison between the single shell Compton cross section computed in the IA approximation (line plus cross), and the normalized single shell Compton cross section computed with Eq. 2.37 (line plus circle). The graph shows the single shell Compton cross section of the L1-shell for aluminum (Al), copper (Cu), silver (Ag) and gold (Au).

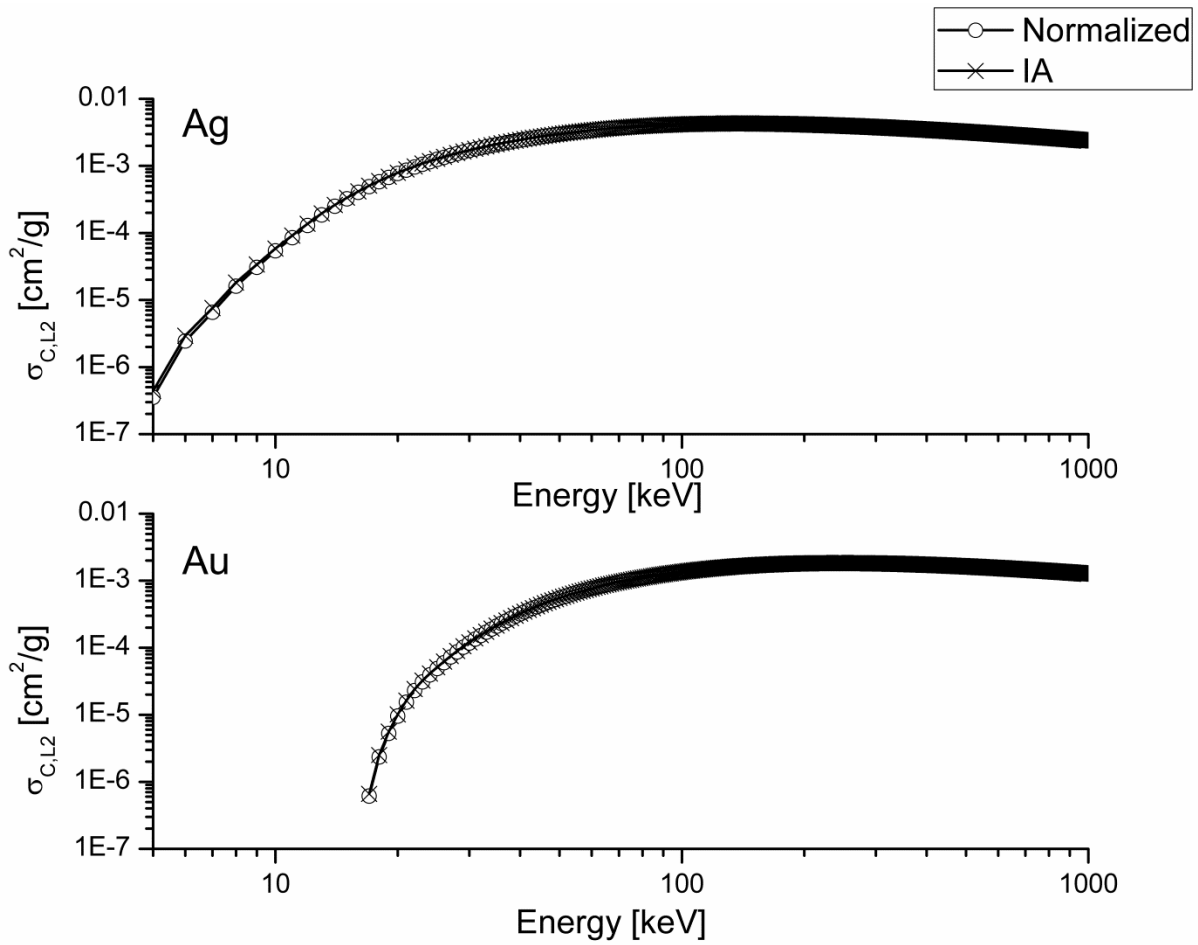


Fig 2.12. Comparison between the single shell Compton cross section computed in the IA approximation (line plus cross), and the normalized single shell Compton cross section computed with Eq. 2.37 (line plus circle). The graph shows the single shell Compton cross section of the L2-shell for silver (Ag) and gold (Au).

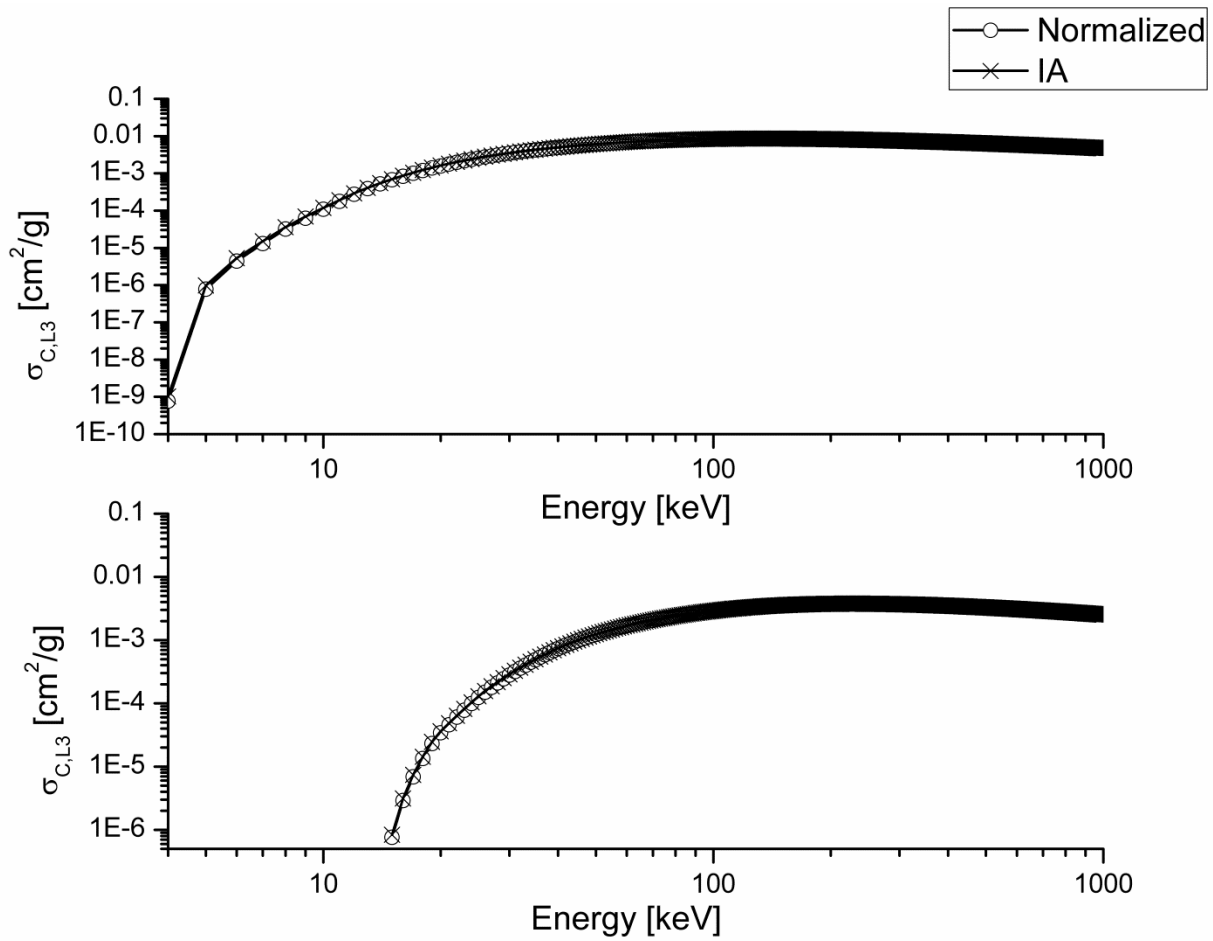


Fig 2.13. Comparison between the single shell Compton cross section computed in the IA approximation (line plus cross), and the normalized single shell Compton cross section computed with Eq. 2.37 (line plus circle). The graph shows the single shell Compton cross section of the L3-shell for silver (Ag) and gold (Au).

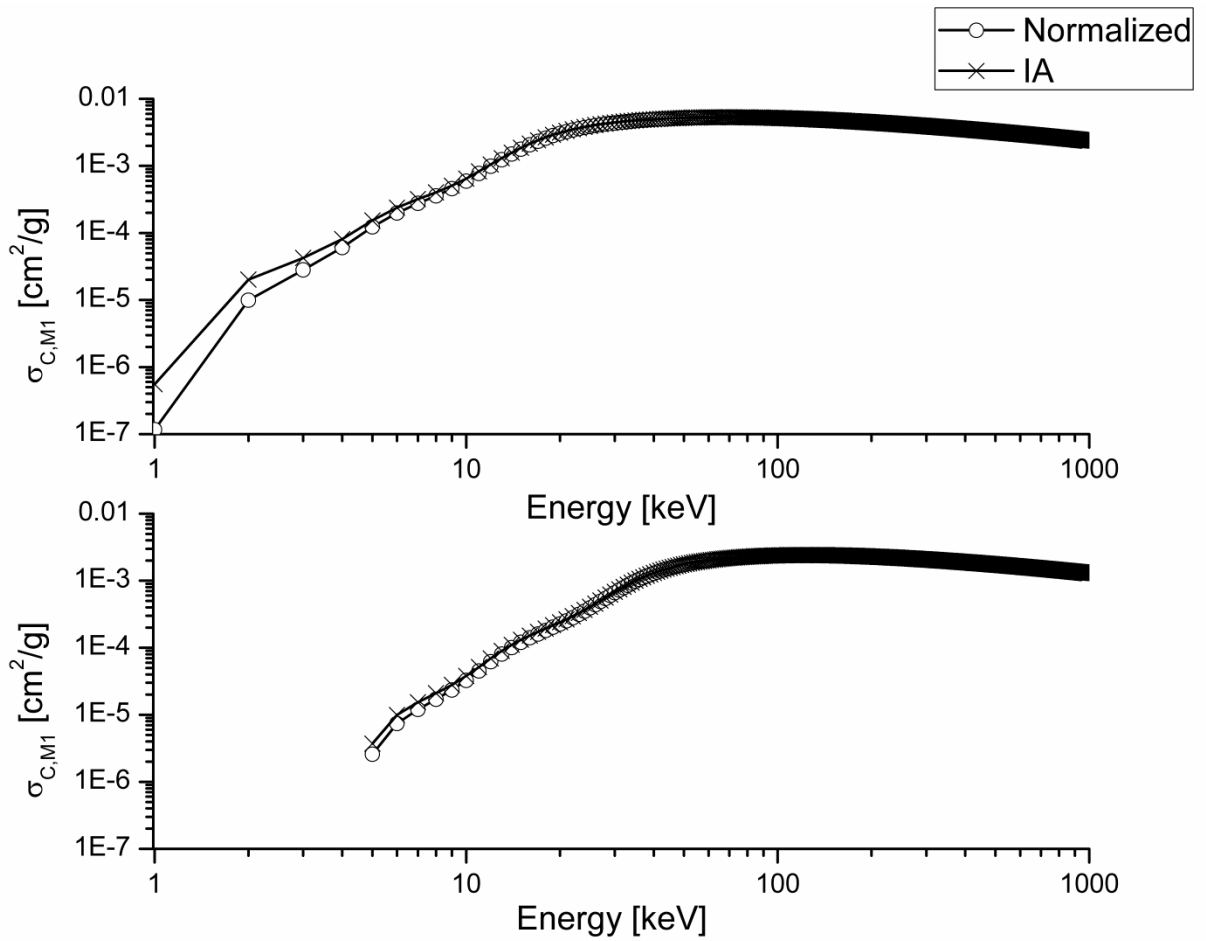


Fig 2.14. Comparison between the single shell Compton cross section computed in the IA approximation (line plus cross), and the normalized single shell Compton cross section computed with Eq. 2.37 (line plus circle). The graph shows the single shell Compton cross section of the M1-shell for silver (Ag) and gold (Au).



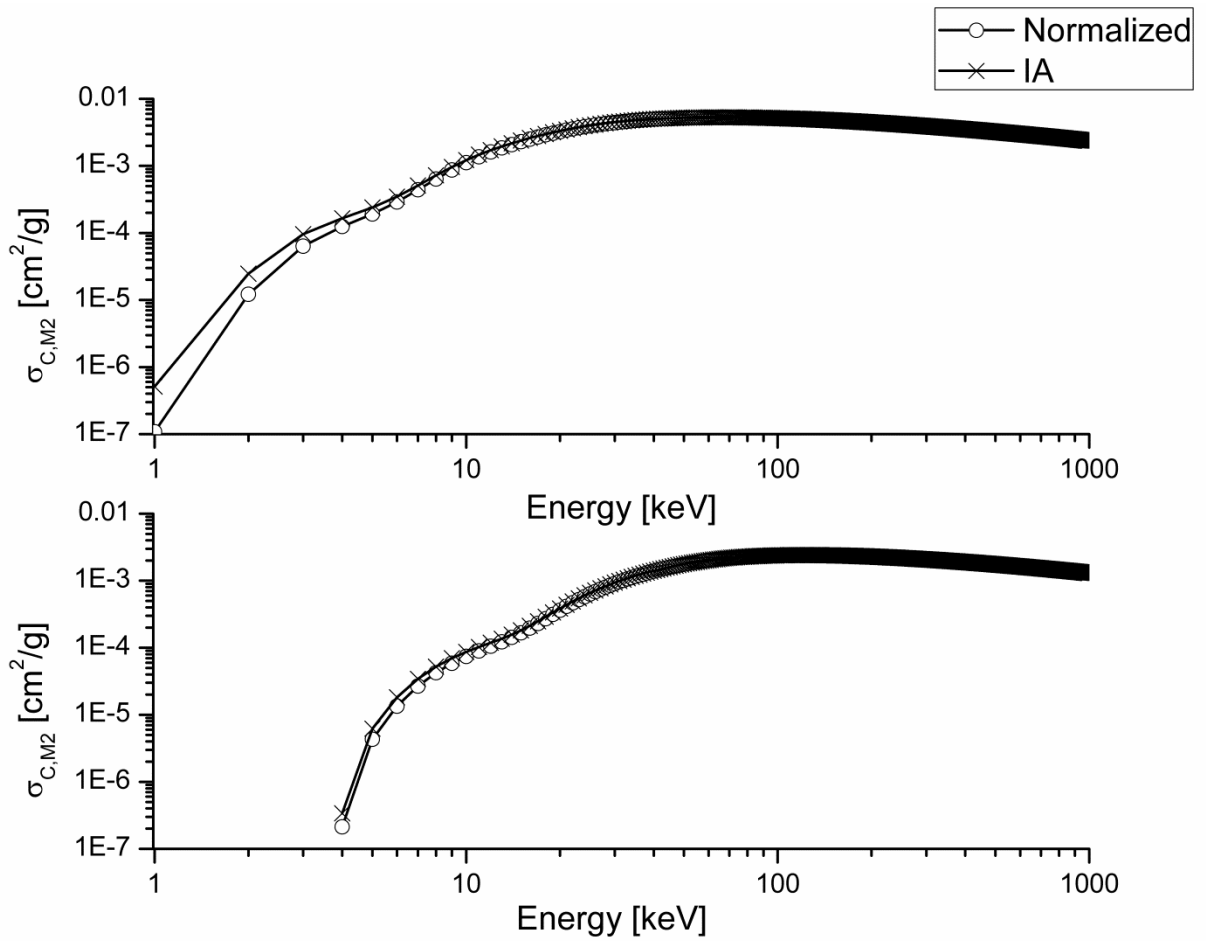


Fig 2.15. Comparison between the single shell Compton cross section computed in the IA approximation (line plus cross), and the normalized single shell Compton cross section computed with Eq. 2.37 (line plus circle). The graph shows the single shell Compton cross section of the M2-shell for silver (Ag) and gold (Au).

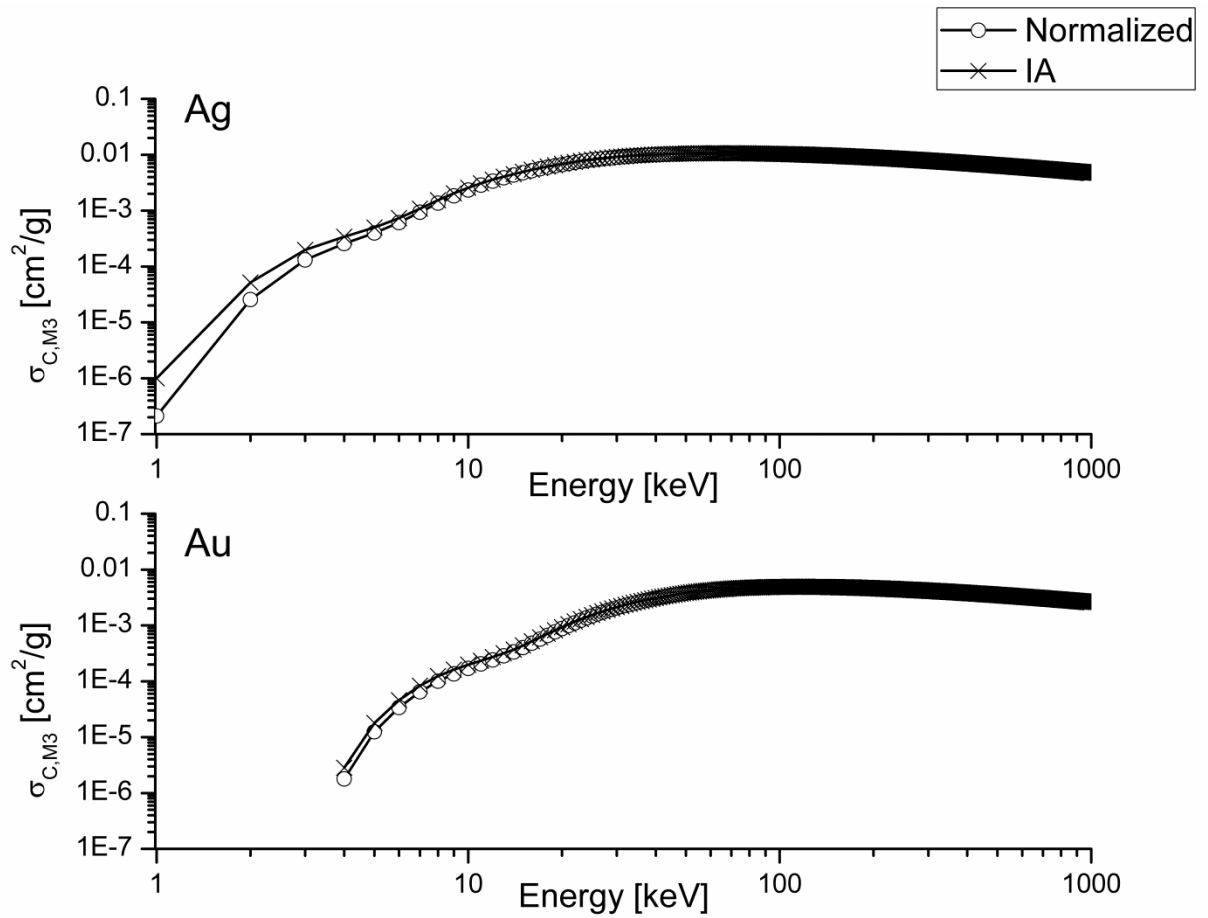


Fig 2.16. Comparison between the single shell Compton cross section computed in the IA approximation (line plus cross), and the normalized single shell Compton cross section computed with Eq. 2.37 (line plus circle). The graph shows the single shell Compton cross section of the M3-shell for silver (Ag) and gold (Au).

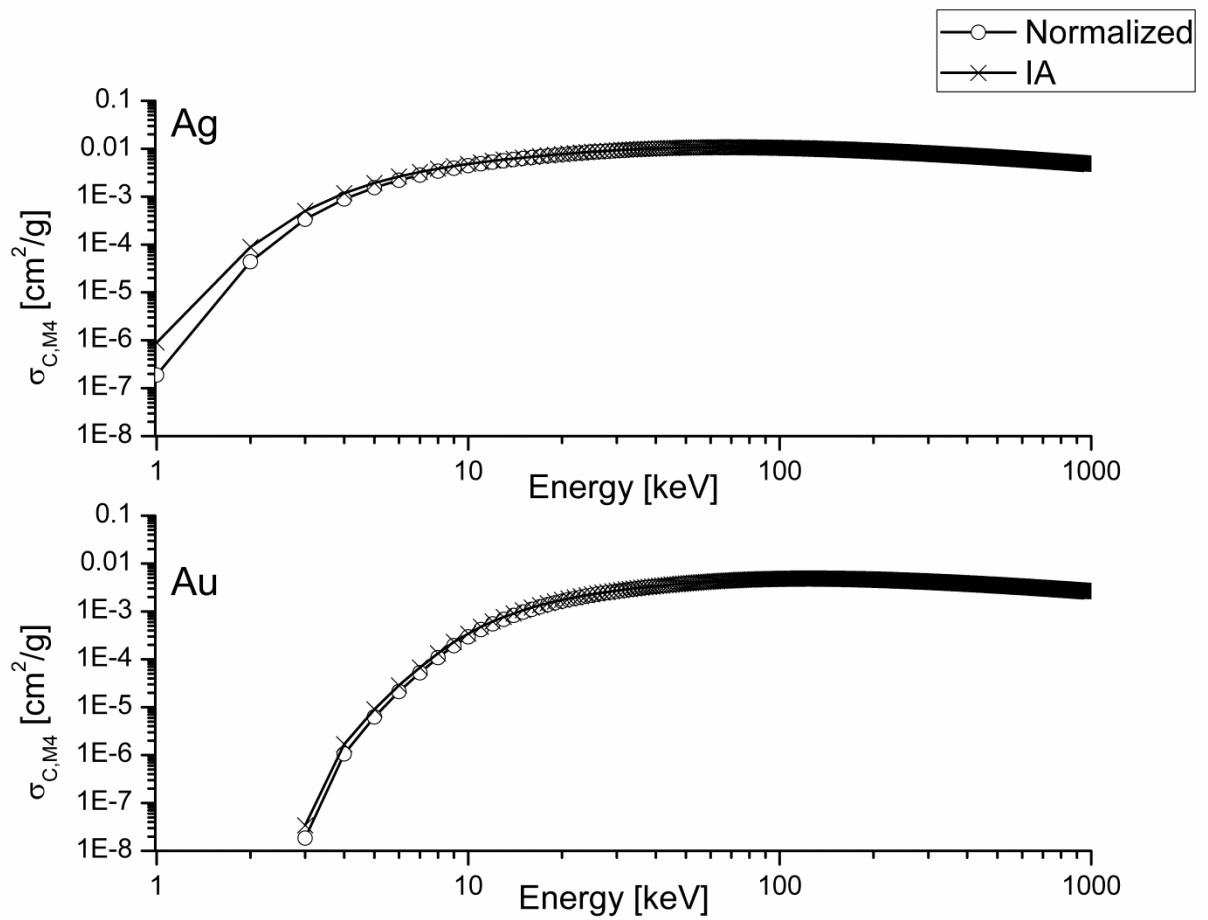


Fig 2.17. Comparison between the single shell Compton cross section computed in the IA approximation (line plus cross), and the normalized single shell Compton cross section computed with Eq. 2.37 (line plus circle). The graph shows the single shell Compton cross section of the M4-shell for silver (Ag) and gold (Au).

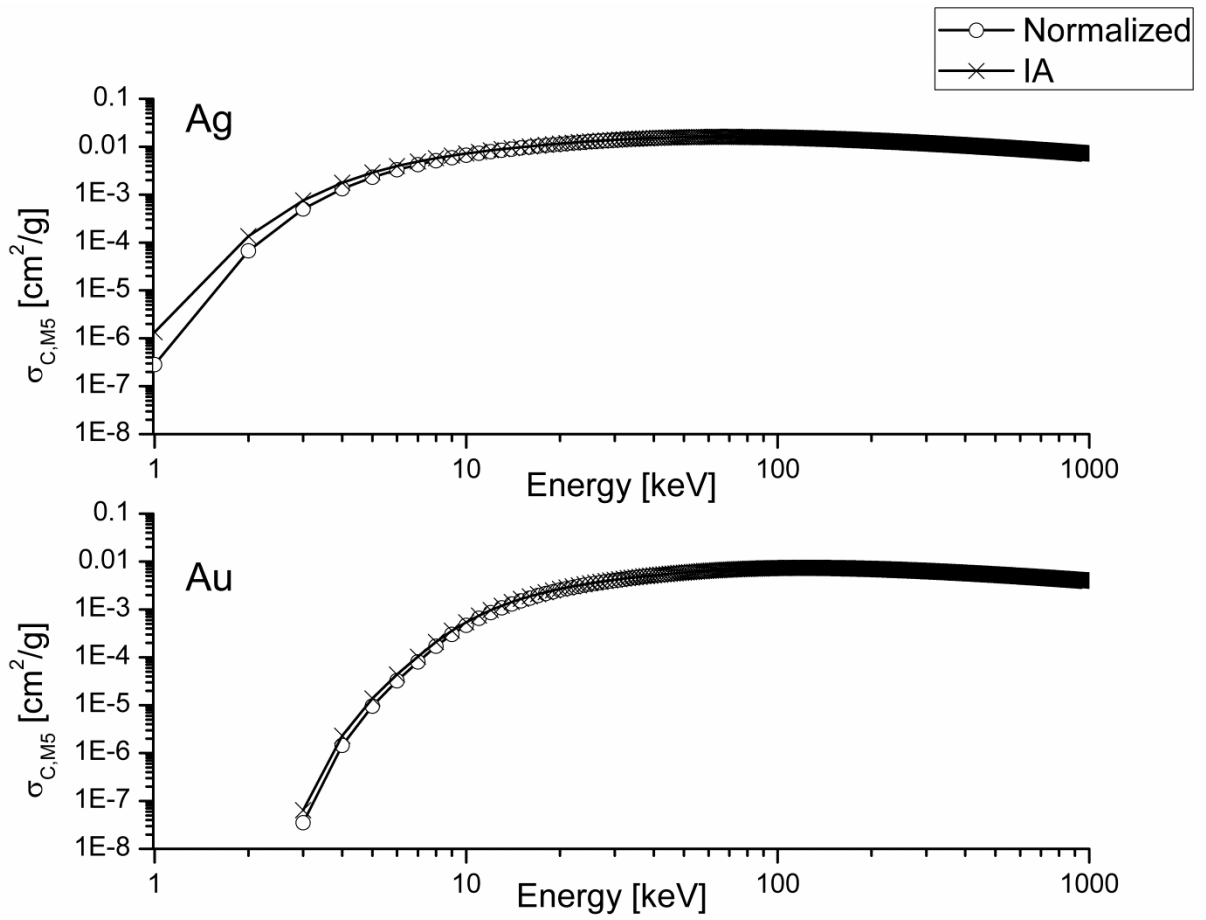


Fig 2.18. Comparison between the single shell Compton cross section computed in the IA approximation (line plus cross), and the normalized single shell Compton cross section computed with Eq. 2.37 (line plus circle). The graph shows the single shell Compton cross section of the M5 shell for silver (Ag) and gold (Au).

## 2.6.2 Single shell photoelectric cross section

The single shell photoelectric cross section  $\tau_i$  is evaluated by using two different data library approximations:

- The EPDL97 database from Cullen et al. [Cullen, 1997].
- The attenuation coefficient data tables and fitting functions taken from McMaster et al. [McMaster, 1969].

The EPDL97 library contains photoelectric cross sections for all shells of the elements with  $Z$  from 1 to 100 and photon energies from 1 eV to 1000 GeV, derived from Scofield's theoretical calculations of shell cross sections [Saloman, 1988] and Hubbell's total cross sections [Hubbell, 1980]; [Berger, 1987]. In our computation it is used the PENELOPE database (extracted from the EPDL97) [Salvat, 2011] which contains the photoelectric total atomic cross section and partial cross sections for photoionization of K, L, M and N shells, for all elements with  $ZZ=1-99$ , in the energy range 50eV-1TeV. The data are taken from Cullen et al. 1997 [Cullen, 1997]. To compute the value of the partial cross sections for an arbitrary energy from the PENELOPE data base a polynomial interpolation procedure is used.

The McMaster data tables let to compute the total photoelectric cross section for elements with  $Z$  from 1 to 92. From these data tables, as shown in Fernandez [Fernandez, 1989], the single shell photoelectric cross section  $\tau_i$  can be computed by using the following equation system:

$$\left\{ \begin{array}{l} \tau_K = \tau(1 - r_K) \\ \tau_{L1} = \tau r_K(1 - r_{L1}) \\ \tau_{L2} = \tau r_K r_{L1}(1 - r_{L2}) \\ \tau_{L3} = \tau r_K r_{L1} r_{L2}(1 - r_{L3}) \\ \tau_{M1} = \tau r_K r_{L1} r_{L2} r_{L3}(1 - r_{M1}) \\ \tau_{M2} = \tau r_K r_{L1} r_{L2} r_{L3} r_{M1}(1 - r_{M2}) \\ \tau_{M3} = \tau r_K r_{L1} r_{L2} r_{L3} r_{M1} r_{M2}(1 - r_{M3}) \\ \tau_{M4} = \tau r_K r_{L1} r_{L2} r_{L3} r_{M1} r_{M2} r_{M3}(1 - r_{M4}) \\ \tau_{M5} = \tau r_K r_{L1} r_{L2} r_{L3} r_{M1} r_{M2} r_{M3} r_{M4}(1 - r_{M5}) \end{array} \right. \quad \text{with} \quad \left\{ \begin{array}{l} r_i = \frac{1}{j_i} \text{ for } E' \geq U_i \\ r_i = 1 \text{ for } E' < U_i \end{array} \right. \quad (2.38)$$

where  $\tau$  is the total photoelectric cross section computed from the McMaster data tables,  $\tau_i$  and  $U_i$  are respectively the single shell photoelectric cross section and the binding energy of the shell  $i$  for the considered element, and  $j_i$  is the absorption edge jump of the shell  $i$  as tabulated by Scofield [Scofield, 1973].

Some examples of the obtained single shell photoelectric cross section by using the two different data library are shown in Fig. 2.19 for the K shell, Fig. 2.20 for the L shells and Fig 2.21 for the M shells.

From Fig. 2.19 it can be seen an almost perfect agreement between the two used data library for the K shells. From Fig. 2.20 and Fig 2.21 it can be noted an apparent discrepancies that for L and M shells discrepancies are apparent.

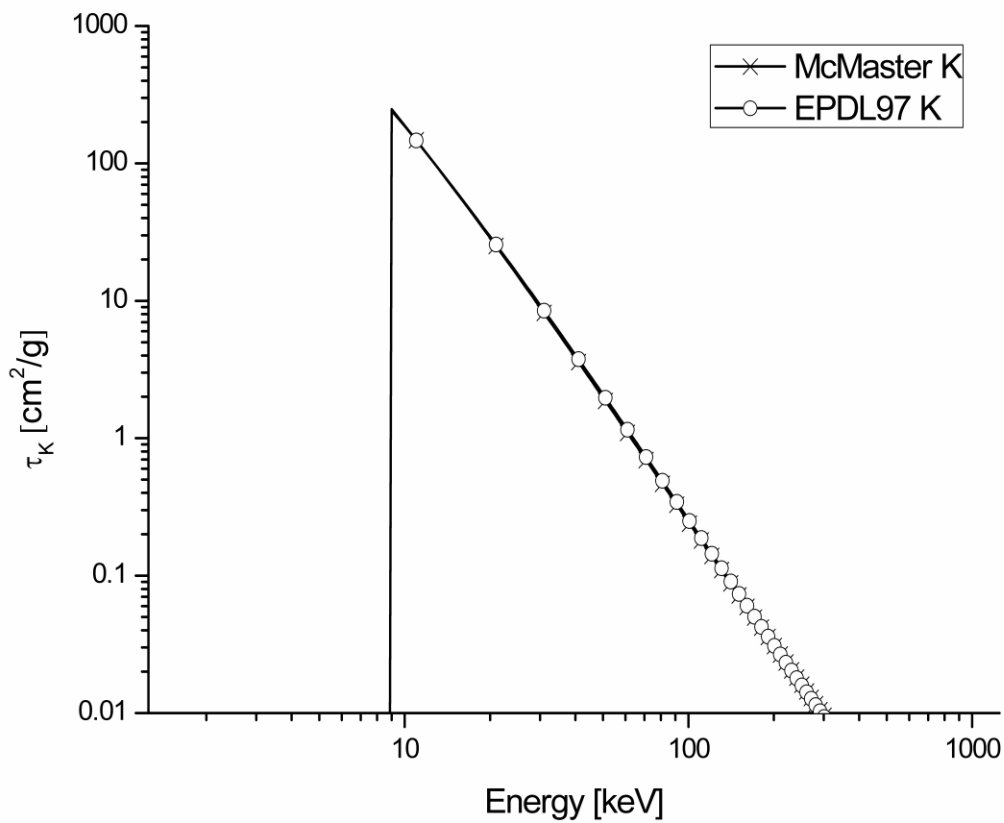


Fig. 2.19. Comparison of the single shell photoelectric cross section from the McMaster data library and the EPDL97 data library for the K shell of copper.

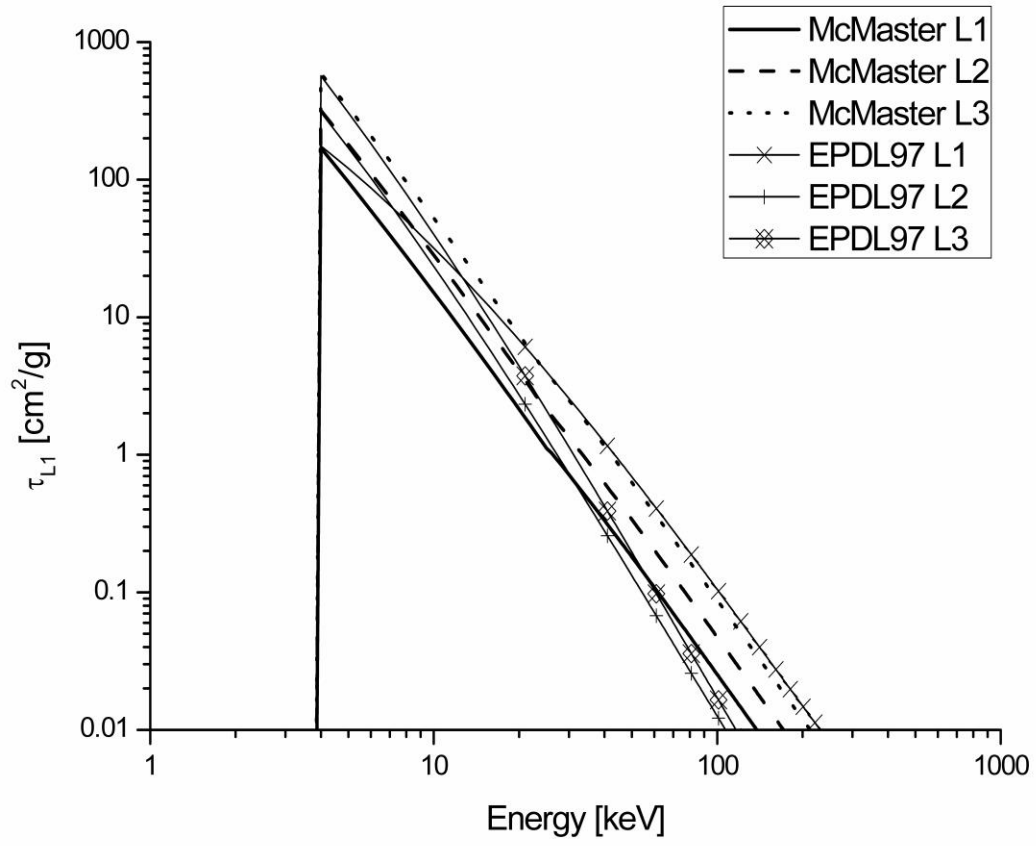


Fig. 2.20. Comparison of the single shell photoelectric cross section from the McMaster data library and the EPDL97 data library for the L shells of silver.

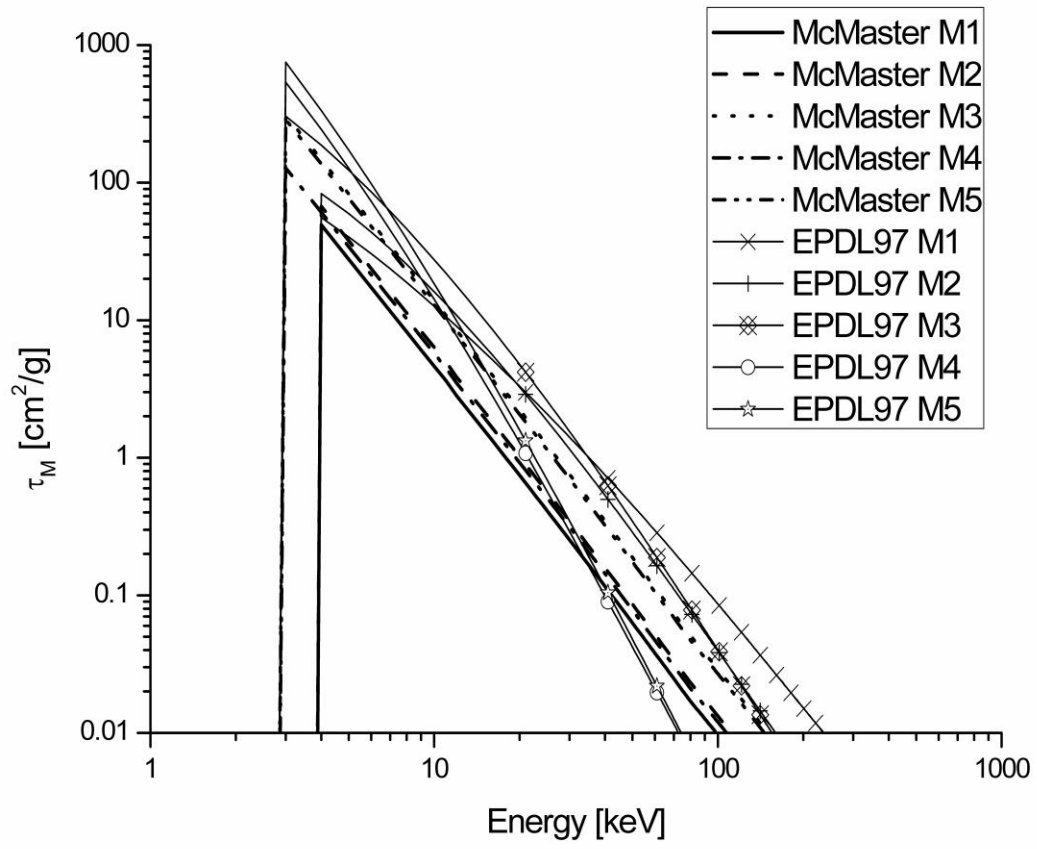


Fig. 2.21. Comparison of the single shell photoelectric cross section from the McMaster data library and the EPDL97 data library for the M shells of gold.



### 2.6.3 Single shell photoelectric-Compton cross section ratio

Some values of single shell Compton cross section and single shell photoelectric cross section evaluated as described in the previous sections are compared with the corresponding ones given by Stutz [Stutz, 2014]. Tab. 2.1 reproduces the Table 1 from [Stutz, 2014]. Tab 2.2 shows some values of the single shell Compton cross section and photoelectric cross section computed with our strategy.

Element	Energy [keV]	$\sigma_{C_K}$ [barn/atom]	$\tau$ [barn/atom]	$\sigma_{C_K} + \tau$ [barn/atom]	$\tau/\sigma_{C_K}$ [barn/atom]
Cu	279	0.640	1.239	1.879	1.936
Ag	145	0.334	67.205	67.539	201.213
	279	0.511	10.302	10.813	20.160
	662	0.465	1.087	1.552	2.338
	1250	0.357	0.276	0.633	0.773
Au	662	0.377	10.490	10.867	27.825
	1250	0.321	2.755	3.076	8.583

Tab. 2.1. Partial Compton cross section for K shells and photoelectric cross sections of some elements, as reported in Table 1 of the Stutz work [Stutz, 2014].

Element	Energy [keV]	$\sigma_{C_K}$ [barn/atom]	$\tau$ [barn/atom]	$\sigma_{C_K} + \tau$ [barn/atom]	$\tau/\sigma_{C_K}$ [barn/atom]
Cu	250	0.65237	1.71529	2.368	2.629
	300	0.63277	1.01466	1.647	1.604
Ag	140	0.39103	72.25569	72.647	184.781
	150	0.41570	59.22939	59.645	142.482
	250	0.52295	13.80491	14.328	26.398
	300	0.53199	8.30171	8.834	15.605
	650	0.46845	1.08082	1.549	2.307
	1000	0.40036	0.39036	0.791	0.975
Au	650	0.37196	10.16324	10.535	27.323
	1000	0.33980	4.22468	4.564	12.433

Tab. 2.2. Single shell Compton cross section and photoelectric cross sections for K shells of some elements computed with our procedure. Cross sections are in b/atom.

As it can be seen from Tab 2.1 and Tab 2.2 the results obtained with our computational strategy are in very good agreement with Stutz's results.

For each element with  $Z$  from 11 to 92 the ratio  $\sigma_{C_i}/\tau_i$  is evaluated in function of the primary photon energy  $E'$ , for the shells K, L1, L2, L3, M1, M2, M3, M4, and M5. Some examples of the obtained distributions are showed in Fig. 2.20, Fig. 2.21 and Fig. 2.22.

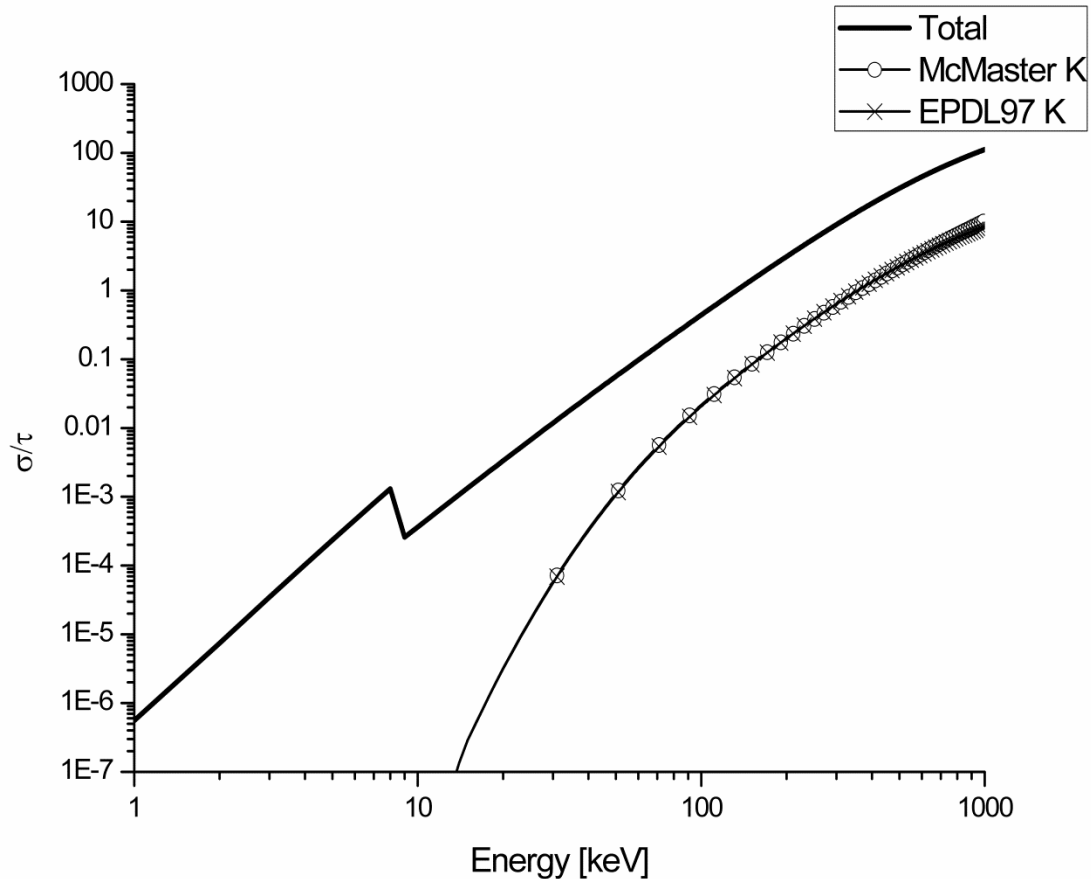


Fig 2.20. Single shell Compton-photoelectric cross section ratio. In the graph are compared the  $\sigma_{C_K}/\tau_K$  distribution for the K shell of copper with the photoelectric cross section computed from the McMaster library (McMaster K) and from the EPDL97 database (EPDL97 K). The solid line represents the total Compton-photoelectric cross section ratio for the considered element. As expected in this case it can be seen how between the two used libraries there are not significant differences in the K-shell ratio description.

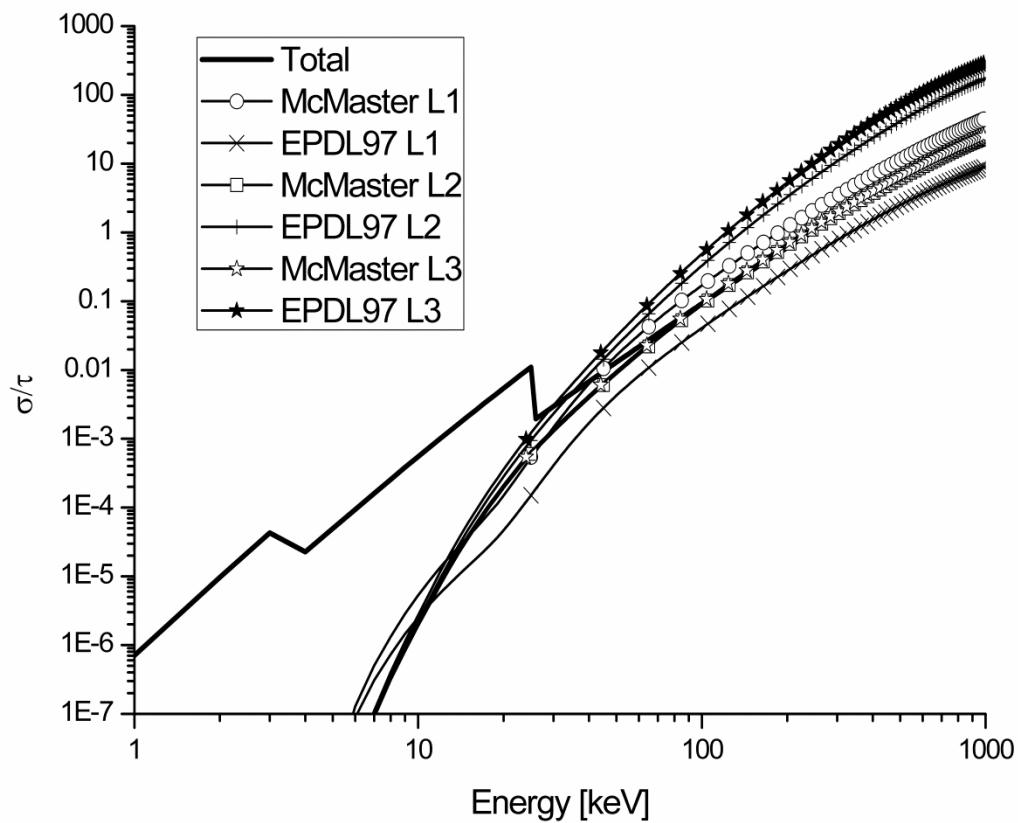


Fig 2.21. Single shell Compton-photoelectric cross section ratio. In the graph are compared the  $\sigma_{C_L}/\tau_L$  distribution for the L shells of silver with the photoelectric cross section computed from the McMaster library (McMaster L1, McMaster L2 and McMaster L3) and from the EPDL97 database (EPDL97 L1, EPDL97 L2 and EPDL97 L3). The solid line represents the total Compton-photoelectric cross section ratio for the considered element. In this case it can be seen how the gap between the two used libraries introduces significant differences for the computed distribution in all the considered energy range.

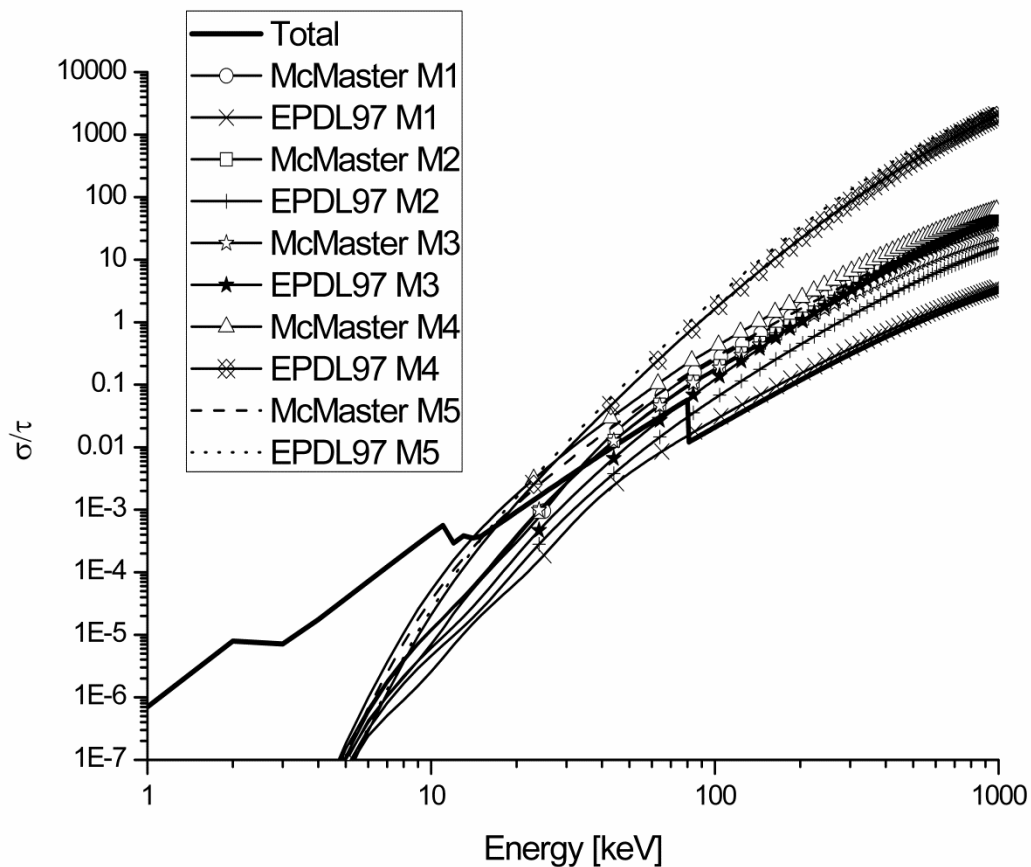


Fig 2.22. Single shell Compton-photoelectric cross section ratio. In the graph are compared the  $\sigma_{C_M}/\tau_M$  distribution for the M shells of gold with the photoelectric cross section computed from the McMaster library (McMaster M1, McMaster M2, McMaster M3, McMaster M4 and McMaster M5) and from the EPDL97 database (EPDL97 M1, EPDL97 M2, EPDL97 M3, EPDL97 M4 and EPDL97 M5). The solid line represents the total Compton-photoelectric cross section ratio for the considered element. In this case it can be seen how the gap between the two used libraries introduces significant differences for the computed distribution in all the considered energy range.

Starting from these results it is developed a FORTRAN code that allows, for each shell of all considered elements, the computation of the energy values  $E'(Z)$  for which the ratio  $\sigma_{C_i}/\tau_i$  becomes bigger than an arbitrary fixed percentage value. In Fig. 2.23, Fig. 2.24, Fig. 2.25, Fig. 2.26, Fig. 2.27, Fig. 2.28, Fig. 2.29, Fig. 2.30 and Fig. 2.31 are shown the distributions obtained with the developed code for values of the ratio  $\sigma_{C_i}/\tau_i$  equal to 1%, 5%, 10%, 20%, 50%, and 100%, respectively for the shells K, L1, L2, L3, M1, M2, M3, M4, and M5.

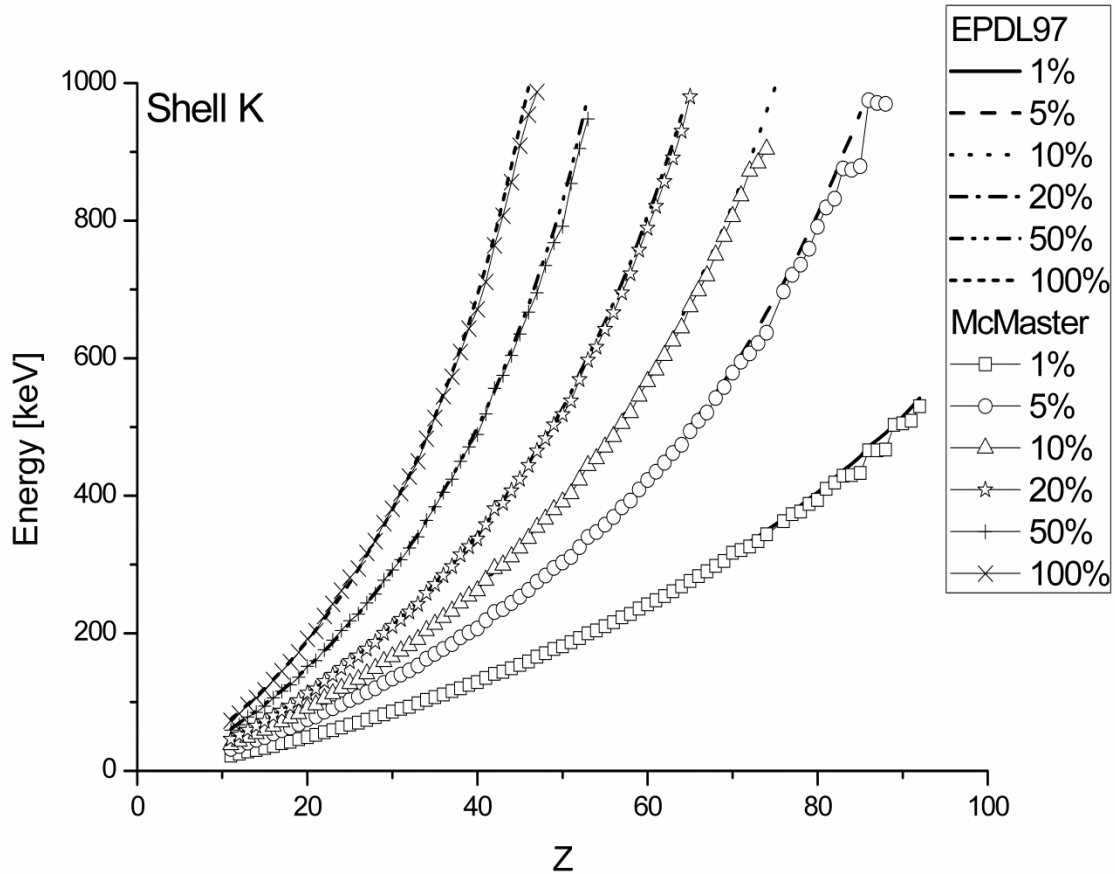


Fig 2.23. Values of the energy in keV, as a function of the atomic number  $Z$ , for which  $\frac{\sigma_k}{\tau_k}$  is bigger than 1%, 5%, 10%, 20%, 50% and 100%. This value is computed both using the McMaster and the EPDL97 database.

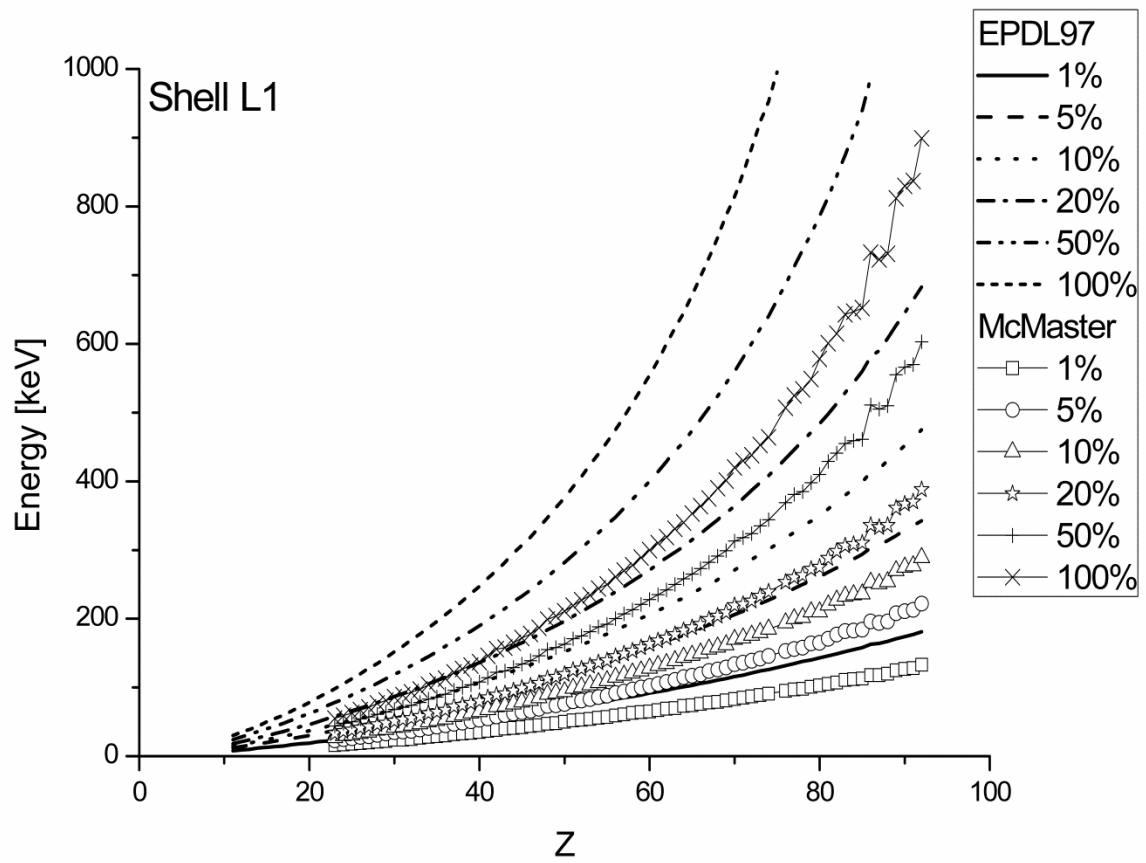


Fig 2.24. Values of the energy in keV, as a function of the atomic number Z, for which  $\frac{\sigma_{L1}}{\tau_{L1}}$  is bigger than 1%, 5%, 10%, 20%, 50% and 100%. This value is computed both using the McMaster and the EPDL97 database.

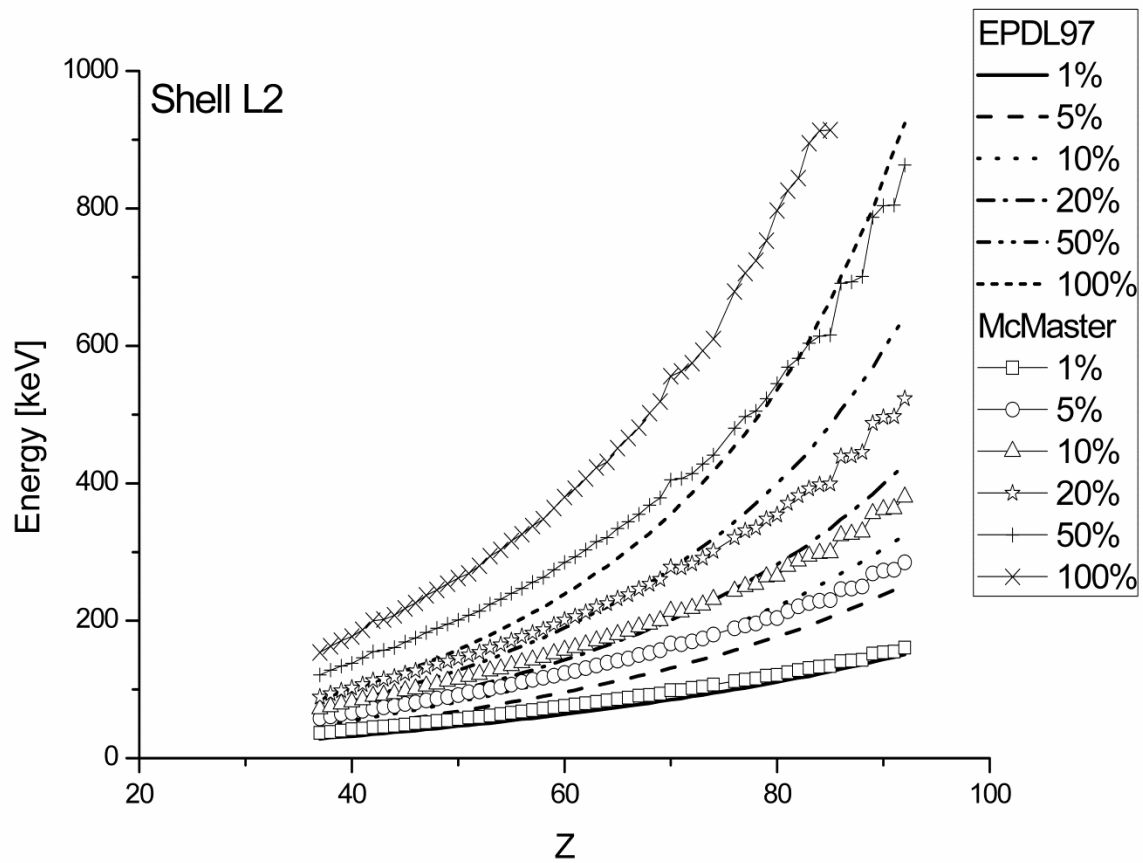


Fig 2.25. Values of the energy in keV, as a function of the atomic number  $Z$ , for which  $\frac{\sigma_{L2}}{\tau_{L2}}$  is bigger than 1%, 5%, 10%, 20%, 50% and 100%. This value is computed both using the McMaster and the EPDL97 database.

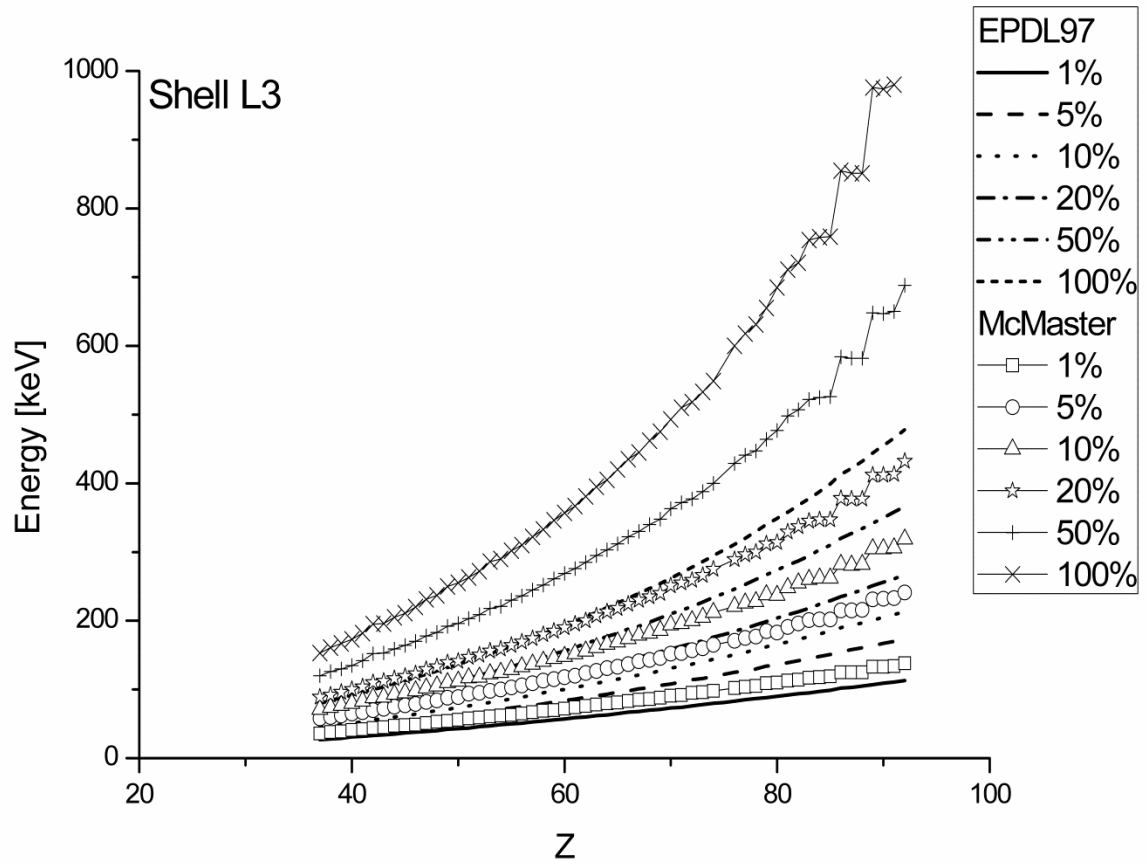


Fig 2.26. Values of the energy in keV, as a function of the atomic number Z, for which  $\frac{\sigma_{L3}}{\tau_{L3}}$  is bigger than 1%, 5%, 10%, 20%, 50% and 100%. This value is computed both using the McMaster and the EPDL97 database.



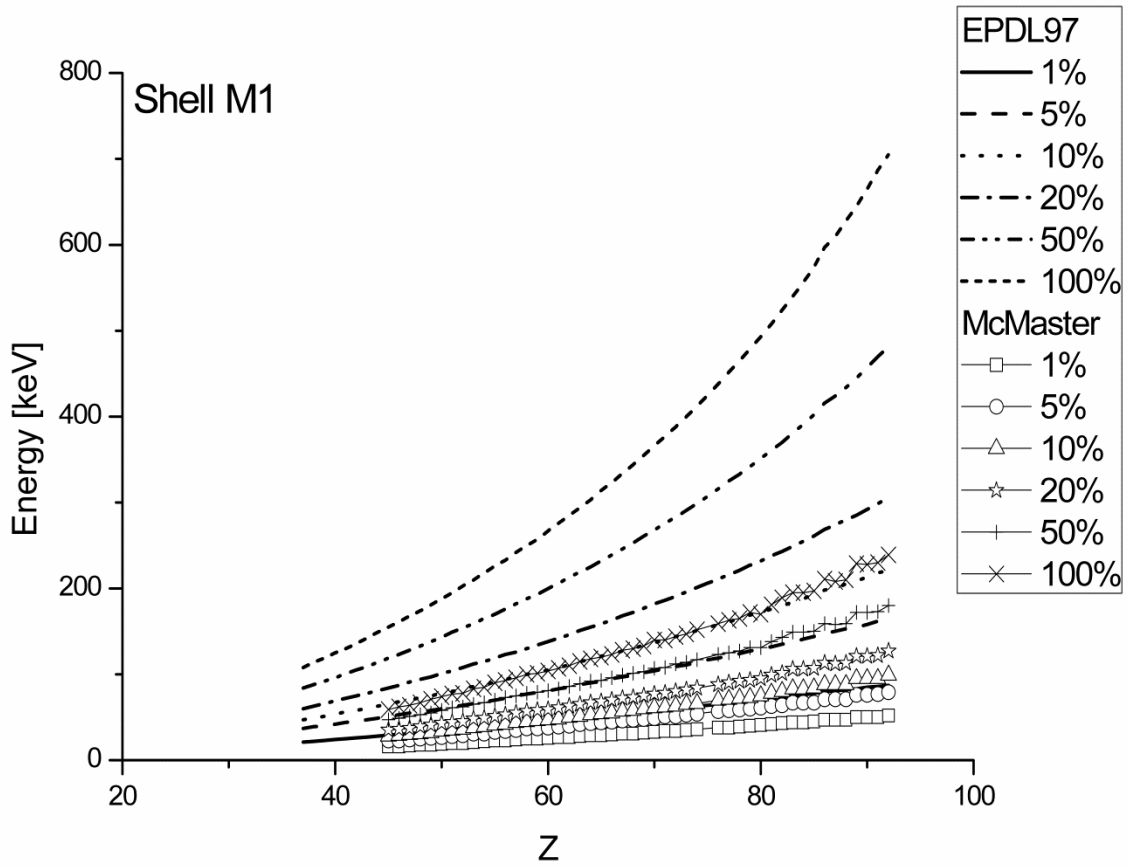


Fig 2.27. Values of the energy in keV, as a function of the atomic number  $Z$ , for which  $\frac{\sigma_{M1}}{\tau_{M1}}$  is bigger than 1%, 5%, 10%, 20%, 50% and 100%. This value is computed both using the McMaster and the EPDL97 database.

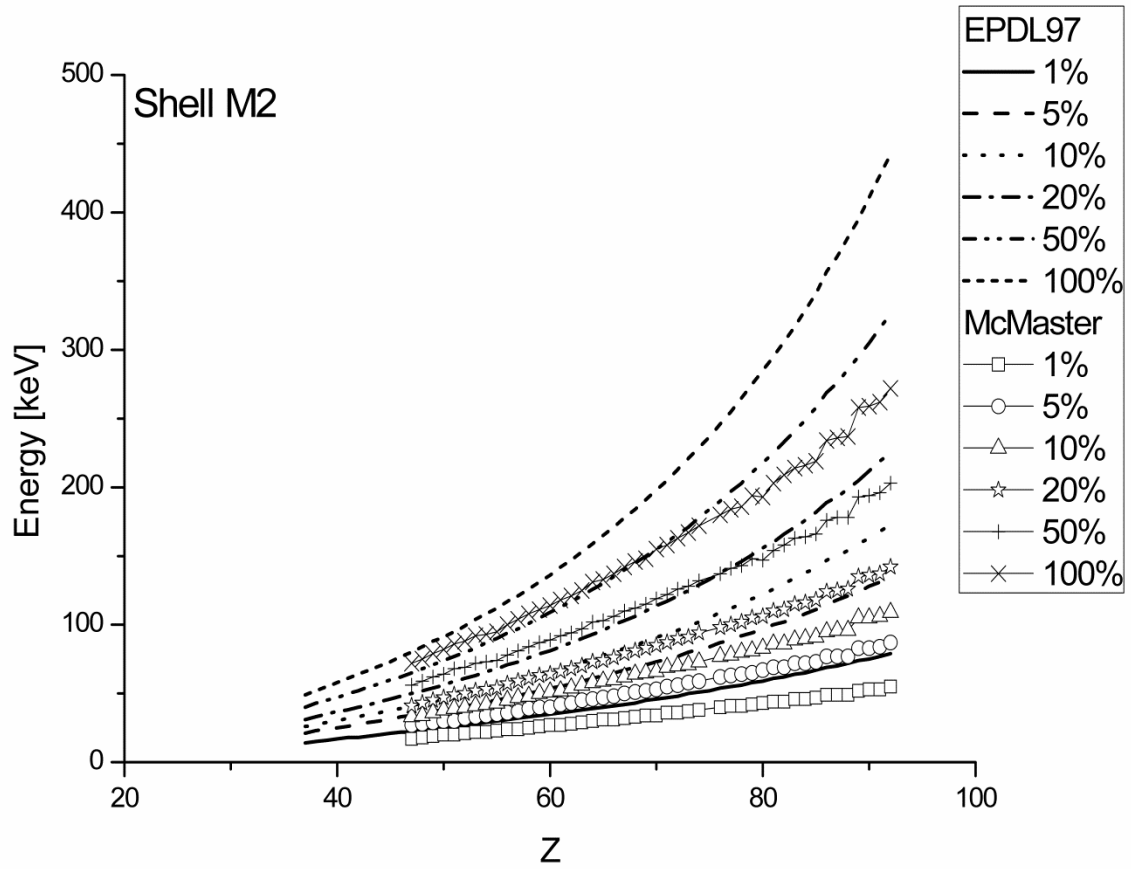


Fig 2.28. Values of the energy in keV, as a function of the atomic number Z, for which  $\frac{\sigma_{M2}}{\tau_{M2}}$  is bigger than 1%, 5%, 10%, 20%, 50% and 100%. This value is computed both using the McMaster and the EPDL97 database.

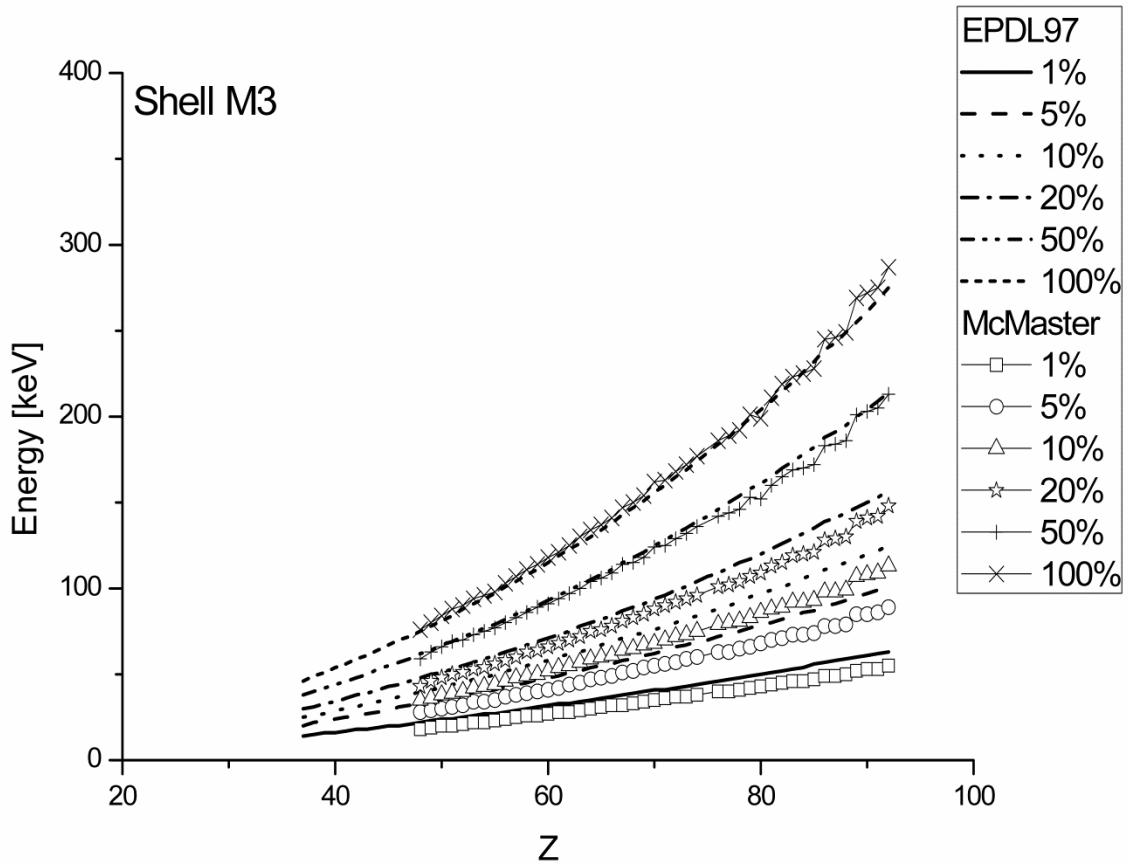


Fig 2.29. Values of the energy in keV, as a function of the atomic number  $Z$ , for which  $\frac{\sigma_{M3}}{\tau_{M3}}$  is bigger than 1%, 5%, 10%, 20%, 50% and 100%. This value is computed both using the McMaster and the EPDL97 database.

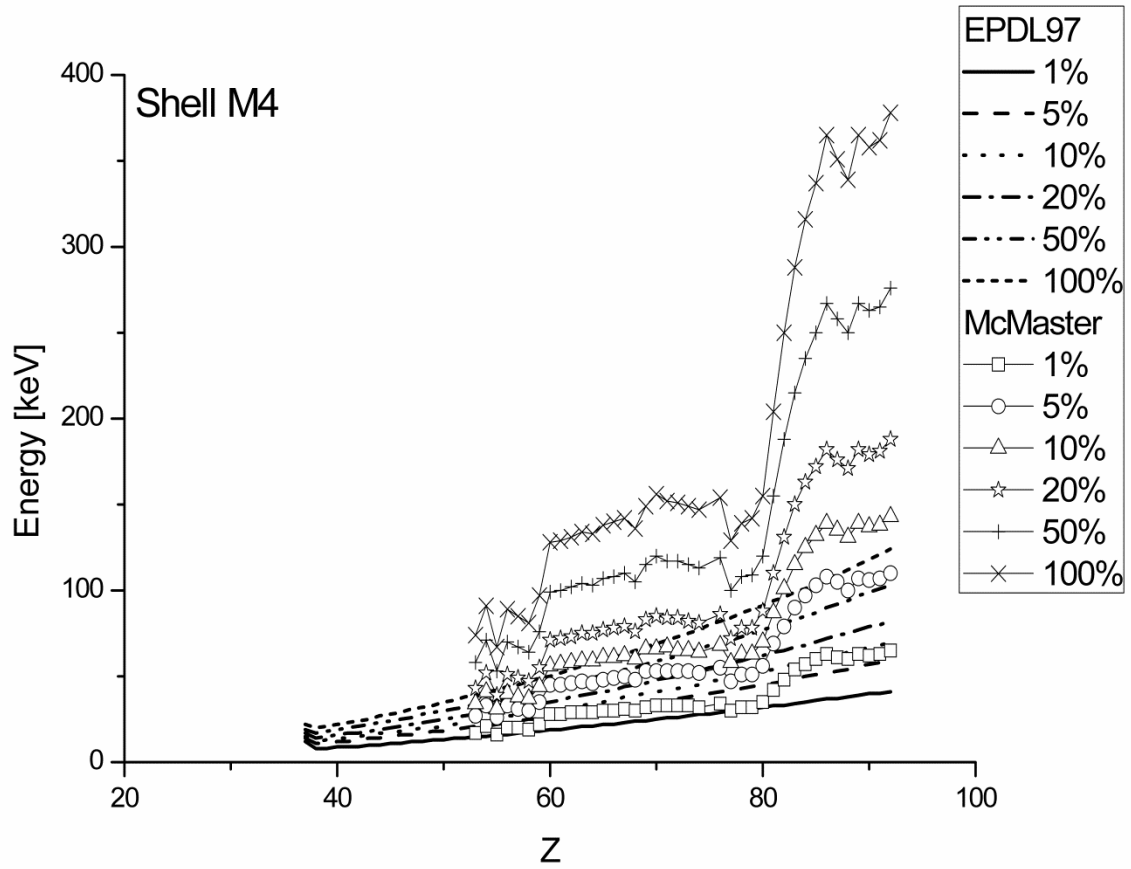


Fig 2.30. Values of the energy in keV, as a function of the atomic number  $Z$ , for which  $\frac{\sigma_{M4}}{\tau_{M4}}$  is bigger than 1%, 5%, 10%, 20%, 50% and 100%. This value is computed both using the McMaster and the EPDL97 database.

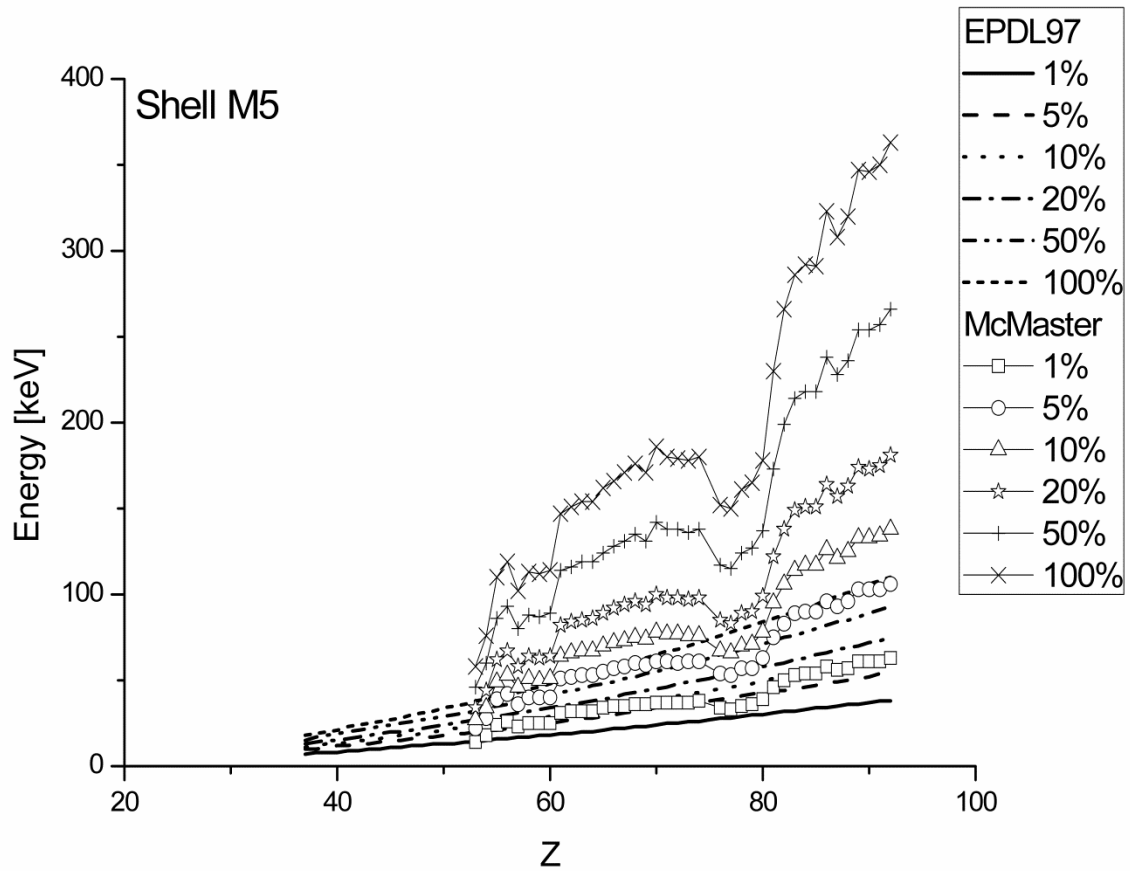


Fig 2.31. Values of the energy in keV, as a function of the atomic number  $Z$ , for which  $\frac{\sigma_{M5}}{\tau_{M5}}$  is bigger than 1%, 5%, 10%, 20%, 50% and 100%. This value is computed both using the McMaster and the EPDL97 database.

From the graphs it can be seen how the gap between the two used data library (McMaster and EPDL97) increase as we move from the K shell to the M shells. In particular, for shells M4 and M5, the behavior of the plot is completely different. These results suggest that also if the McMaster data library gives a good description of the single shell photoelectric cross section for the K shell, it results a too crude approximation to describe the behavior of the photoelectric single shell cross section for the L and the M shells. On the other hand, the EPDL97 data library, by preserving more precise values of the single shell photoelectric cross section for all shells from K to M5, allow the obtainment of a most accurate description of the magnitude of interest.

From the showed EPDL97 distributions it can be than assessed with good precision the energy values at which the Compton interaction becomes the main process of creation of vacancies from K to M5 shells. In particular, in the X-ray energy field (from 1 keV to 150 keV), it can be seen that the XRF contribution from Compton scattering become bigger than the photoelectrical one ( $\sigma_{C_i}/\tau_i \geq 100\%$ ):

- for all elements with  $Z \leq 17$  for the K shell
- for all elements with  $Z \leq 29$  for the L1 shell
- for all elements with  $Z \leq 48$  for the L2 shell
- for all elements with  $Z \leq 52$  for the L3 shell
- for all elements with  $Z \leq 44$  for the M1 shell
- for all elements with  $Z \leq 62$  for the M2 shell
- for all elements with  $Z \leq 68$  for the M3 shell
- for all elements with  $Z \leq 92$  for the M4 shell
- for all elements with  $Z \leq 92$  for the M5 shell

It is then implemented a FORTRAN code that, by using a polynomial fitting method, allows to express the percentage distributions  $E'(Z)$  computed for an arbitrary percentage value  $\sigma_{C_i}/\tau_i$  with a forth degree polynomial equation of the form

$$E'(Z) = a_1 + a_2 \cdot Z + a_3 \cdot Z^2 + a_4 \cdot Z^3 + a_5 \cdot Z^4 \quad (2.39)$$

In tables from Tab 2.3 to Tab 2.11 are shown the polynomial coefficients computed with the developed code that fit the Compton-photoelectric ratio distributions obtained with the EPDL97 database for the  $\sigma_{C_i}/\tau_i$  percentage ratio showed in the figures from Fig. 2.23 to Fig. 2.31 (1%, 5%, 10%, 20%, 50% and 100%).

K Shell					
Percentage	$a_1$	$a_2$	$a_3$	$a_4$	$a_5$
1 %	1.795060	1.229403	0.07052466	-0.000725791	0.000005507833
5 %	20.16897	-0.9357635	0.2426902	-0.00360137	0.00002822135
10 %	20.95964	-1.047857	0.3095737	-0.005040393	0.00004534665
20 %	16.14925	-0.3484109	0.3580223	-0.006412225	0.00006994765
50 %	52.42743	-6.636205	0.8810612	-0.01968788	0.0002193309
100 %	58.99783	-8.481381	1.205097	-0.03063429	0.0003924475

Tab 2.3. Forth degree polynomial fitting coefficients of the Compton-photoelectric ratio distribution evaluated for the K shell. It is used the EPDL97 database to evaluate the single shell photoelectric cross section.

L1 Shell					
Percentage	$a_1$	$a_2$	$a_3$	$a_4$	$a_5$
1 %	-3.125159	0.8759588	0.01284704	-0.000041991	0.0000003797306
5 %	-3.791257	1.125931	0.03255647	-0.000218568	0.000001931976
10 %	-2.321313	1.000399	0.05808626	-0.000552646	0.000004522728
20 %	1.335975	0.6053203	0.1025338	-0.001226354	0.000009948448
50 %	21.39004	-2.008091	0.2682448	-0.004045192	0.00003134196
100 %	17.24509	-1.659722	0.3213939	-0.005344519	0.00004891593

Tab 2.4. Forth degree polynomial fitting coefficients of the Compton-photoelectric ratio distribution evaluated for the L1 shell. It is used the EPDL97 database to evaluate the single shell photoelectric cross section.

L2 Shell					
Percentage	$a_1$	$a_2$	$a_3$	$a_4$	$a_5$
1 %	16.09446	-0.9715079	0.05071526	-0.00052405	0.000002836705
5 %	0.5725386	-0.1584233	0.04948761	-0.000605477	0.000004451143
10 %	45.00625	-3.362916	0.1423031	-0.001698792	0.000009875719
20 %	100.4977	-7.537764	0.2667923	-0.003219314	0.00001771077
50 %	304.3732	-22.90889	0.7089641	-0.008640638	0.00004430710
100 %	745.0976	-56.29289	1.655024	-0.02024592	0.00009931157

Tab 2.5. Forth degree polynomial fitting coefficients of the Compton-photoelectric ratio distribution evaluated for the L2 shell. It is used the EPDL97 database to evaluate the single shell photoelectric cross section.

L3 Shell					
Percentage	$a_1$	$a_2$	$a_3$	$a_4$	$a_5$
1 %	3.675933	-0.00095385	0.022099	-0.00015818	0.000000635605
5 %	-21.33176	1.796506	-0.01387283	0.000275305	-0.00000093697
10 %	-23.01326	1.939690	-0.01216853	0.000284607	-0.00000084089
20 %	-18.63422	1.721269	-0.00108610	0.000200811	-0.00000027273
50 %	-41.21758	3.373439	-0.03304786	0.0006113454	-0.00000137638
100 %	-55.77782	4.416527	-0.04785761	0.0007879209	-0.00000111957

Tab 2.6. Forth degree polynomial fitting coefficients of the Compton-photoelectric ratio distribution evaluated for the L3 shell. It is used the EPDL97 database to evaluate the single shell photoelectric cross section.



M1 Shell					
Percentage	$a_1$	$a_2$	$a_3$	$a_4$	$a_5$
1 %	-29.26884	2.020340	-0.02906628	0.0003484415	-0.00000131728
5 %	0.7121832	0.2211176	0.02514221	-0.000146935	0.0000006300391
10 %	-13.92175	1.131117	0.01409890	-0.000021928	0.0000004172686
20 %	-18.57830	1.433225	0.01968906	-0.000064265	0.000001055045
50 %	14.02994	-1.137344	0.1156350	-0.001182794	0.000007186141
100 %	38.90979	-3.508341	0.2186336	-0.002571468	0.00001594892

Tab 2.7 Forth degree polynomial fitting coefficients of the Compton-photoelectric ratio distribution evaluated for the M1 shell. It is used the EPDL97 database to evaluate the single shell photoelectric cross section.

M2 Shell					
Percentage	$a_1$	$a_2$	$a_3$	$a_4$	$a_5$
1 %	-15.49889	0.8718271	-0.00329748	0.00002935319	0.0000002700289
5 %	-9.652493	0.5365997	0.01032901	-0.0000981310	0.000001169195
10 %	-14.63472	0.8043438	0.009731682	-0.0001121186	0.000001654996
20 %	-11.67456	0.5328313	0.02364888	-0.0002911450	0.000002992499
50 %	24.06540	-2.191088	0.1081441	-0.001314336	0.000008545248
100 %	91.82676	-7.333016	0.2604359	-0.003189133	0.00001820425

Tab 2.8. Forth degree polynomial fitting coefficients of the Compton-photoelectric ratio distribution evaluated for the M2 shell. It is used the EPDL97 database to evaluate the single shell photoelectric cross section.

M3 Shell					
Percentage	$a_1$	$a_2$	$a_3$	$a_4$	$a_5$
1 %	6.688484	-0.4776667	0.02656280	-0.000260096	0.000001094053
5 %	-18.19058	1.185438	-0.00833370	0.0001394313	-0.000000391112
10 %	-14.76519	1.016892	-0.00212328	0.0001065860	-0.000000264532
20 %	-34.38631	2.352179	-0.03112323	0.0004423892	-0.000001484588
50 %	-35.42023	2.424001	-0.02664136	0.0004456391	-0.000001331218
100 %	-9.653263	0.7918672	0.01760996	0.00003291135	0.0000005094626

Tab 2.9. Forth degree polynomial fitting coefficients of the Compton-photoelectric ratio distribution evaluated for the M3 shell. It is used the EPDL97 database to evaluate the single shell photoelectric cross section.

M4 Shell					
Percentage	$a_1$	$a_2$	$a_3$	$a_4$	$a_5$
1 %	86.94472	-5.515189	0.1336785	-0.00129700	0.00000475226
5 %	67.74531	-4.359004	0.1107828	-0.00106915	0.00000401584
10 %	44.86392	-2.817534	0.07406090	-0.00066871	0.00000248605
20 %	33.71884	-2.110166	0.05917522	-0.00050789	0.00000191721
50 %	55.14460	-3.671669	0.1018895	-0.00096363	0.00000382922
100 %	65.69589	-4.344094	0.1195484	-0.00113029	0.00000455582

Tab 2.10. Forth degree polynomial fitting coefficients of the Compton-photoelectric ratio distribution evaluated for the M4 shell. It is used the EPDL97 database to evaluate the single shell photoelectric cross section.

M5 Shell					
Percentage	$a_1$	$a_2$	$a_3$	$a_4$	$a_5$
1 %	-13.84071	0.8773462	-0.01446854	0.0001929043	-0.00000078600
5 %	3.256653	-0.2846259	0.01615379	-0.000110983	0.0000003786407
10 %	-5.996172	0.2644896	0.005651303	-0.000007481	0.00000005052207
20 %	-7.972501	0.3854694	0.004523465	0.00001130705	0.000000003875472
50 %	-27.53050	1.755607	-0.02787032	0.0003792688	-0.000001404330
100 %	-18.36574	1.093991	-0.00978042	0.0002109543	-0.0000007481635

Tab 2.11. Forth degree polynomial fitting coefficients of the Compton-photoelectric ratio distribution evaluated for the M5 shell. It is used the EPDL97 database to evaluate the single shell photoelectric cross section.

Some examples of the distributions obtained with the polynomial fitting formula in Eq. 2.39 by using the fitting coefficients reported from Tab 2.3 to Tab 2.11 are shown in Fig. 2.32, Fig 2.33 and Fig 2.34. The validity of the fitted distribution showed in the following figures is limited only in the Z range where, for the considered shell, values of the Compton-photoelectric ratio exist.

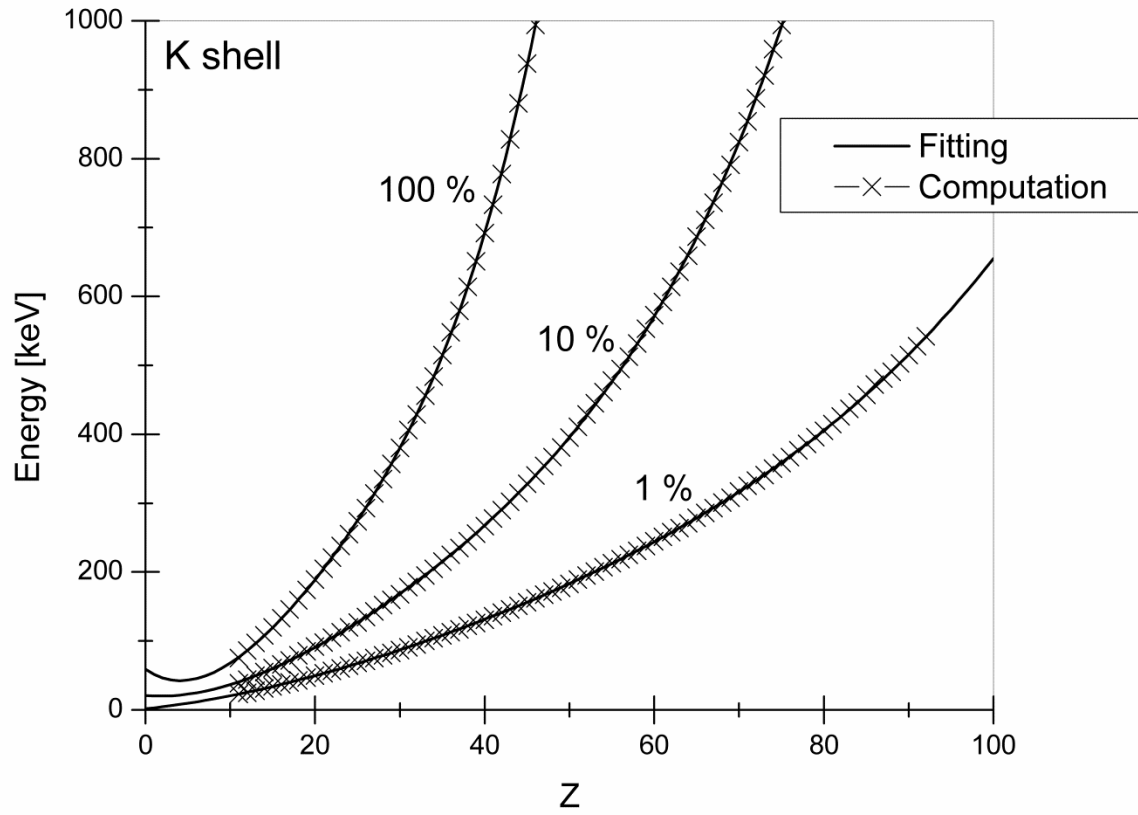


Fig 2.32. Comparison between the computed distributions and the fitting distribution obtained with Eq. 2.39, for the K shell and for 1%, 10%, and 100% compton-photoelectric ratio.

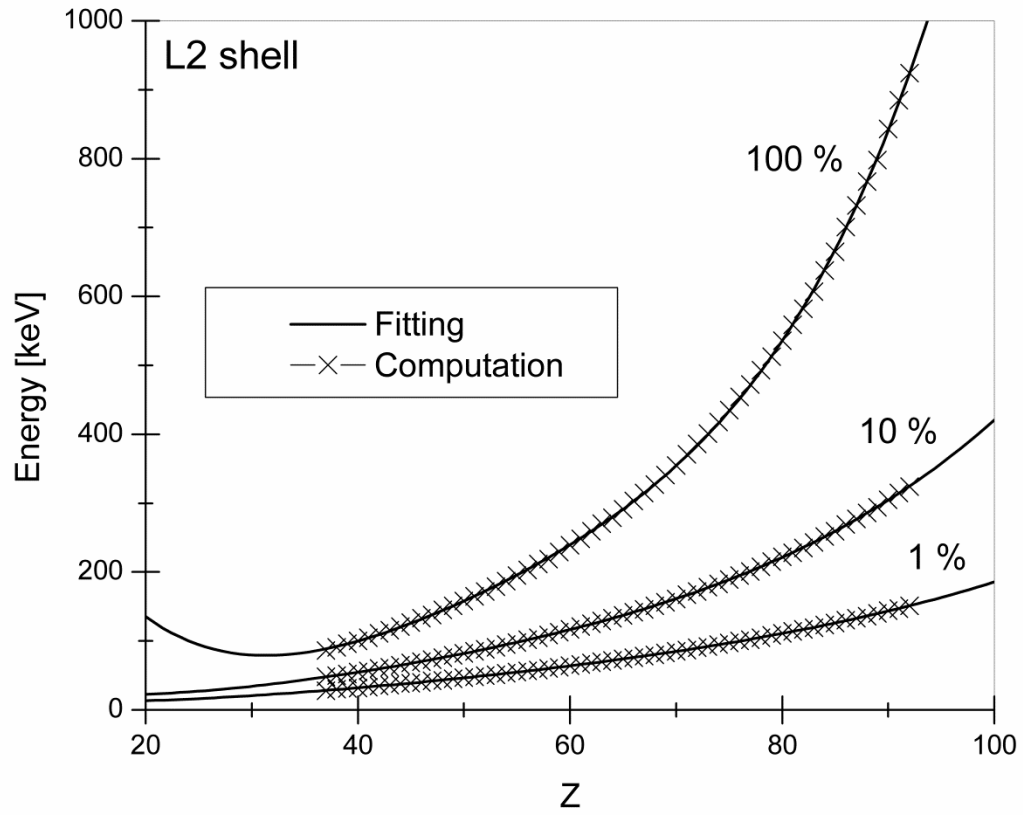


Fig 2.33. Comparison between the computed distributions and the fitting distribution obtained with Eq. 2.39, for the L2 shell and for 1%, 10%, and 100% compton-photoelectric ratio.

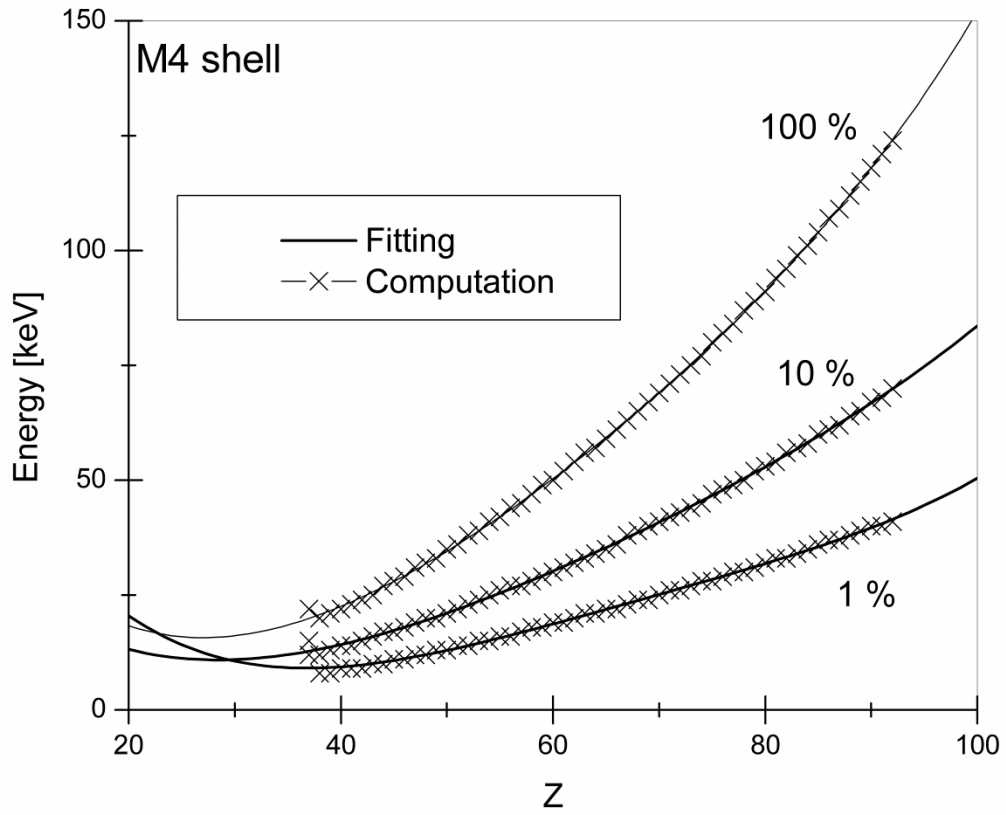


Fig 2.33. Comparison between the computed distributions and the fitting distribution obtained with Eq. 2.39, for the L2 shell and for 1%, 10%, and 100% Compton-photoelectric ratio.

## 2.7 XRF from Compton ionization kernel refinement

As shows in the previous sections, the Compton scattering is an important ionization process which in some cases gives rise to a non-negligible atomic relaxation contribution. The contribution due to Compton scattering can be added directly into the photoelectric cross section showed in Eq. 2.29 as a corrective term  $f_i^C$  for each considered line  $i$  defined as

$$f_i^C = \left(1 + \frac{\sigma_{C_i}}{\tau_i}\right) \quad (2.40)$$

obtaining the new photoelectric effect kernel

$$k_P(\vec{\omega}', E', \vec{\omega}, E) = \frac{1}{4\pi} \sum_{i=1}^{n\_lines} Q_{E_i}(E') f_i^C \delta(E - E_i) [1 - \cup(E_{e_i} - E')] \quad (2.41)$$

This new kernel expression allows the addition to the Boltzmann model of atomic relaxation contribution due to Compton ionization process for each shell from K to M5.

An evaluation of the XRF corrective term  $f_i^C$  in function of the photon energy  $E'$ , for a generic shell  $i$  of a generic element  $Z$  can be done in first approximation by applying a linear interpolation method between the Compton-photoelectric ratio fitted distributions showed in the previous section. However this interpolation method result too crude and some attempts to find a parametric function capable to describe the energy dependences of the XRF correction from Compton ionization need to be investigate in the future.





## Chapter 3

# Electrons' radiative contribution in X-ray transport processes

In the previous chapter it is shown how the radiative contribution of an X-ray transport process can be studied through the use of the Boltzmann model. In this model, the photons can interact with atoms through three different mechanisms: the Rayleigh scattering, the Compton scattering and the photoelectric effect. By these processes, however, not only photons are produced: the Compton scattering and the photoelectric effect, in fact, are ionizing interactions which cause the ejection of a secondary electron from the interacting atom. The produced secondary electrons interact along its path through different collision mechanism, some of which generate photons that contributes to the radiation field. A full description of the radiative interactions involved in an X-ray transport process is shown in Fig. 3.1.

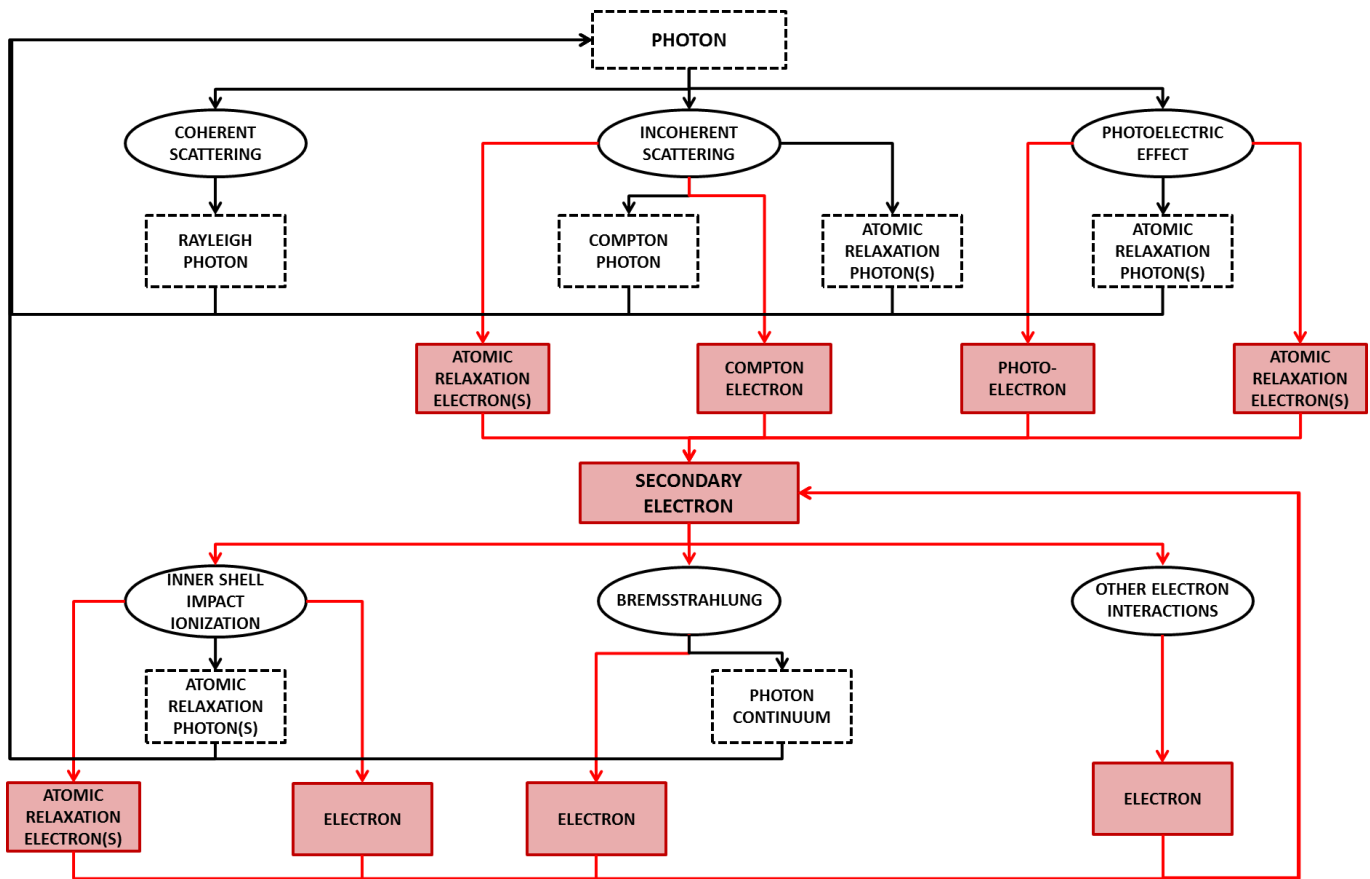


Fig. 3.1. Main photon and electron interactions in the energy range 1-150 keV. Secondary electrons feedback new photons into the photon interactions cycle through conversion mechanisms like bremsstrahlung and inner-shell impact ionization. Photons are represented with dash boxes and black lines, electrons with solid red boxes and lines. Other electron interaction not mentioned explicitly here like elastic and inelastic electrons scattering, etc. are packed in the box “Other electron interactions”. Auger electrons and Coster-Kronig transitions are packed in the box “Atomic relaxation electron”.

As it can be seen from Fig 3.1 secondary electrons produce photons through two main interaction processes: the bremsstrahlung (which produces a continuous photon energy spectrum) and the inner shell impact ionization (ISII) (an inelastic collision which ionizes the interacting atom causing a vacancy in an atomic shell that is filled through a relaxation process). These electrons’ radiative contributions are completely neglected in the Boltzmann photon transport model used by now and a most accurate description of the radiation field in X-ray spectrometry requires the modeling of the coupled photon-electron transport equation model.

The continuous behavior of electron interactions makes it difficult to treat the multiple scattering in the transport equation for electrons. Because of this difficulty, it is preferred the use of the Monte Carlo simulation together with special numerical approximations to describe the multiple scattering of electrons. This technique however results in most of cases extremely time consuming. An alternative approach to this problem consists in computing externally corrective kernel terms to the photon Boltzmann transport model able to describe the contribution of secondary electrons to the radiation field. By this approach, the Boltzmann equation showed in Chapter 2 can be rewritten as:

$$\begin{aligned}
 & \eta \frac{\partial}{\partial z} f(z, \vec{\omega}, E) = -\mu(E) f(z, \vec{\omega}, E) \\
 & + \sum_i^{\text{all photon interactions}} \int_0^\infty \left( \int_{4\pi} \cup(z) k_i^{p \rightarrow p}(\vec{\omega}', E', \vec{\omega}, E) f(z, \vec{\omega}', E') d\omega' \right) dE' \\
 & + \sum_j^{\text{all coupling terms}} \int_0^\infty \left( \int_{4\pi} \cup(z) k_j^{e \rightarrow p}(\vec{\omega}', E', \vec{\omega}, E) f(z, \vec{\omega}', E') d\omega' \right) dE' \\
 & \quad \quad \quad + S(z, \vec{\omega}, E)
 \end{aligned} \tag{3.1}$$

where the superscripts  $e$  and  $p$  stand for electron and photon respectively,  $f$  is the particle flux,  $\vec{\omega}'$  and  $\vec{\omega}$  are the unit vectors defining the propagation direction of the particles respectively before and after a generic interaction,  $E'$  and  $E$  are the energy before and after a generic interaction,  $\eta$  denotes the directional cosine  $\omega_z$ ,  $d\omega' = d\eta' d\phi'$  is the differential of the solid angle in the direction of the unitary vector  $\vec{\omega}'$ ,  $\mu(E)$  is the total attenuation coefficient,  $\cup(z)$  the unitary step Heaviside function,  $k^{p \rightarrow p}(\vec{\omega}', E', \vec{\omega}, E)$  is the single process photon to photon interaction kernel,  $k^{e \rightarrow p}(\vec{\omega}', E', \vec{\omega}, E)$  is the single process electron to photon interaction kernel, and  $S(z, \vec{\omega}, E)$  is an external source of photons. The coupling terms represent the change with respect to the previous transport equation.

This method was recently introduced by Fernandez et al. [Fernandez, 2013], [Fernandez, 2014-2] to study the correction on the intensity of the characteristic lines due to ISII. In the third part of this thesis, a similar strategy is applied to study the bremsstrahlung radiation produced by secondary electrons. This effect is fundamental to properly characterize the background of the recorded spectrum which otherwise remains unexplained in entire energy region. This is particularly evident in the simulation of synchrotron experiments with monochromatic excitation using photon codes [Fernandez, 2009].

In this work the ad-hoc code KERNEL [Fernandez, 2013], [Fernandez, 2014-2] is adapted to evaluate the bremsstrahlung radiative contribution of secondary electrons. KERNEL simulates the sequence of interactions of particles generated from a forced first collision of a monochromatic photon source at the origin of coordinates in an infinite medium by using the Monte Carlo coupled photon-electron transport code PENELOPE [Salvat, 2011]. To give a complete description of the magnitudes of interest, the bremsstrahlung radiative contribution is evaluated as a function of angle, space coordinates and energy in the range 1-150 keV, for all elements  $Z=1-92$ . It is shown that the resulting distributions can be well approximated with an isotropic point source contribution. The energy distributions of bremsstrahlung quanta is calculated for selected photon source energies and stored in a data base. A 2D interpolation scheme on the data library is developed to compute the single element contribution at arbitrary energies. Finally a new bremsstrahlung corrective kernel, which allows the introduction of the bremsstrahlung contribution in the modified photon transport Boltzmann equation through the use of the data library, is introduced. This new kernel can be easily used in photon transport codes (deterministic or Monte Carlo) with a minimal increase in complexity. The use of the developed kernel is illustrated with some examples, showing the tremendous improvement in the computational speed compared to the solution of the coupled transport problem.

In what follows, starting from a brief description of the electron interaction engine used in the Monte Carlo code PENELOPE, the results obtained in this work on the radiative characterization of the bremsstrahlung due to secondary electron are shown together with the results obtained by Fernandez et al. [Fernandez, 2013], [Fernandez, 2014-2] for the ISII contribution.

## 3.1 The Monte Carlo code PENELOPE

PENELOPE [Salvat, 2011] is a Monte Carlo algorithm and computer code developed at the Facultat de Física (ECM) of the Universitat de Barcelona (UB) that simulates coupled electron-photon transport in arbitrary geometries and in a wide energy range, from a few hundred of eV to about 1 GeV. PENELOPE simulates electron-photon showers in infinite (unbounded) or finite media of various compositions. As a Monte Carlo method, the simulation of a given experimental arrangement consists of the numerical generation of random histories. In the simulation, the history (track) of a particle is viewed as a random sequence of free flights that end with an interaction event where the particle changes its direction of movement, loses energy and, occasionally, produces secondary particles. To simulate these histories is used an interaction model, i.e., a set of differential cross sections (DCS) for the relevant interaction mechanisms. The DCSs determine the probability distribution functions (PDF) of the following random variables that characterize a track:

1. Free path between successive interaction events.
2. Type of interaction taking place
3. Energy loss and angular deflection in a particular event (and initial state of emitted secondary particles, if any).

Once these PDFs are known, random histories can be generated by using appropriate sampling methods. If the number of generated histories is large enough, quantitative information on the transport process may be obtained by simply averaging over the simulated histories.

The PENELOPE simulation algorithm is based on a scattering model that combines numerical databases with analytical cross section models for the different interaction mechanisms. Photon transport is followed by using a highly detailed simulation method. The simulation of electrons is performed by means of a mixed procedure, which combines detailed simulation of the so-called “hard” events (interactions with scattering angle or energy loss greater than a preselected value), with condensed simulation of “soft” interactions (interactions with scattering angle or energy loss less than the corresponding cut-off). Secondary particles are produced in direct interactions (hard inelastic collisions, hard bremsstrahlung emission, positron annihilation, photoelectric absorption, Compton scattering and pair production) and as fluorescent radiation (characteristic X-rays and Auger electrons). Secondary particles emitted with initial energy larger than an absorption energy value defined by the user are stored and simulated after completion of each primary track.

The PENELOPE Monte Carlo method yields the same information as the solution of the coupled Boltzmann transport equation, with a similar interaction model, but is easier to implement. In particular, the simulation of radiation transport in complex geometry is straightforward, while even the simplest finite geometries are very difficult to be dealt with by the transport equation. This advantage of the Monte Carlo transport codes is based on the assumption that particle transport can be modeled as a Markov process, *i.e.*, future values of a random variable (interaction event) are statistically determined by present events and depend only on the event immediately preceding. Owing to the Markovian character of the transport, it is possible to stop the generation of a particle history at an arbitrary state and resume the simulation from this state without introducing any bias in the results. The main drawback of the Monte Carlo method lies in its random nature: all the results are affected by statistical uncertainties which can be reduced at the expense of increasing the sampled population and, hence, the computation time.

In this work the Monte Carlo code PENELOPE is used to collect the secondary electrons' radiative contribution. PENELOPE simulates all the possible interactions of electrons in the considered medium (Bremsstrahlung, elastic scattering, inelastic scattering, ISII) by using atomic DCSs defined either as analytical functions or by means of numerical tables, or as a combination of both. In what follows, the main DCSs used by PENELOPE to simulate the two electronic interactions of interest (bremsstrahlung and ISII) are described. More details can be found on the PENELOPE manual [Salvat, 2011].

### 3.1.1 Inner shell impact ionization process

The inner shell impact ionization is an inelastic collision process between a free electron and another one located in an inner shell of the interacting atom. In this process the inner shell electron is expelled from the atom generating a vacancy subsequently filled by an atomic relaxation process. The PENELOPE model for the simulation of inner-shell ionization and relaxation take into account for the following features of the process:

1. Space distribution of inner-shell ionizations along the projectile's track.
2. Relative probabilities of ionizing various atomic electron shells.
3. Energies and emission probabilities of electrons and X-rays released through the de-excitation cascade of the ionized atom.

In previous versions of PENELOPE, ISII was simulated using cross sections obtained from the atomic generalized oscillator strength (GOS) model [Mayol, 1990], *i.e.*, from an approximate formulation of the plane-wave (first) Born approximation (PWBA). However, the cross section for ionization of a bound shell decreases rapidly with the shell ionization energy  $U_i$  (because energy transfers less than  $U_i$ , which would promote the target electron to occupied states, are forbidden). As a consequence, collisions occur preferentially with electrons in the conduction band and in outer bound shells. ISII by electron/positron impact is a relatively unlikely process, and the GOS model, used for electron inelastic interactions, is too crude to

provide an accurate description of it. A more elaborate theoretical description of total ionization cross sections is obtained from the relativistic distorted-wave Born approximation (DWBA), which consistently accounts for the effects of both distortion and exchange [Bote, 2008].

In the present version of PENELOPE [Salvat, 2011], an extensive numerical database of ionization cross sections has been calculated for K, L and M shells of all the elements from hydrogen ( $Z = 1$ ) to einsteinium ( $Z = 99$ ), for projectiles with kinetic energies from threshold up to 1 GeV. The theoretical model adopted in these calculations combines the DWBA and the PWBA, as described by Bote and Salvat [Bote, 2008]. The DWBA is used to calculate the ionization cross section for projectiles with energies from  $\sim U_i$  up to  $16 U_i$ . For higher energies, the cross section is obtained by multiplying the PWBA cross section by an empirical energy-dependent scaling factor, which tends to unity at high energies where the PWBA is expected to be reliable. This calculation scheme accounts for differences between the cross sections for ionization by electrons and positrons. The cross section for ionization of the  $i$ -th shell of a given element by impact of electrons with kinetic energy  $E'$  will be denoted by  $\sigma_{si,i}(E')$ . The PENELOPE numerical database consists of 198 files with tables of the cross sections for ionization of K, L and M shells of the elements ( $Z= 1-99$ ) by electron impact. The grid of energies where  $\sigma_{si,i}(E')$  is tabulated varies with the element, because it has a higher density of points above each ionization threshold to allow accurate linear log-log interpolation. The atomic cross section for inner-shell ionization is obtained as the sum over all the inner shell of the atom  $i$  of the single shell cross section  $\sigma_{si,i}(E')$ .

The atomic relaxation processes subsequent to an ISII interaction is simulated in PENELOPE for vacancies produced in K, L, and M shells. The relaxation of these vacancies is followed until the K, L and M shells are filled up, i.e., until the vacancies have migrated to N and outer shells. Vacancies in these outer shells originate much less energetic secondary radiation, whose main effect is to spread out the excitation energy of the ion within the surrounding material. In the simulation are considered only characteristic X-rays and Auger electrons emitted in the first stages of the relaxation process. These secondary radiations are assumed to be emitted isotropically from the excited atom. To designate all the possible transitions in PENELOPE are used the following notations:

- Radiative transition: S0-S1 (an electron from the S1 shell fills the vacancy in the S0 shell, leaving a hole in the S1 shell).
- Non radiative transition: S0-S1-S2 (an electron from the S1 shell fills the vacancy in the S0 shell, and the released energy is taken away by an electron in the S2 shell; this process leaves two vacancies in the S1 and S2 shells).

The information furnished to PENELOPE for each element consists of a table of possible transitions, transition probabilities and energies of the emitted X-rays or electrons for ionized atoms with a single vacancy in the K shell or in an L or M subshell. The transition probabilities are extracted from the LLNL Evaluated Atomic Data Library [Perkins, 1991]. The energies of x rays emitted in radiative transitions resulting from single vacancies in the K and L shells were taken from the recent compilation by Deslattes et al. [Deslattes, 2003]. X-ray energies for

transitions of vacancies in M shells were taken from Bearden's [Bearden, 1967] review and reevaluation of experimental X-ray wavelengths. In the case of radiative transitions S0-S1 not included in Bearden's tabulation, the energy of the x ray is approximated as

$$E_p = U'_{s_0} - U'_{s_1} \quad (3.2)$$

where  $U'_{s_i}$  is the ionization energy of an electron in the shell  $S_i$  of the neutral atom, which was taken from the LLNL Evaluated Atomic Data Library [Perkins, 1991]. The ionization energies in this library are the negatives of the eigenvalues of the Dirac-Hartree-Fock-Slater self-consistent equations for neutral atoms in their ground states. For tightly bound shells, with  $U'_{s_i} \geq 200\text{eV}$ , the theoretical values  $U'_{s_i}$  agree closely with Carlson's [Carlson, 1975] recommended shell ionization energies [Salvat, 2009]. The energy of the electron emitted in the non-radiative transition S0-S1-S2 is set equal to

$$E_e = U'_{s_0} - U'_{s_1} - U'_{s_2} \quad (3.3)$$

The transition that fills the initial vacancy is randomly selected according to the adopted transition probabilities, by using Walker's aliasing sampling method [Salvat, 2011]. This transition leaves the ion with one or two vacancies. If the energy of the emitted characteristic X-ray or Auger electron is larger than the corresponding absorption energy, the state variables of the particle are stored in a secondary stack (which contains the initial states of all particles produced during the current shower that have not yet been simulated). The generation of the cascade continues by repeating the process for each remaining vacancy. It ends either when the K, L and M subshells have been filled up or when there is not enough energy to produce effective fluorescence radiation (with energy larger than the absorption energy).



### 3.1.2 Bremsstrahlung process

As a result of the acceleration caused by the electrostatic field of atoms, swift electrons (or positrons) emit bremsstrahlung (braking radiation). In each bremsstrahlung event, an electron with kinetic energy  $E_e$  generates a photon of energy  $E$ , which takes values in the interval from 0 to  $E_e$ . The process is described by an atomic DCS, differential in the energy loss  $E$ , the final direction of the projectile and the direction of the emitted photon [Koch, 1959], [Tsai, 1974]. A simple description of the bremsstrahlung DCS is given by the Bethe-Heitler formula with screening, which is derived within the Born approximation [Bethe, 1934], [Tsai, 1974]. This formula predicts that, for a given value of  $Z$ , the quantity  $E(d\sigma_{br}/dE)$  varies smoothly with  $E$  and  $E_e$ . Therefore, the DCS for bremsstrahlung emission by electrons is usually expressed in the form

$$\frac{d\sigma_{br}}{dE} = \frac{Z^2}{\beta^2} \frac{1}{E} \chi(Z, E_e, \kappa) \quad (3.4)$$

where  $\kappa = E/E_e$  is the reduced photon energy which takes values between 0 and 1, and  $\beta = v/c$  is the velocity of the electron in units of the speed of light  $c$ . The quantity

$$\chi(Z, E_e, \kappa) = E \frac{d\sigma_{br}}{dE} \frac{\beta^2}{Z^2} \quad (3.5)$$

is known as the scaled bremsstrahlung DCS and, for a given element  $Z$ , it varies smoothly with  $E_e$  and  $\kappa$ . Seltzer and Berger [Seltzer, 1985], [Seltzer, 1986] produced extensive tables of the scaled DCS for elements with  $Z$  from 1 to 92 and for electron energies between 1 keV and 10 GeV. They calculated the DCS for the interaction with the field of the nucleus shielded by the electron cloud, and for that with the field of atomic electrons. The electron-nucleus bremsstrahlung DCS was calculated, for emission in screened atomic fields and energies below 2 MeV, by combining analytical theories for high energy with the results of the partial wave calculations by Pratt et al. [Pratt, 1977]. The scaled DCS for electron-electron bremsstrahlung was obtained from the theory of Haug [Haug, 1975] in combination with a screening correction involving Hartree-Fock incoherent scattering functions.

The PENELOPE database of scaled bremsstrahlung differential cross sections consists of 99 files, one for each element from hydrogen to einsteinium, which were generated from the original database of Seltzer and Berger. The file of the element  $Z$  contains the values of  $\chi(Z, E_{e,i}, \kappa_i)$  for a set of  $i$ -th electron kinetic energies  $E_{e,i}$ , which covers the range from 1 keV to 10 GeV. The grid of values is built to allow natural cubic spline interpolation in  $\ln(E_e)$ . For each energy  $E_{e,i}$  in this grid, the table contains the values of the scaled DCS for a given set of 32 reduced photon energies  $\kappa_j$  (the same for all elements), which span the interval  $[0, 1]$ . The spacing of the  $\kappa$ -grid is dense enough to allow linear interpolation of  $\chi(Z, E_e, \kappa)$  in  $\kappa$ .

The direction of the emitted bremsstrahlung photon is defined by the polar angle  $\theta$  and the azimuthal angle  $\phi$ . For isotropic media, with randomly oriented atoms or molecules, the bremsstrahlung DCS is independent of  $\phi$  and can be expressed as

$$\frac{d^2\sigma_{br}}{dEd\cos(\theta)} = \frac{d\sigma_{br}}{dE} p_{br}(Z, E_e, \kappa; \cos(\theta)) \quad (3.6)$$

where  $p_{br}(Z, E_e, \kappa; \cos(\theta))$  is the PDF of  $\cos(\theta)$ , called shape function. Numerical values of the shape function were calculated by partial-wave methods and have been published by Kissel et al. [Kissel, 1983] for the following benchmark cases:  $Z= 2, 8, 13, 47, 79, 92$ ;  $E_e = 1, 5, 10, 50, 100, 500$  keV and  $\kappa = 0, 0.6, 0.8, 0.95$ . These authors also gave a parameterization of the shape function in terms of Legendre polynomials. Unfortunately, their analytical form is not suited for random sampling of the photon direction. In PENELOPE, a different parameterization is used, by means of the semi empirical analytical formula derived by Kirkpatrick and Wiedmann [Kirkpatrick, 1945] (and subsequently modified by Statham [Statham, 1976]) modified by introducing two adjustable parameters to reproduce the benchmark shape functions tabulated by [Kissel, 1983] also allowing the random sampling of  $\cos(\theta)$  in a simple way [Salvat, 2011].

## 3.2 The program KERNEL

The PENELOPE code system is a FORTRAN 77 subroutine package, which performs simulation of electron-photon showers. Being a subroutine package, PENELOPE cannot operate by itself but needs the writing of a main program to simulate the desired problem. This main program has to read the parameters introduced through the input file, control the evolution of the generated tracks and keep score of relevant quantities. PENELOPE has been devised to do the largest part of the simulation work. This property allows the user to write its own simulation program, with arbitrary geometry and scoring, without previous knowledge of the intricate theoretical aspects of scattering and transport theories.

In the present work, the ad-hoc main program KERNEL has been developed to simulate the sequence of interactions of particles generated from a forced collision of a monochromatic photon source at the origin of coordinates in an infinite medium using the PENELOPE engine. The physics of the interactions is described using the PENELOPE subroutine library. The simulated process is sketched by the flow diagram in Fig. 3.2, and is summarized by the following points:

- Point 1.** A photon with energy  $E'$ , situated in an infinite medium, comes along the z axis and hits an atom in the origin of the reference frame. In the energy range of interest 1-150 keV, photons can interact through three different processes: photoelectric effect, coherent (Rayleigh) scattering, incoherent (Compton) scattering. The first and the third interactions involve the production of secondary electrons. If their energy exceeds a user defined absorption limit, these particles are stored in the secondary stack.
- Point 2.** After the interaction, the secondary stack is immediately checked in order to verify the presence of particles. If it is found empty, the photon suffered a Rayleigh interaction and the code goes back to point 1, starting a new shower. Otherwise, it proceeds to point 3.
- Point 3.** The secondary stack can contain electrons, or photons. The program starts to simulate the slowing down process for electrons until their energy falls down the absorption threshold  $E_{ABS}$ . The transport of secondary photons is ignored. Charged particle interactions involve the production of other charged particles and photons: the first ones are stored in the secondary stack; the photon properties are scored in order to obtain angular, energy and spatial distributions. These distributions are tallied for bremsstrahlung emission, ISII.
- Point 4.** The simulation of the shower keeps going until the secondary stack is empty, and all the charged particles stored in it have completed their 'lives'. At this point, the shower is completed and KERNEL starts the generation of a new one (point 1).

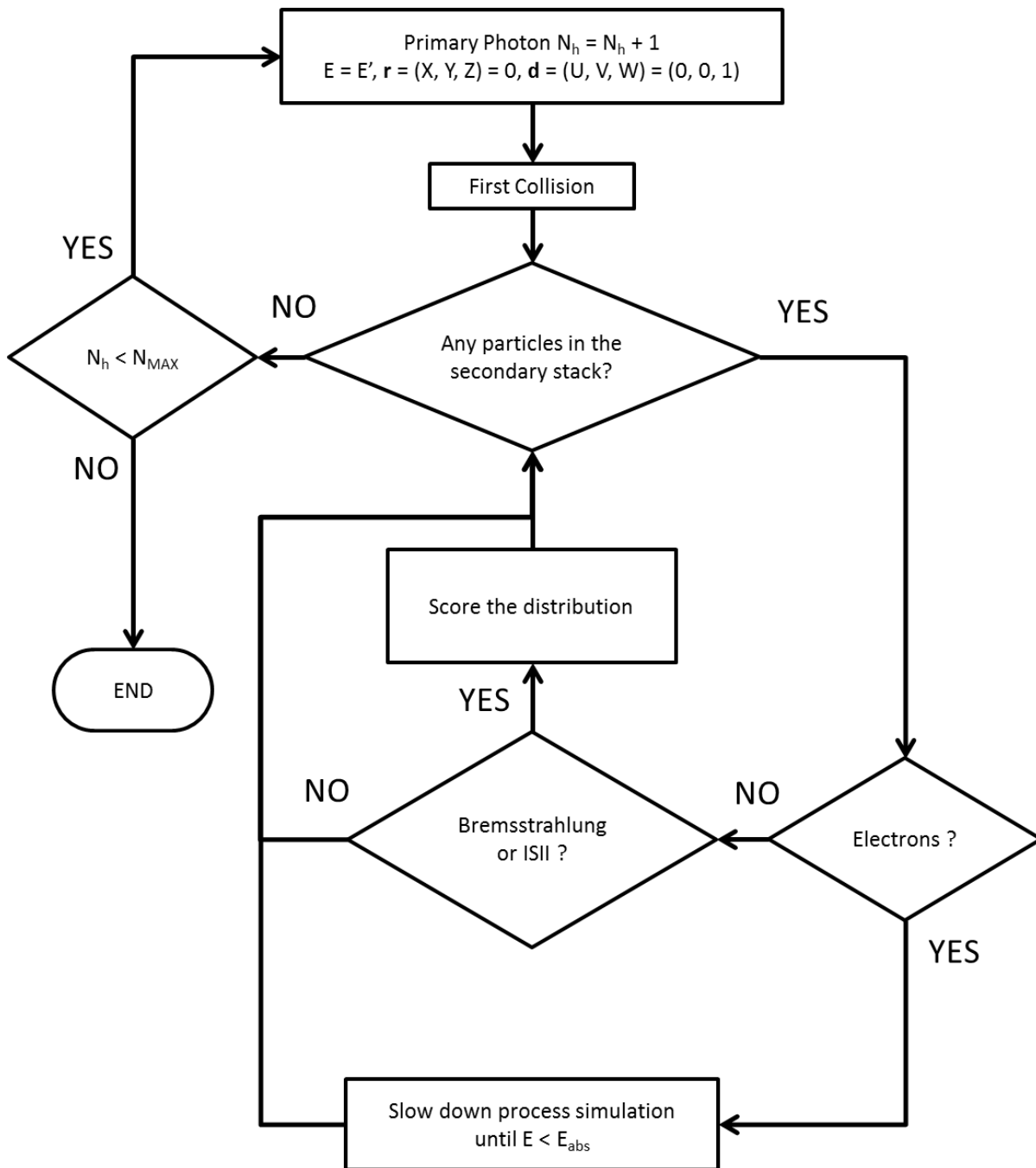


Fig. 3.2 Flow diagram of the code KERNEL.

### 3.2.1 KERNEL input files

An example of the structure of the KERNEL input file is depicted below in Fig 3.3.

```

TITLE Al .
      >>>>>>> Source definition.
SENERG 0.1500E+04          [Initial energy (monoenergetic)]
      .
      >>>>>>> Material data and simulation parameters.
MFNAME Al.mat              [Material file, up to 20 chars]
MSIMPA 200 200 200 .01 .01 200 200      [EABS(1:3),C1,C2,WCC,WCR]
DSMAX 1.0e20                [Maximum step length]
      .
      >>>>>>> Interaction forcing.
IFORCE 1 1 4 -8.0 0.01 10          [KB,KPAR,ICOL,FORCER,WLOW,WHIG]
IFORCE 1 1 5 -100 0.01 10         [KB,KPAR,ICOL,FORCER,WLOW,WHIG]
      .
      >>>>>>> Counter array dimensions and pdf ranges.
NBE 000.0 150000.0 300          [Energy window and no. of bins]
NBANGL 200                    [Nos. of bins for cos(THETA)]
NBZ 200                        [No. of bins for the Z-coordinate]
NBR 200                        [No. of radial bins]
      .
      >>>>>>> Job properties.
RESUME dump.dmp              [Resume from this dump file, 20 chars]
DUMPTO dump.dmp              [Generate this dump file, 20 chars]
DUMPP 600                     [Dumping period, in sec]
      .
RSEED 52983 98352            [Seeds of the random-number generator]
NSIMSH 1E6                    [Desired number of simulated showers]
TIME 1e19                     [Allotted simulation time, in sec]
      .
END                            [Ends the reading of input data]

```

Fig. 3.3. Example of the KERNEL input file. The input file shown is related to the simulation for an aluminum material target with energy source of 1.5 keV.

The following listing describes the function of each of the input keywords:

- **TITLE:** In this section is defined the title of the job. In our case the title is set equal to the chemical name of the element considered in the simulation (in the example shown in Fig. 3.3 is Al for aluminum). The **TITLE** string is used to mark the dump files created by PENELOPE. This dump file collect all the intermediate results an parameter of the simulation and allows to stop the computation process in an intermediate stage and to resume it in a later computation.

>>>>>>> Source definition

- **SENERG:** In this section is defined the value of the monochromatic photon source energy expressed in eV (in the example shown in Fig. 3.3 is 1500 eV).
- **Other source parameter:** there are other source parameters not defined in the input but introduced directly in the main program KERNEL. These parameter are:
  - **SKPAR:** This parameter defines the kind of simulated source particles **KPAR** (1 for electrons, 2 for photons, 3 for positrons). As we are simulating a photon source, in our case the **KPAR** value for the first particle is the same for all the computations (**KPAR** = 2).
  - **SGPOL:** This parameter defines the polarization state of the photon source by using the three Stokes parameters (**SP1**, **SP2** and **SP3**) [Salvat, 2011]. In the simulation it can be considered the effects due to the polarization state of the particles by set the parameter **IPOL**=1. In our case, we are not considering the photon's polarization state in the simulation and it is considered **IPOL** = 0 by default. By this setting all the three Stokes parameter are set equal to zero (**SP1**=0, **SP2**=0 and **SP3**=0) for all the simulated particles.
  - **SPOSIT:** This parameter expresses the position of the primary energy through the definition of the three Cartesian coordinates (**SX0**, **SY0** and **SZ0**). As in our simulation we are considering a point source centered in the origin of coordinates in an infinite medium, these parameter are set always equal to 0 (**SX0**=0, **SY0**=0 and **SZ0**=0).

>>>>>>> Material data and simulation parameters

- **MFNAME:** In this section is defined the material file name of the PENELOPE input material data file generated by running the PENELOPE's program MATERIAL. This file includes tables of physical properties, interaction cross sections and relaxation data of the considered material. Additional information on the program MATERIAL and on the material file structure can be found in the PENELOPE manual [Salvat, 2011].
- **MSIMPA:** In this section are defined the values of the simulation parameters for the considered material. The defined values are:
  - **EABS(KPAR,MAT):** This parameter is a **KPAR**×**MAT** matrix in which are defined the absorption threshold energy values  $E_{ABS}$  of each the simulated particle **KPAR** in each considered material **MAT**. As we are considering a homogenous infinite

material composed by a single element, in our computation **MAT** is set equal to one (**MAT=1**). The absorption threshold energy value is the same for all the considered particles **KPAR** and is set equal to 200 eV for computation with source energies lower equal than 5 keV, and equal to 500 eV for computation with source energies greater than 5 keV.

- **c1**: This parameter defines the average angular deflection produced by multiple elastic scattering of electrons along a path length equal to the mean free path between consecutive hard elastic events (set by default equal to 0.01).
- **c2**: This parameter is the maximum average fractional energy loss, between consecutive electrons hard elastic events (set by default equal to 0.01).
- **WCC**: This parameter is the cutoff energy loss (in eV) for hard inelastic collisions (set by default equal to 200 eV).
- **WCR**: This parameter is the cutoff energy loss (in eV) for hard bremsstrahlung emission (set by default equal to 200 eV).
- **DSMAX**: This parameter defines the maximum step length of electrons and positrons in the material. In mixed simulations of electron/positron transport, it is necessary to limit the lengths of each free jump so that it does not exceed a given value  $s_{max}$ . To accomplish this, the program samples the free path length  $s$  to the next interaction, but when  $s \geq s_{max}$  it only lets the particle advance a distance  $s_{max}$  along the direction of motion. At the end of the truncated free jump, the particle keeps its energy and direction of motion unaltered; however, for programming convenience, the particle suffers a delta interaction (actually, a non-interaction). When the sampled value of  $s$  is less than  $s_{max}$ , a real interaction is simulated. After the interaction (either real or delta), a new free path  $s$  is sampled, the particle is moved to a distance  $s_0 = \min(s, s_{max})$ , etc. From the Markovian character of the transport, it is clear that the insertion of delta interactions keeps the simulation unbiased. Parameter **DSMAX** is important only for thin bodies; in the case of program kernel, the simulation occurs in an infinite medium, and the step length control can be disabled by setting **DSMAX=1.0E20**.

>>>>>>> Interaction forcing

- **IFORCE - [KB,KPAR,ICOL,FORCER,WLOW,WHIG]**: By this parameter is activated the forcing of interactions of type **ICOL** of particles **KPAR** in the body **KB**. The PENELOPE code number (**ICOL**) for the various interaction events of the considered particles **KPAR** is shown in Tab 3.1. **FORCER** is the forcing factor which must be larger than unity. The values **WLOW** and **WHIG** are the limits of the weight window where interaction forcing is applied. The interaction forcing is a variance-reduction method [Salvat, 2011] in which the interaction probability of the process of interest **ICOL** of the particles **KPAR** is artificially increased in order to force the interaction of interest to occur more frequently than for the real process. In our case the interaction forcing is applied to obtain the resulting photon spectra of bremsstrahlung (**KPAR=1, ICOL=4**) and inner-shell ionization (**KPAR=1, ICOL=5**) in a reasonable computational time. This method consist in replacing the mean free path **MFP** of the considered interaction **ICOL** with a new mean free path defined as  $\text{MFP}/|\text{FORCER}|$ . The results of the forced simulation must be correct by

applying to all the simulated particles a weight defined as  $W_i = W_{i-1}/|\mathbf{FORCER}|$  where  $W_i$  is the corrective weight of the particle of the  $i$ -th generation, (for the primary particle  $W_1=1$ ). In our computation, the parameter **FORCER** is set equal to -8 for the bremsstrahlung interactions, and to -100 for the ISII interactions. **WLOW** and **WHIG** are set respectively equal to 0.01 and 10. A negative input value of **FORCER**, is assumed to mean that each particle should interact, on average and approximately, **FORCER**-times in a path length equal to the range of the particle with **E = SENERG**.

<b>ICOL</b>	<b>KPAR=1</b> (electrons)	<b>KPAR=2</b> (photons)	<b>KPAR=3</b> (positrons)
1	Artificial soft event (random hinge)	Rayleigh scattering	Artificial soft event (random hinge)
2	Hard elastic collision	Compton scattering	Hard elastic collision
3	Hard inelastic collision	Photoelectric absorption	Hard inelastic collision
4	Hard bremsstrahlung emission	Electron-positron pair production	Hard bremsstrahlung emission
5	ISII		ISII
6			Annihilation
7	Delta interaction	Delta interaction	Delta interaction
8	Auxiliary interaction	Auxiliary interaction	Auxiliary interaction

Tab 3.1. The PENELOPE code number (**ICOL**) for the various interaction events.

>>>>>>> Counter array dimensions and tallied ranges

- **NBE**: In this parameter is defined the energy windows and the number of bins for the energy discretization of the tallied distributions. In our case it is used an energy windows spacing from 0 keV to 150 keV with number of bins equal to 300.
- **NBANGL**: In this parameter is defined the number of bins considered for the angular discretization of the tallied distributions. In our computation it is set **NBANGL=200**.
- **NBZ**: In this parameter is defined the number of bins considered for the axial discretization of the tallied distributions. In our computation it is set **NBZ=200**.



- **NBR**: In this parameter is defined the number of bins considered for the radial discretization of the tallied distributions. In our computation it is set **NBR=200**.

>>>>>>> Job properties

- **RESUME**: In this section is defined the name of the dump file from which the program will resume the simulation from the point where it was left. In our computation it is set **RESUME=dump.dmp**.
- **DUMPTO**: In this section is defined the name of the dump file generated by the code after completing the simulation run. In our computation it is set **DUMPTO=dump.dmp**. This allows the simulation to be resumed to improve statistics. If the file dump.dmp already exists, it is overwritten.
- **DUMPP**: In this section is defined the period (in seconds) from which the code update the dump file defined in **DUMPTO**.
- **RSEED**: In this section is defined the Seeds of the random-number generator used by PENELOPE.
- **NSIMSH**: In this section is the fine the desired number of simulated shower (number of photons emitted by the considered primary source). In all our computations this number it is set equal to 1E6.
- **TIME**: In this section is defined the allotted simulation time (in seconds). To be sure that all the desired number of shower defined in **NSIMSH** was simulated, in all our computation this parameter is set equal to 1E19.
- **END**: End the reading of the KERNEL input file.

### 3.2.2 KERNEL output files

In the PENELOPE computation, the particles state is defined through the following parameters:

- **KPAR**: Kind of particle (1: electron, 2: photon, 3: positron).
- **E**: Current particle energy (eV) (kinetic energy for electrons and positrons).
- **X, Y, Z**: Position coordinates of the particle (cm).
- **U, V, W**: Direction cosines of the direction of movement.
- **WGHT**: A dummy variable in analogue simulations. When using variance-reduction methods, the particle weight is stored here.
- **IBODY**: This auxiliary flag serves to identify different bodies in complex material structures. The main program KERNEL simulates only one body and one material, so the value of **IBODY** is constant.
- **MAT**: Material where the particle moves, i.e., the one in the body labeled **IBODY**. Also this parameter is constant in kernel.

- **ILB**: An auxiliary array of 5 labels that describe the origin of secondary particles defined as:
  - **ILB(1)**: Generation of the particle; 1 for primary particles, 2 for their direct descendants, etc.
  - **ILB(2)**: Kind **KPAR** of parent particle, only if **ILB(1) > 1** (secondary particle).
  - **ILB(3)**: Interaction mechanism **ICOL** that originated the particle, only when **ILB(1) > 1**.
  - **ILB(4)**: A non-zero value identifies particles emitted from atomic relaxation events and describes the atomic transition where the particle was released. The numerical value is  $= Z \cdot 10^6 + IS1 \cdot 10^4 + IS2 \cdot 100 + IS3$ , where  $Z$  is the atomic number of the parent atom and  $IS1$ ,  $IS2$  and  $IS3$  are the labels of the active atomic electron shells defined as shown in table 3.2.
  - **ILB(5)**: This label can be defined by the user and it is transferred to all descendants of the particle.

Label	Shell
1	K
2	L1
3	L2
4	L3
5	M1
6	M2
7	M3
8	M4
9	M5
10-29	From N1 to Q1
30	Outer shell

Tab 3.2. Numerical labels used to designate atomic electron shells. In the case of non-radiative transitions, the label 30 indicates shells beyond the N7 shell.

Through the reading of these parameters for each simulated particle, in order to evaluate the contribution to the total photon spectrum coming from the electronic interactions, the program **KERNEL** scores quantities which describe angular, energy and spatial distribution of photons emitted by bremsstrahlung and inner-shell ionization. The separation of the scored different processes is done through the evaluation of the labels **ILB** assigned by **PENELOPE** assigns to all simulated particles. In particular, the label stored in the variable **ILB(3)** is used to discriminate the interaction mechanism **ICOL** (see Tab. 3.1) that originated the particle. In case of atomic relaxation event the label stored in the variable **ILB(4)** is used to discriminate the shell from which the scored particle is originated (see Tab. 3.2). A list of the output files generated by **KERNEL** is shown below in Tab 3.3

<b>File</b>	<b>Description</b>
e_brm_tot.dat	Energy distribution of bremsstrahlung photons due to all secondary electrons
e_brm_c.dat	Energy distribution of bremsstrahlung photons due to secondary electrons produced by Compton scattering
e_brm_pk.dat	Energy distribution of bremsstrahlung photons due to secondary electrons produced by photoelectric effect from K shell
e_brm_pl.dat	Energy distribution of bremsstrahlung photons due to secondary electrons produced by photoelectric effect from L shells
e_brm_pm.dat	Energy distribution of bremsstrahlung photons due to secondary electrons produced by photoelectric effect from M shells
e_brm_pnq.dat	Energy distribution of bremsstrahlung photons due to secondary electrons produced by photoelectric effect from N-Q shell. PENELOPE set as belonging to the N-Q shells all photoelectrons generated from a shell with binding energy lower than the chosen cut off value $E_{ABS}$
e_brm_2t.dat	Energy distribution of bremsstrahlung photons due to multiple scattering of secondary electrons
e_brm_pA.dat	Energy distribution of bremsstrahlung photons due to Auger effect and Coster-Kronig transitions
r_brm_tot.dat	Radial distribution of photons by bremsstrahlung
z_brm_tot.dat	Axial distribution of photons by bremsstrahlung
ct_brm_tot.dat	Angular distribution of photons by bremsstrahlung
e_cmp.dat	Energy distribution of Compton photons ( $1^\circ$ order interaction)
e_cmp_r.dat	Energy distribution of photons by relaxation events due to subsequent to a Compton ionization
e_ph_r.dat	Energy distribution of characteristic photons ( $1^\circ$ order interaction)
e_isii_c.dat	Energy distribution of inner shell impact ionization photons due to secondary electrons produced by Compton scattering
e_isii_p.dat	Energy distribution of inner shell impact ionization photons due to secondary electrons produced by photoelectric effect
PH-lines.dat	Table of photoelectric characteristic photons.
ION-lines.dat	Table of characteristic lines' energy and probability of inner shell impact ionization
ION-lines-c.dat	Table of characteristic lines' energy and probability of inner shell impact ionization subsequent to a Compton scattering
ION-lines-ph.dat	Table of characteristic lines' energy and probability of inner shell impact ionization subsequent to a photoelectric effect

Tab. 3.3 Output files generated from the code KERNEL.

Through the code `KERNEL` the contributions described in Tab. 3.3 are evaluated and then studied in terms of angle, space and energy for all elements with  $Z$  from 1 to 92, by using the following selected source energy in the range 1-150 keV:

(1 keV, 2 keV, 5 keV, 10 keV, 15 keV, 20 keV, 25 keV, 30 keV, 35 keV, 40 keV, 45 keV, 50 keV, 55 keV, 60 keV, 65 keV, 70 keV, 75 keV, 80 keV, 85 keV, 90 keV, 95 keV, 100 keV, 125 keV and 150 keV).

Moreover, for all elements it is added the computations related to sources energies closely before and after the binding energy of each shell (50 eV before and 50 eV after each binding energy values). In this way for each element the number of simulation is equal to the sum of the 24 fixed set of source energies showed before plus two time the number of the binding energies of the considered element.

Because of the large amount of time required to complete all computations, it is implemented a parallelized 16 threads program in FORTRAN 90/95 by using the application program interface Open MP (Open MP ARB). This parallelized code consists in four master threads which simulate the 92 considered elements, and 4 slave threads which simulate the set of considered source energies for each element.

The final result of the computation consists in 92 folders (one for each element). In each one of these elements' folders there are a number of folders equal to the number of the simulated source energy of the element. In these source energy folders are included the output files described in Tab. 3.3. The full computation is done on an HP Z800 workstation with a dual CPU Intel® Xeon® X5550 @2.67GHz, @2.66GHz, requiring 14 days, 4 hours, 42 minutes and 47 seconds.

In the following two sections are presented respectively the results obtained for the ISII by Fernandez et al. [Fernandez, 2013] and the results obtained in this work on the bremsstrahlung emission.

### 3.3 Radiative contribution of inner shell impact ionization

In this section it is shown the results obtained by Fernandez et al. [Fernandez, 2013], [Fernandez, 2014-2] on the characterization of the ISII contribution on X-ray transport due to secondary electrons. In the cited work the ISII contribute was studied in terms of angle, space and energy. From the simulations it was demonstrated that the source of photons from electron interactions can be safely represented as a point source and that the radiative emission from ISII can be assumed as isotropic, i.e. it is licit to consider that the ISII contribution is isotropic and occurs at the same place of the photon collision. To quantify the ISII contribution in terms of energy, PENELOPE calculations were performed for all the lines of the elements  $Z=11-92$  in the energy range 1-150 keV. To parameterize the contribution for a generic energy, the whole energetic interval was divided into 5 energy regions delimited by K, L1, L2 and L3 absorption edges (see Fig. 3.3). A simple parametric expression was defined for every region.

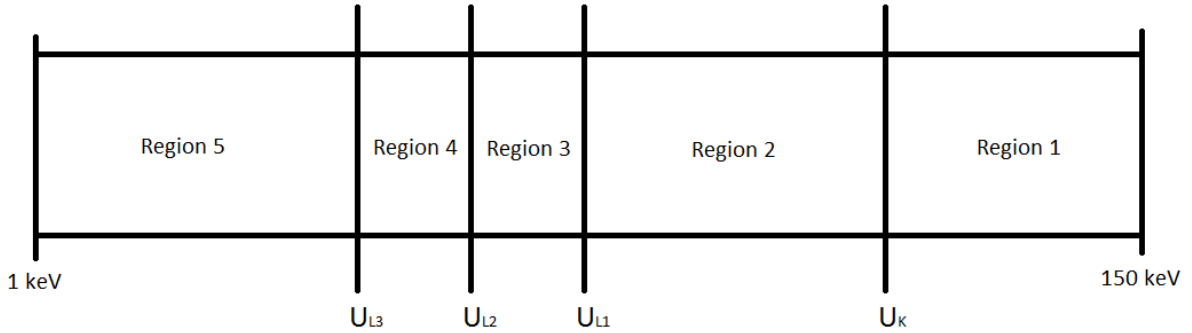


Fig. 3.3. Schematic representation of the division of the energy interval.

The best fit of the ISII energy contribution at each interval was computed using 4 coefficients as follows [Fernandez, 2013]:

$$f_{ISII}(E) = \exp \left[ \sum_{k=1}^3 \alpha_{kR} \ln(E^k) \right] \quad (3.7)$$

It was found that since the electrons lose their energy more efficiently in the low energy range, the computed contribution is always higher for low energy lines, and, therefore, for K-lines of low  $Z$  elements; for L-lines for medium  $Z$  elements; and for M-lines for high  $Z$  elements.

It was demonstrated that for all cases the contribution of ISII to the total emission probability grows with energy. Starting from these results, Fernandez et al. develop an externally corrective kernel terms to the photon Boltzmann transport model able to describe the ISII radiative contribution due to secondary electrons to the radiation field. As the ISII contributes influences only the intensities of the characteristic lines of the spectra, the contribution can be considered as a correction of the photoelectric effect single process kernel. To avoid data-base differences between PENELOPE and other transport codes the electron contribution  $f_{ISII}(E')$  was computed as a relative one, in units of the photon contribution  $Q_{E_i}(E')$ . The corrective term is assembled as:

$$\Delta k_{PE_i}(\vec{\omega}', E', \vec{\omega}, E) = \frac{1}{4\pi} f_{ISII}(E') Q_{E_i}(E') \delta(E - E_i) [1 - U(E_{e_i} - E')] \quad (3.8)$$

where  $f_{ISII}(E')$  is defined as:

$$f_{ISII}(E') = \frac{\Delta Q_{E_i}(E')|_{electron}}{Q_{E_i}(E')} \quad (3.9)$$

Thus, the new corrected kernel comprising electron contributions for a single line introduced by Fernandez et al. has the expression:

$$\Delta k_{PE_i}(\vec{\omega}', E', \vec{\omega}, E) = \frac{1}{4\pi} [1 + f_{ISII}(E')] Q_{E_i}(E') \delta(E - E_i) [1 - U(E_{e_i} - E')] \quad (3.10)$$

with the relative correction parameterized as:

$$f_{ISII}(E) = \sum_{R=1}^5 H_R(E) \exp \left[ \sum_{k=1}^3 \alpha_{kR} \ln(E^k) \right] \quad (3.11)$$

where  $H_R(E)$  assumes the values:

$$H_R(E) = \begin{cases} 1, & \text{if } E \text{ belongs to region } R \\ 0, & \text{otherwise} \end{cases} \quad (3.12)$$

More information on the results obtained by Fernandez et al. can be found in the cited articles [Fernandez, 2013], [Fernandez, 2014-2].

## 3.4 Radiative contribution of Bremsstrahlung

With a similar procedure as used on the characterization of the ISII radiative contribution by Fernandez et al. [Fernandez, 2013], [Fernandez, 2014-2], in this work the bremsstrahlung contribution due to secondary electrons is evaluated and then studied in terms of angle, space and energy for all elements with  $Z$  from 1 to 92 by using the code KERNEL.

### 3.4.1 Bremsstrahlung angular distribution

The direction of the photon emitted by bremsstrahlung is defined by the polar angle  $\theta$  and the azimuthal angle  $\phi$ . For isotropic media, with randomly oriented atoms or molecules, the bremsstrahlung DCS is independent of  $\phi$ . Fig. 3.4 shows the polar angular distribution of photons emitted by bremsstrahlung in aluminum, copper, silver and gold for 5 and 50 keV of primary photon energy. The graphs show the presence of a tiny slope, which seems to become smaller as the atomic number  $Z$  increases and the energy source value decreases. Indeed, the slope can be assumed negligible compared to the obtained probability distribution function (PDF) values. Since electrons suffer a great number of interactions before being absorbed, it is predicted that this angular distribution will further average as a consequence of the scattering. Therefore it can be assumed that the photon source from bremsstrahlung emission is isotropic.

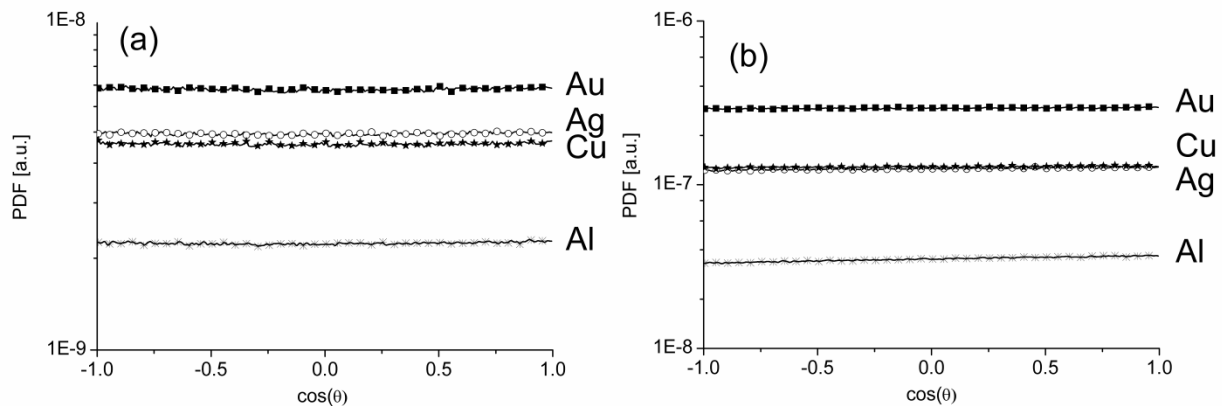


Fig. 3.4. Polar angular distribution of photons emitted by bremsstrahlung in Al, Cu, Ag and Au with primary photon sources of 5 keV (a) and 50 keV (b). The graphs show that the slope is negligible for all these elements.



### 3.4.2 Bremsstrahlung spatial distribution

Fig. 3.5 and Fig. 3.6 show, respectively, the radial and axial distributions of photons emitted by bremsstrahlung in Al and Ag for 5 and 50 keV of primary photon energy. The spatial distribution of the photons emitted by secondary electrons is always a fraction of the Bethe range  $R(E_e)$  defined as the average path length travelled by a particle of kinetic energy  $E_e$  (in an infinite medium) before being absorbed. For a photon transport code, the length scale for transport processes is the photon mean free path  $\lambda_p$ . As shown by Fernandez et al [Fernandez, 2013], [Fernandez, 2014-2], this quantity compared with the Bethe range is always of a greater order of magnitude, i.e.  $\tau_s = R(E_e)/\lambda_p \ll 1$ . For this reason, the source of photons generated from electron interactions can be safely represented as a point source.

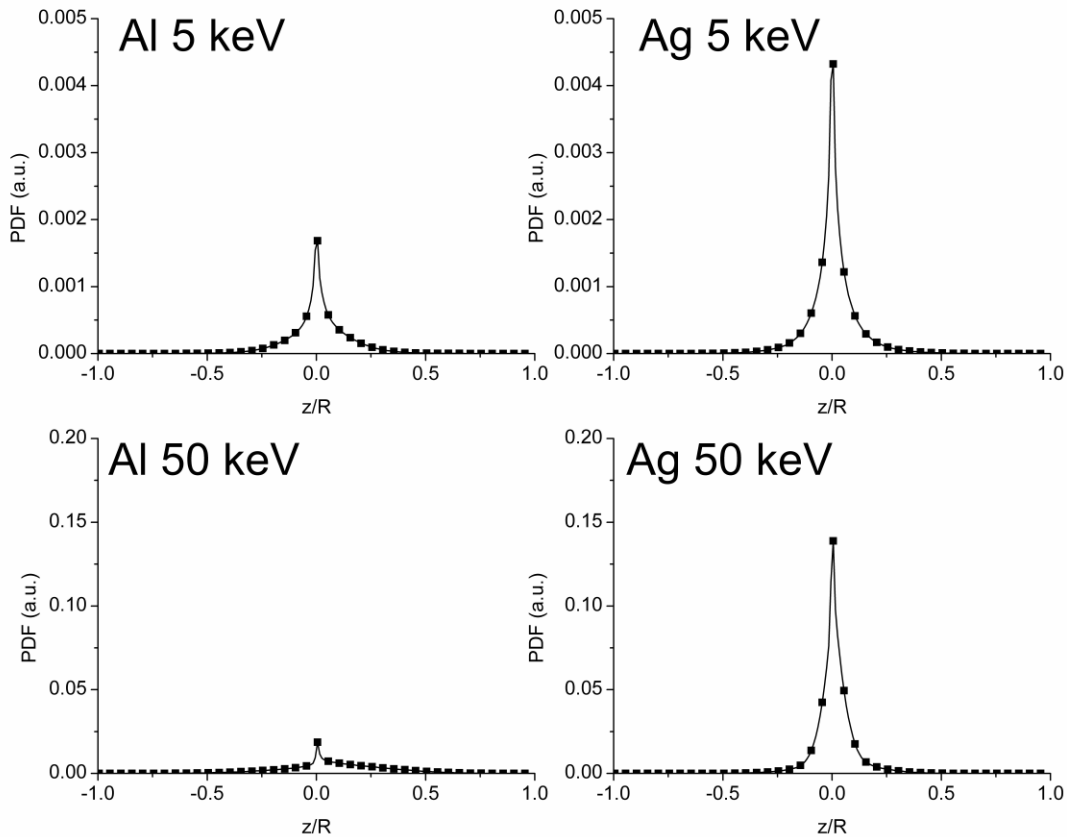


Fig. 3.5. Axial distribution of photons emitted by bremsstrahlung in Al and Ag with a primary photon source of 5 keV (top panel) and 50 keV (bottom panel).

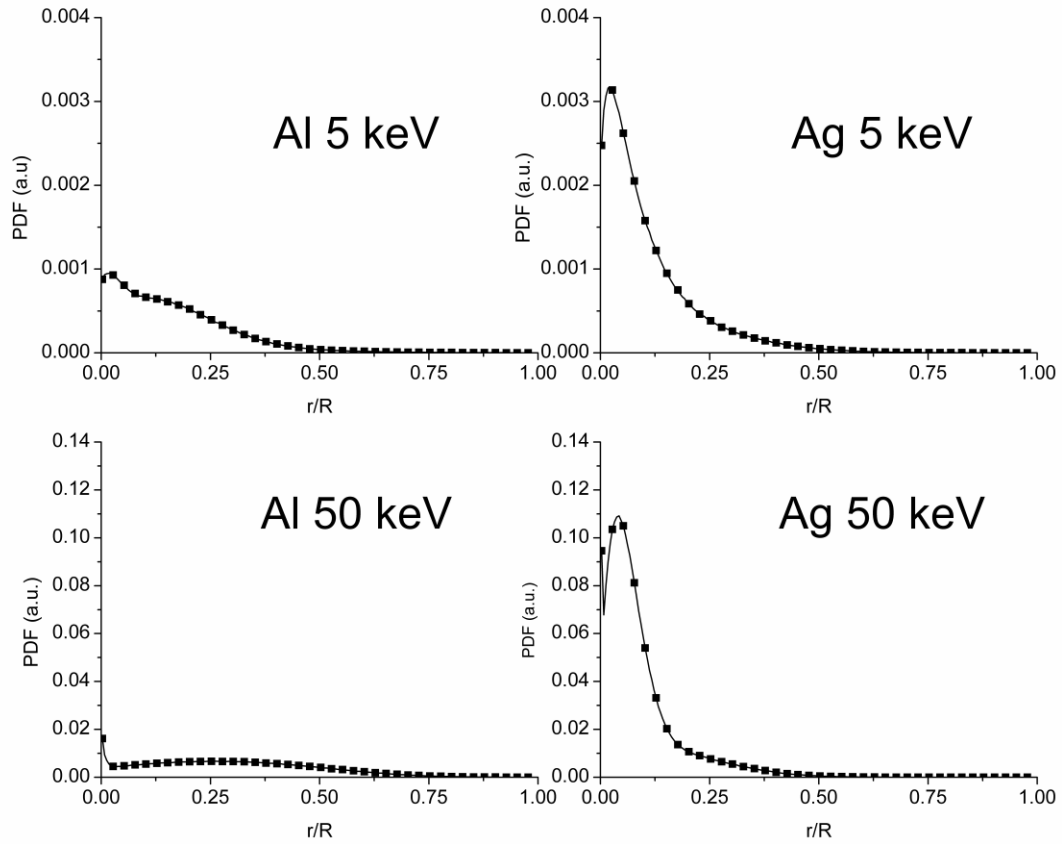


Fig. 3.6. Radial distribution of photons emitted by bremsstrahlung in Al and Ag with a primary photon source of 5 keV (top panel) and 50 keV (bottom panel).

### 3.4.3 Bremsstrahlung energy distribution

As shown in the section 3.1.2, PENELOPE simulates the bremsstrahlung emission with a differential cross section which is:

$$\frac{d\sigma_{br}}{dE} \propto \frac{Z^2}{E} \quad (3.13)$$

where  $E$  is the energy of the emitted photon and  $Z$  the atomic number. As shown previously in section 3.2.2, the bremsstrahlung contribution is computed for all the different interactions which generate secondary electrons: Compton scattering, Auger effect, multiple scattering of electrons and photoelectric effect for all the shells. As an example, Fig. 3.7 shows for Cu and Au, the total bremsstrahlung distribution and the single distributions due to electrons produced by the different processes: Compton electrons, Auger electrons, multiple scattering of electrons, and photoelectrons from different shells. As expected, the resulting spectra are proportional to  $1/E$  and the contribution from bremsstrahlung emission increases with  $Z$ . Different accumulators are used to store contributions from all the K, L, and M shells and a single accumulator for the shells N-Q. By default, in PENELOPE, bremsstrahlung produced by photoelectrons coming from shells with binding energy lower than a pre-defined cut off is stored in the N-Q accumulator. The cut off value used in our computations is 200 eV for photon source energies lower than 5 keV, and 500 eV otherwise.

The Cu distributions in Fig. 3.7 do not show any M-shell contribution. This is because the M-shells accumulator is empty (M1 binding energy is 120 eV), and the bremsstrahlung from M-shells photoelectrons is stored in the N-Q accumulator. The K-shell contribution of Au is not present because the binding energy (80.7 keV) is higher than the photon source energy. It is apparent the presence of a discontinuity associated to the absorption edges. As an example, the starting point of the K-shell distribution in copper is 41 keV which corresponds to the difference between the photon source energy (50 keV) and the absorption edge energy of the considered shell (8.993 keV).

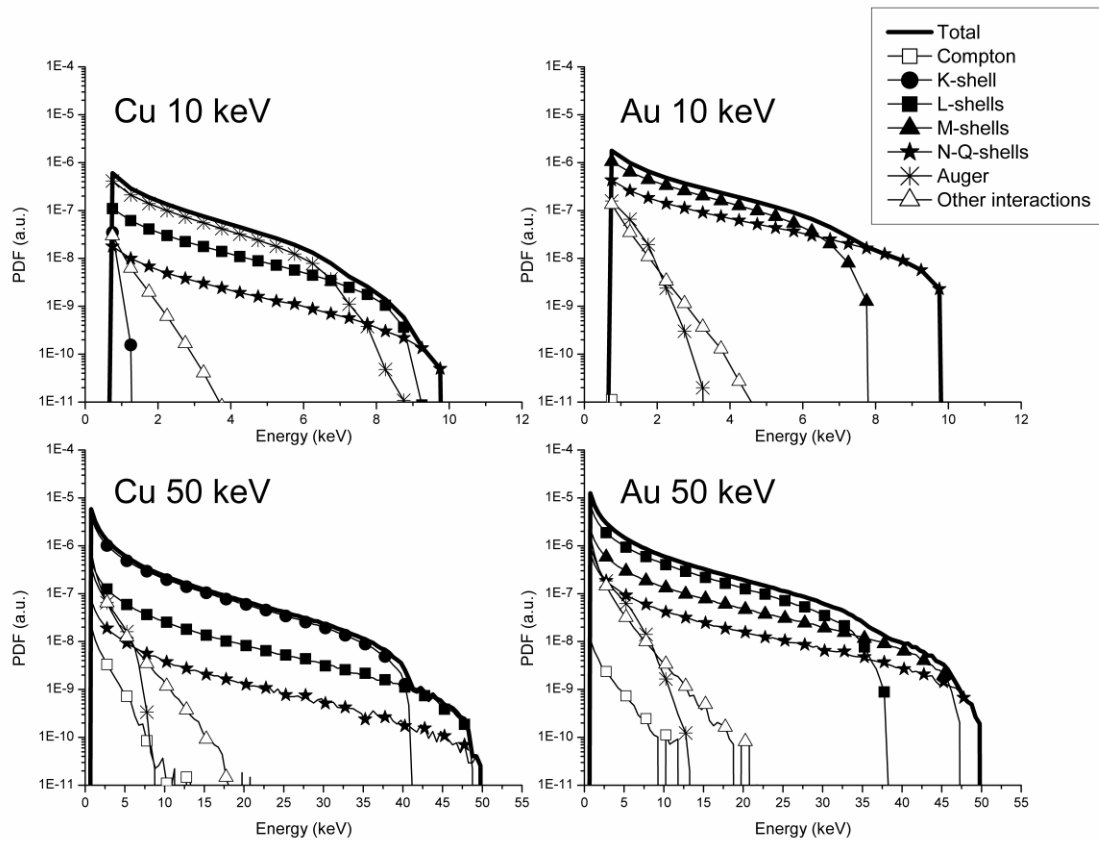


Fig. 3.7. Bremsstrahlung distribution for Cu and Au at photon source energies of 10 keV and 50 keV. The single contributions due to Compton electrons (Compton), photoelectrons from the K- (K-shell), L- (L-shells), M- (M-shells), and N-Q shells (N-Q-shells), Auger electrons (Auger), and multiple scattering of electrons (Other interactions), concur to form the total bremsstrahlung distribution (Total).

### 3.4.4 New bremsstrahlung kernel

As the angular distribution of the photons due to bremsstrahlung can be safely considered as isotropic, and the source of photons from electron interactions is well represented as a point source, it is valid to consider that the emission is isotropic and occurs at the same place of the photon collision. Concerning the energy distribution, it is shown that bremsstrahlung depends on the energy of the incoming photon. The bremsstrahlung can be added to the transport equation as a new kernel  $k_B(\omega', E', \omega, E)$  which contains the continuous distribution in energy  $f_B(E', E)$ :

$$k_B(\omega', E', \omega, E) = \frac{1}{4\pi} f_B(E', E) \quad (3.14)$$

where the factor  $(4\pi)^{-1}$  denotes the isotropic behavior of the kernel,  $\omega', E'$  are the direction and energy of the photon source and  $\omega, E$  those of the exiting radiation.

Some attempts were made to find a parametric function to reproduce these distributions for different energies and materials, but without a satisfactory result. Therefore, instead to find an analytical expression of the PDF, the bremsstrahlung distribution is computed for selected source energies and stored in a data library. For all the elements  $Z=1-92$ , the database contains the computed bremsstrahlung distribution  $f_B(E', E)|_{PEN}$  for the following fixed photon source energies  $E'$ : 1, 2, 5, 10, 15, 20, 25, 30, 35, 40, 45, 50, 55, 60, 65, 70, 75, 80, 85, 90, 95, 100, 125, and 150 keV. In addition, the data library comprises the bremsstrahlung distribution computed at photon source energies closely before and after the binding energy of each shell. This allows the insertion of all the discontinuities for each element. Each distribution is computed in the energy range  $E=0-150$  keV with a discretization of 500 eV. The choice of this discretization is a compromise between an acceptable energy resolution and a reasonable statistics for the MC simulation. Some examples of bremsstrahlung distribution from the created library database are shown in Fig. 3.8. The time to compute the full data library is 7137 s for Cu.

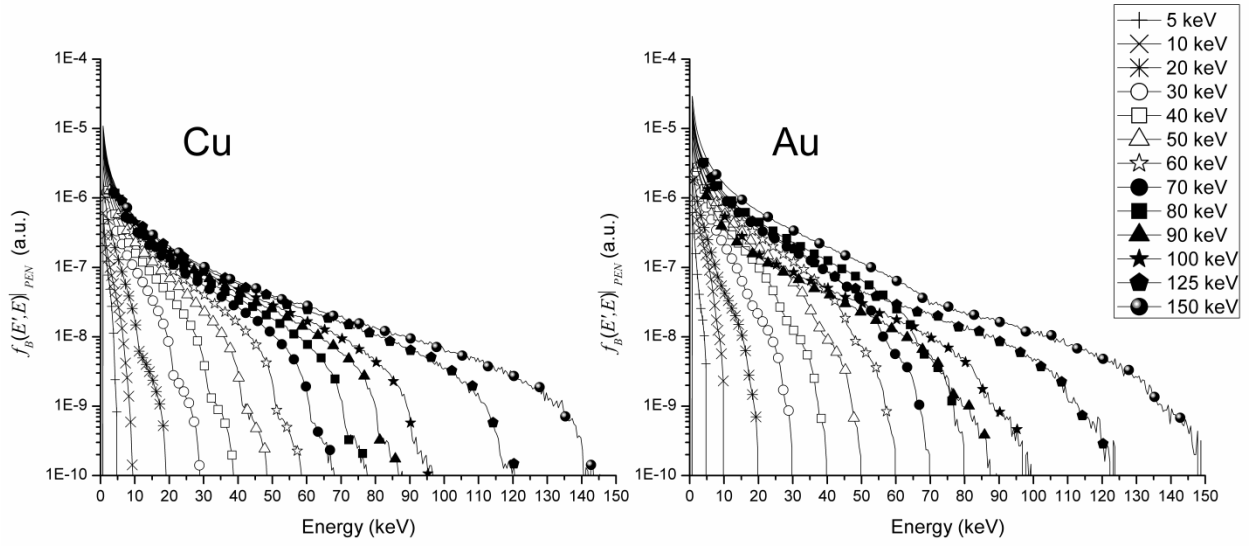


Fig. 3.9. Excerpt of the database for Cu and Au for the following fixed photon source energies: 5, 10, 20, 30, 40, 50, 60, 70, 80, 90, 100, 125, and 150 keV. Symbols are used to identify the different distributions and are not in correspondence with the single values.

For an arbitrary value of the source energy  $E'$  the contribution is obtained by interpolating the data library using the ad-hoc 2D interpolation scheme presented by Fernandez et al [Fernandez, 2007-2]:

$$f_B(\bar{x}, E)|_{PEN} = \frac{(E'_2 - E') f_B(x_1, E'_1)|_{PEN} + (E' - E'_1) f_B(x_2, E'_2)|_{PEN}}{E'_2 - E'_1} \quad (3.15)$$

where  $x_1$  and  $x_2$  are defined as

$$x_1 = \bar{x} \frac{E'_1}{E'} \quad ; \quad x_2 = \bar{x} \frac{E'_2}{E'} \quad (3.16)$$

and  $\bar{x} \in [0, E']$  denotes the central energy of one energy bin of the discretization.  $E'_1$  and  $E'_2$  are the adjacent energies, respectively smaller and bigger than  $E'$ , for which the bremsstrahlung distribution is present in the database. Fig. 3.9 illustrates the quality of the interpolation for a photon source energy of 9 keV (not present in the database). The direct calculation of the bremsstrahlung distribution with PENELOPE is compared with the distribution obtained by interpolating the data library. The good agreement obtained is illustrated for two elements: Cu and Au. The low energy discrepancy for Au is due to the 500 eV energy resolution of the stored distributions.

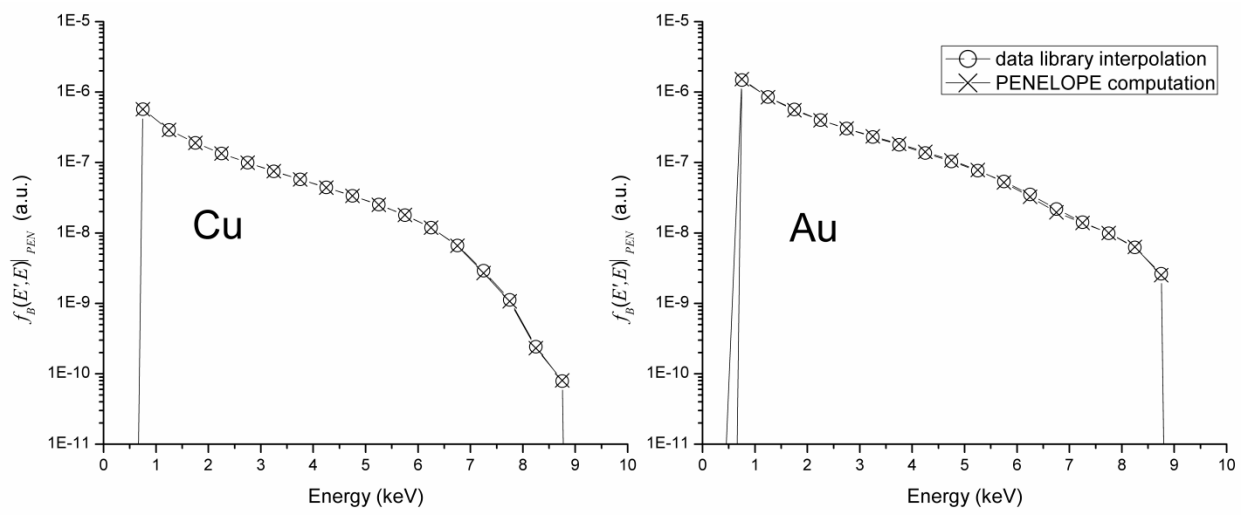


Fig. 3.9. Comparison between the bremsstrahlung distributions computed with PENELOPE and the interpolations from the library database, for Cu and Au, with 9 keV photon source energy. It is apparent the excellent agreement.

To avoid data-base differences between PENELOPE and other transport codes,  $f_B(E', E)$  is computed in units of the Compton scattering coefficient:

$$\tilde{f}_B(E', E)|_{PEN} = \frac{f_B(E', E)|_{PEN}}{\sigma_C(E')|_{PEN}} \quad (3.17)$$

where  $f_B(E', E)|_{PEN}$  and  $\sigma_C(E')|_{PEN}$  are respectively the bremsstrahlung PDF and the Compton scattering coefficient computed with PENELOPE.

To include the bremsstrahlung in a generic photon transport code it is necessary to multiply the value of the normalized bremsstrahlung PDF  $\tilde{f}_B(E', E)|_{PEN}$  by the Compton scattering coefficient  $\sigma_C(E')$  computed within the code in which the bremsstrahlung distribution has to be introduced:

$$f_B(E', E) = \tilde{f}_B(E', E)|_{PEN} \cdot \sigma_C(E') \quad (3.18)$$

### 3.4.5 Application to a synchrotron experiment

The following example illustrates the potential of the data library and the improvement in the calculation speed. The experimental data come from a measurement performed at BL-14, KEK [Hirayama, 2005]. The experimental set-up reproduces the one described in Namito et al. [Namito, 2000]. The monochromatic source at 40 keV is linearly polarized with polarization degree  $P=0.885$ . The scattered spectrum is collected by two Ge detectors: one detector (Ge2) located in the plane of the incident polarization vector ( $\varphi=0^\circ$ ), and the other (Ge1) in the plane perpendicular to it ( $\varphi=90^\circ$ ). The scattering angle is  $\theta=90^\circ$ .

The transport in the Cu target (thickness 0.2 cm and density  $8.92 \text{ g/cm}^3$ ) is simulated with the PENELOPE main program PENMAIN [Salvat, 2011]. The input of PENMAIN example 5 included in the PENELOPE distribution is modified to tally the bremsstrahlung distribution due to secondary electrons and to score the photon spectrum in the range 1-40 keV. It is worth noting that to simulate the bremsstrahlung emission with good statistics it was necessary to apply collision forcing in the Cu target and change the energies cut-off, at the cost of having a loss of performance for the higher energy part of the spectrum. The complete simulation took more than one day on an HP xw8600 workstation with an Intel® Xeon® dual CPU X5450@3.00GHz. To improve the computational time, it is possible to split the energy range in two intervals, above 30 keV and below 30 keV, and perform two PENELOPE runs with different parameters.

The bremsstrahlung contribution is computed also by means of the new data library. The content of the data library for Cu at 40 keV can be seen in Fig. 3.8. The bremsstrahlung is calculated only for the first photon collision (40 keV photons). To compute the intensity reaching the detector for the considered geometry it is necessary to include the attenuation in the target. It is well known that the first order flux in reflection geometry is expressed analytically as:



$$f^{(1)}(t, \vec{\omega}, E) = \frac{I'}{|\eta||\eta'|} k(\omega', E', \omega, E) \int_0^t \exp[-(\alpha + \alpha')\tau] d\tau \quad (3.19)$$

with

$$\alpha = \frac{\mu(E)}{|\eta|} \quad ; \quad \alpha' = \frac{\mu(E')}{|\eta'|} \quad (3.20)$$

In the above expressions,  $t$  is the target thickness,  $\eta = \cos(\vartheta)$ ,  $\eta' = \cos(\vartheta')$ ,  $\vartheta$  and  $\vartheta'$  being the polar angles,  $\mu$  is the mass attenuation coefficient,  $k$  is the kernel, and  $I'$  is the intensity of the monochromatic source of energy  $E'$ . Integrating Eq. 3.19 and including the bremsstrahlung database by means of the kernel in Eq. 3.14, it is possible to compute the first order contribution to the photon transport due to the bremsstrahlung as:

$$f^{(1)}(t, \vec{\omega}, E) = \frac{I'}{|\eta||\eta'|} \frac{1}{4\pi} f_B(E', E) \frac{1 - \exp[-(\alpha + \alpha')t]}{\alpha + \alpha'} \quad (3.21)$$

with  $E'=40$  keV. Fig. 3.10 shows the comparison between the complete PENELOPE simulation for the given experimental set-up and the bremsstrahlung contribution computed with Eq. 3.21. It is apparent the agreement in the description of the bremsstrahlung. The gain in the computational speed is enormous. The time to read the data library and obtain the bremsstrahlung distribution is less than 0.03 s. Given the values of the mass attenuation coefficients and of  $f_B(E', E)$ , the first order contribution can be computed almost instantaneously with a simple worksheet.

To illustrate the use of the data base in a photon transport code, the same experimental set-up is simulated with the code MCSHAPE, using a multiple stage procedure as the one described in Fernandez and Scot [Fernandez, 2009]. First, the transport in the target is computed with MCSHAPE [Fernandez, 2004], [Fernandez, 2007] (Fig. 3.11a). Then, the bremsstrahlung spectrum obtained with Eq. 3.21 is added to the transport result. In a successive simulation, the energy deposition spectrum in the detector is included by running the code MCSHAPE in “detector mode” and using as source the results of previous step (Fig. 3.11b). Finally, the

MCSHAPE results are convoluted with the detector resolution and the effects of charge collection with the code RESOLUTION [Fernandez, 2009], [Fernandez, 2014-3] (Fig. 3.11c). It is apparent the very good agreement between the experiment and the MC simulation, once the influence of the detection system and the bremsstrahlung are included. Only two regions of the measure present discrepancies. The one below the characteristic Cu K X-ray lines deserves further investigation because it cannot be explained as bremsstrahlung or incomplete charge collection. It may be due to KLL and KLM radiative Auger effects. The other region is the energy range from 10 keV to 20 keV which can be now partially explained by bremsstrahlung. According to Namito et al. [Namito, 2000] this region can host pulse pile-up. Since the effective number of counts of the measurement and information on the acquisition electronics are not available, it is not possible to apply the pulse pile-up correction to the measured spectrum.

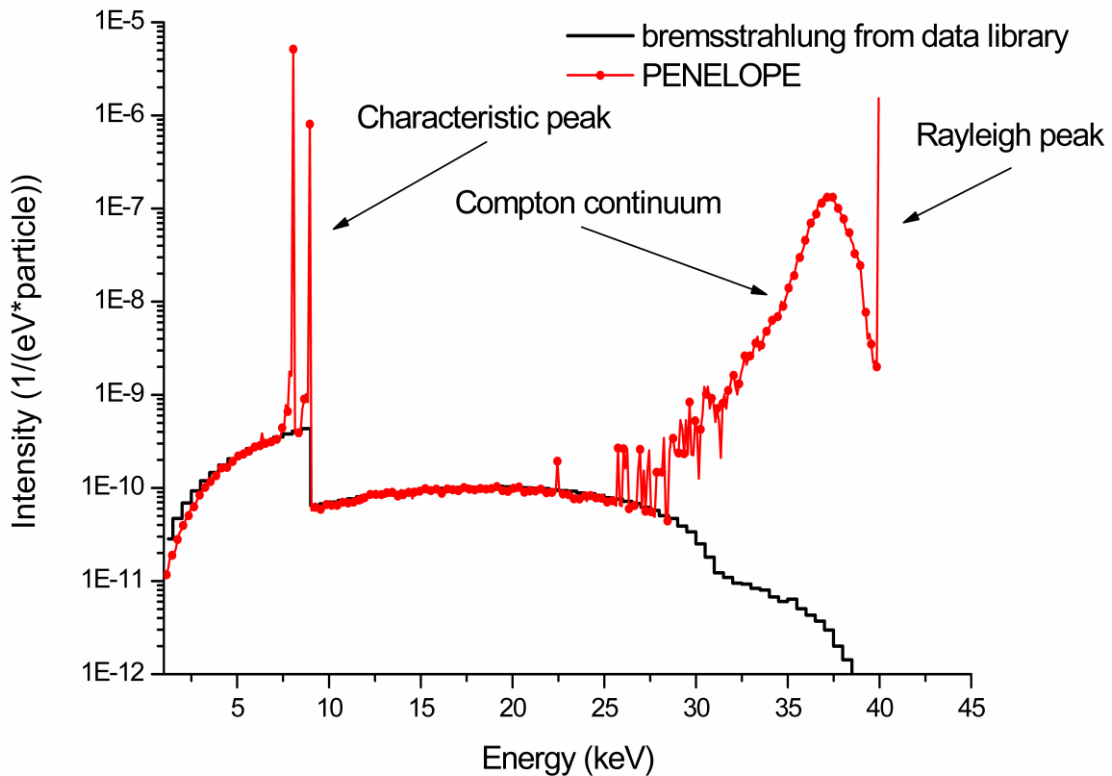


Fig. 3.10. Simulation of a Cu specimen, using as source a synchrotron beam at 40 keV. The experimental set up is described in Namito et al. [Namito, 2000]. The figure shows the comparison between the complete PENELOPE simulation and the first order intensity of bremsstrahlung computed using the data library. It is apparent the excellent agreement in the description of the continuous bremsstrahlung background.

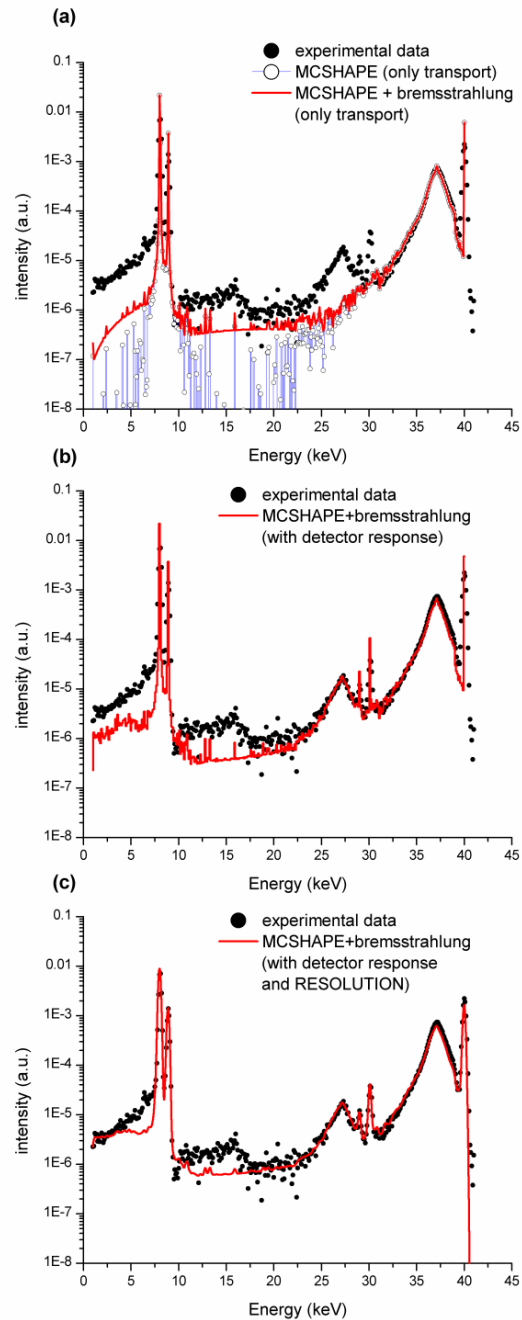


Fig. 3.11. Comparison between the experimental data from Namito et al. [Namito, 2000] with (a) the simulation of the transport in the target performed with the MCSHAPE with and without bremsstrahlung; (b) the simulation with MCSHAPE including bremsstrahlung and the detector response computed with MCSHAPE; and (c) the simulation of MCSHAPE including bremsstrahlung, the detector response computed with MCSHAPE, and the effects of resolution and charge collection computed with RESOLUTION [Fernandez, 2009], [Fernandez, 2014-3].



## 4 Conclusion

---

The first part of this work deals with the study of the inverse (or unfolding) problem solution in the X-ray spectroscopy field. An original strategy to optimally solve the inverse problem by using the maximum entropy principle through a combination of the codes GRAVEL and MAXED is illustrated. The strategy also allows the indirect evaluation of the quality of the model used to describe the detector response function (DRF), providing a measure of the consistency between the used detector response model and the measurement accuracy. It is built the code UMESTRAT, to apply the described unfolding strategy in a semiautomatic way to any X-ray spectrometry measurement. UMESTRAT also gives a graphical representation of all the intermediate steps of the unfolding. The application of UMESTRAT is shown with a computational example. From the obtained results it can be stressed that UMESTRAT successfully solve the unfolding problem in the X-ray energy regime by optimally resolving peak overlapping and removing the noise in the background of the measured spectrum.

The second part of this work deals with the improvement of the Boltzmann model used to describe a generic X-ray transport process, by studying two radiative interactions neglected in the current photon models. Firstly it is studied the characteristic line emission due to Compton ionization. In a second place it is characterized the bremsstrahlung radiative contribution due the secondary electrons generated during a generic X-ray transport process.

To characterize the XRF emission due to Compton ionization it is developed a strategy that allows the evaluation of this contribution for the shells K, L and M of all elements with  $Z$  from 11 to 92. The obtained Compton cross section is compared with the corresponding photoelectrical one for each one of the considered shells. The mentioned strategy can be summarized in three steps: (a) compute the single shell Compton cross section  $\sigma_{C_i}$  by means of a mixed procedure involving both WH and IA approximation; (b) compute the single shell photoelectric cross section  $\tau_i$  using different available data libraries; and (c) evaluate the ratio  $\sigma_{C_i}/\tau_i$  as a function of the primary photon energy  $E'$ . The single shell Compton cross section  $\sigma_{C_i}$  is evaluated by means of both the WH and the IA approximations as  $\sigma_{C_i} = (\sigma_{C_i}^{IA}/\sigma_C^{IA}) \cdot \sigma_C^{WH}$ . This mixed procedure allows the conservation of all the advantages of the approximations used. The single shell Compton cross section in the IA approximation is evaluated together with the total Compton cross section in the IA and in the WH approximation for the considered shells of all the elements in the energy range 1-1000 keV. The single shell photoelectric cross section  $\tau_i$  is evaluated by using two different data libraries: the EPDL97 database from Cullen et al. [Cullen, 1997]; the attenuation coefficient data tables and fitting functions from McMaster et al. [McMaster, 1969]. The ratio  $\sigma_{C_i}/\tau_i$  is computed for both data libraries (EPDL97 and McMaster) as a function of the excitation energy in the range 1-1000 keV for the shells K to M5 of all considered elements with  $Z$  from 11 to 92. Starting from these results it is developed a FORTRAN code that allows, for each shell  $i$  of the considered elements, the computation of the energy values  $E'(Z)$  for which the ratio  $\sigma_{C_i}/\tau_i$  becomes equal to a given fixed percentage value. From the obtained results it can be asserted that the EPDL97 allows a better description of the magnitude of interest. It is then derived the energy values at which the Compton interaction becomes the prevailing process to produce ionization at the K to M5 shells. In particular, in the X-ray energy regime (1-150 keV), it is showed that the XRF contribution from Compton ionization becomes bigger than the photoelectrical one ( $\sigma_{C_i}/\tau_i \geq 100\%$ ): for all elements with  $Z \leq 17$  for the K shell; for all elements with  $Z \leq 29$  for the L1 shell; for all elements with  $Z \leq 48$  for the L2 shell; for all elements with  $Z \leq 52$  for the L3 shell; for all elements with  $Z \leq 44$  for the M1 shell; for all elements with  $Z \leq 62$  for the M2 shell; for all elements with  $Z \leq 68$  for the M3 shell; for all elements with  $Z \leq 92$  for the M4 shell and for all elements with  $Z \leq 92$  for the M5 shell. The obtained results show that the XRF contribution from Compton single shell ionization plays an important role in the description of the radiation field in X-ray spectrometry. It is then implemented a FORTRAN code that, by using a polynomial fitting method, allows to express the percentage distributions  $E'(Z)$  computed for an arbitrary percentage value,  $\sigma_{C_i}/\tau_i$  with a fourth degree polynomial equation. The fitting coefficients obtained for some important percentages (1%, 5%, 10%, 20%, 50% and 100%) are given in tables and the goodness of the fitting is showed with some examples. Finally a new kernel for the XRF from Compton ionization is introduced in the Boltzmann model as a correction of the emission kernel from photoelectric ionization. This new kernel expression allows the addition to the Boltzmann model of atomic relaxation contribution due to Compton ionization process for each shell from K to M5. Some attempts to find a parametric function capable to describe the energy dependences of the XRF correction from Compton ionization need to be investigated in the future.

To characterize the radiative contribution due to the bremsstrahlung of secondary electrons it is elaborated a new photon transport model which comprises the bremsstrahlung contribution due to the coupled photon-electron transport process as a coupling term in the Boltzmann equation. The bremsstrahlung of secondary electrons is studied, in a similar way as done for the inner shell impact ionization by Fernandez [Fernandez, 2014-2]. The main program KERNEL is adapted to simulate the coupled photon-electron transport by using the Monte Carlo code PENELOPE. The bremsstrahlung radiation is characterized in terms of space, angle and energy, for all elements with  $Z=1-92$  and for a fixed set of photonic source energies in the range 1–150 keV. It is demonstrated that bremsstrahlung radiative contribution can be well approximated with an isotropic point photon source. The bremsstrahlung energetic contributions are characterized separately for each interaction from which the secondary electron is been created during an X-ray transport process. It is created a data library comprising the energetic distributions of bremsstrahlung for a fixed set of source energies and for all elements with  $Z=1-92$ . For arbitrary energy values the contribution is computed using a 2D ad hoc interpolation method, giving optimal results. It is developed finally a new bremsstrahlung kernel which allows the introduction of this contribution in the modified Boltzmann equation through the use of the created data library. An example of the simulation of a synchrotron experiment is shown. It is apparent that the simulation can reproduce well most of the measured spectrum. With the obtained results it is showed how the new kernel allows the refinement of the radiation field description in photon transport models. The extremely fast computation from the data base permits the reduction of the computational costs and allows the treatment of the bremsstrahlung contribution without the complexity of the coupled photon-electron problem.

## Appendix A - UMESTRAT files format

---

As shown in Chapter 1 the code UMESTRAT uses in its computation the codes MAXED [Reginatto, 1999] and GRAVEL [Matzke, 2002]. These codes can be run either interactively or by employing an input control file. The format of the MAXED and GRAVEL input file is shown in Fig A.1.

```

..\Sinp\phs_meas\Brass.phs
..\Sinp\rsp_detector\silicon.rsp
MXD_name
..\Sinp\def_meas\flat_fine.flu
0.2471000000000000E-02, 0.4328000000000000E-01
0.2471000000000000E-02, 0.4328000000000000E-01
0.1419685000000000E+01
20000
2, 1
1
0

```

Fig. A.1. Input file format of MAXED and GRAVEL.

The input file is characterized by the following format:

- Record 1: path/name of the measured spectrum file.
- Record 2: path/name of the DRF file.
- Record 3: name of the code output files.
- Record 4: path/name of the default spectrum files.
- Record 5: two real numbers representing the lower and the higher energies values of the measured spectrum energy range. These parameters are used to restrict the range of the pulse height data that is used for the unfolding. They must be in the same energy units as those used for the measured spectrum data.
- Record 6: two real numbers representing the lower and the higher energies values of the DRF energy range. These parameters are used to restrict the energy range of the response functions that are used for the unfolding (and therefore, it will also restrict the energy range of the solution spectrum). They must be in MeV, which are the energy units used for the DRF.
- Record 7: a real number representing the requested chi-square per degree of freedom used as built-in stop condition by the code. This parameter is used to select the final chi-squared per degree of freedom of the solution. The choice of this parameter requires some care. In particular, if the value is set too low, there might not be a solution consistent with the data.
- Record 8: an integer number representing the maximum number of iterative steps used as built-in stop condition by the code (in the GRAVEL input file it is present a second integer values representing the number of iterative steps for which GRAVEL show the intermediate result of the computation).



- Record 9: two integer values:
  - a. The first value allows the selection of the energy bin structure used for the unfolding. There are the following options for the energy structure used for the unfolding:
    - (1) Use a fine energy bin structure. In this case, the energy bin structure used for the unfolding is created by overlapping the bin structures of both the default spectrum and the response functions, so that there is a bin edge whenever either the default spectrum or the response functions have a bin edge.
    - (2) Use the energy bin structure of the default spectrum.
    - (3) Use the energy bin structure of the response functions.
  - b. The second values set the representation of the solution spectrum. There are the following options for the representation of the solution spectrum:
    - (1) The solution spectrum is expressed as  $f(E)/dE$ .
    - (2) The solution spectrum is expressed as  $E[f(E)/dE]$ .
- Record 10: an integer number representing the choice of scaling the default spectrum. There are the following options:
  - a. (0) Do not multiply the default spectrum with a scale factor.
  - b. (1) Multiply the default spectrum with a scale factor. This second choice allows the user to change the magnitude of the default spectrum, which is useful when the absolute magnitude of the default spectrum is not correct for the given data set.
- Record 11: an integer values representing the choice of changing the code scale factor (used only if you choose to scale the default spectrum). There are the following options:
  - a. (0) Use the code determined scale factor.
  - b. (1) Change the code determined scale factor.
- Record 12: a real number representing the user-defined scale factor (used Only if you choose to change the scale factor).

The codes MAXED and GRAVEL use as input the measured spectrum expressed in the '.phs' format. An example of the measured data file is show in Fig. A.2.

```
header
      2
      1      2
      1023      1023      49.728905
0.9376E-01,      0.1000E+01,      0.1000E+01
0.1423E+00,      0.1000E+01,      0.1000E+01
0.1908E+00,      0.1000E+01,      0.1000E+01
0.2393E+00,      0.1000E+01,      0.1000E+01
0.2878E+00,      0.1000E+01,      0.1000E+01
0.3364E+00,      0.1000E+01,      0.1000E+01
.....
.....
.....
0.4953E+02,      0.1000E+01,      0.1000E+01
0.4958E+02,      0.1000E+01,      0.1000E+01
0.4963E+02,      0.1000E+01,      0.1000E+01
0.4968E+02,      0.1000E+01,      0.1000E+01
```

Fig. A.2. Measured spectrum file format of MAXED and GRAVEL

The '.phs' format is as follows:

- Record 1: A header not used by the codes.
- Record 2: Two integer numbers:
  - a. The first one represents the form of the measured spectrum for which there are thee following options:
    - (1) The spectrum is expressed as  $f(E)/dE$ .
    - (2) The solution spectrum is expressed as  $f(E)$ .
    - (3) The solution spectrum is expressed as  $E[f(E)/dE]$ .
  - b. The second one represents the units of energy of the measured spectrum wich can be:
    - (1) eV
    - (2) MeV
    - (3) keV
- Record 3: three integer values and e real values representing respectively a dummy variable not used by the codes, the number of energy bins of the spectrum (repeated twice) and the highest energy bin edge.
- From Record 4 to the last record: three real numbers representing respectively the low energy bin edge, the value of the measured spectrum and its uncertainty.

The measured spectrum can be introduced in UMESTRAT also in the '.mca' format characterized by a file with three columns: the first one for the energy discretization, the second and the third one respectively for the value of the measured spectrum and its uncertainty.

The default spectrum file format (with the '.flu' extension) is the same as the '.phs' file format described before.

The codes MAXED and GRAVEL use as input the DRF matrix expressed in the ‘.rsp’ format. An example of the DRF data file is show in Fig. A.3.

```

0.27774E-01  1024  0.93758E-04  0.49777E-01
0.3935E-04  0.4593E-04  0.4744E-04  0.4699E-04  0.4588E-04  0.4456E-04  0.4320E-04
0.4180E-04  0.4033E-04  0.3879E-04  0.3723E-04  0.3578E-04  0.3453E-04  0.3354E-04
0.3269E-04  0.3176E-04  0.3058E-04  0.2917E-04  0.2775E-04  0.2644E-04  0.2524E-04
0.2409E-04  0.2296E-04  0.2194E-04  0.2121E-04  0.2090E-04  0.2091E-04  0.2106E-04
0.2139E-04  0.2202E-04  0.2289E-04  0.2380E-04  0.2464E-04  0.2551E-04  0.2658E-04
0.2789E-04  0.2926E-04  0.3043E-04  0.3126E-04  0.3175E-04  0.3206E-04  0.3233E-04
0.3265E-04  0.3302E-04  0.3331E-04  0.3346E-04  0.3351E-04  0.3346E-04  0.3325E-04
0.3273E-04  0.3173E-04  0.3014E-04  0.2801E-04  0.2554E-04  0.2297E-04  0.2051E-04
.....
.....
.....

```

Fig. A.3. DRF file format of MAXED and GRAVEL.

The ‘.rsp’ format is as follows:

- Record 1: a real number representing the width of the “measurement channels” chosen for the response functions calculation (in units of MeV) (real number). All “measurement channels” must be of the same energy width.
- Record 2: three real numbers and an integer value representing:
  - a. The energy of the incident particle (in units of MeV) (real number).
  - b. The number of “measurement channels” in the response function that were calculated for an incident particle with this particular energy (integer number).
  - c. The lowest energy bin edges (real number).
  - d. The highest energy bin edges (real number).
- Record 3: The response of each of the “measurement channels”, in ascending order (1,2,3,...all the way to the last “measurement channel”)

The structure of records 2 and 3 is repeated for all energies of the incident particle. Both GRAVEL and MAXED generate the output file using a ‘.flu’ extension.

The code UMESTRAT allows the salvage of an input file which can be load in every moment to resume a computation. This file is saved with the '.ume' extension. An example of the DRF data file is show in Fig. A.4.

```

      1
0.0000000000000000E+000  0.0000000000000000E+000
no_mca_file
Brass.phs
Amp_Brass.phs
  1.0000000000000000
silicon.rsp
      2000
      1
GRV_name
  1.4196850000000000
  7.84757019374785
      20000
MXD_name
def_MXD_name.flu
      2
  2.4710000000000000E-003
  4.3280000000000000E-002
  9.3758000000000001E-005
  4.9777000000000000E-002
  1.4198112000000000
  7.84791898286317
UME_name
  1.3839972000000000
  7.74830696559327
      1
  1.4196850000000000
  230.526881720430

```

Fig. A.4. UMESTRAT input file format.

The '.ume' format is as follows:

- Record 1 an integer value set equal to the measured spectrum file extensions (1 for the .phs file; 2 for the .mca file)
- Record 2 two real numbers set equal to the calibration parameters used to convert the measured spectrum from the '.mca' file format to the '.phs' file format.

- Record 3 the name of the “.mca” measured file (no\_mca\_file is shown if no “.mca” measured spectrum was used in the computation)
- Record 4 the name of the “.phs” measured file
- Record 5 the name of the “.phs” measured file in which the count’s standard deviations are modified by the amplification factor
- Record 6 the used amplification factor
- Record 7 the name of the file with the response function
- Record 8 the number of iterations used in the “Chi-Square” tab for the GRAVEL computation
- Record 9 the number of intermediate step iterations used in the “Chi-Square” tab for the GRAVEL computation
- Record 10 the name of the GRAVEL output files
- Record 11 the chi-square per degree of freedom value obtained in the tab “Chi-Square”
- Record 12 the mean relative error obtained in the tab “Chi-Square”
- Record 13 the number of iterations used in the tab “Default Spectrum” for the MAXED computation
- Record 14 the name of the MAXED output files
- Record 15 the name of the file with the obtained well shaped default spectrum
- Record 16 an integer value which show if the default spectrum was computed or loaded (1 if the default spectrum was loaded; 2 if the default spectrum was computed)
- Record 17 a real number equal to lowest energy of the measured data. This parameter is used to restrict the energy range of the measured data that is used for the unfolding.
- Record 18 a real number equal to highest energy of the measured data. This parameter is used to restrict the energy range of the measured data that is used for the unfolding.
- Record 19 a real number equal to lowest energy of the response functions used for unfolding. This parameter is used to restrict the energy range of the response functions that is used for the unfolding
- Record 20 a real number equal to highest energy of the response functions used for unfolding. This parameter is used to restrict the energy range of the response functions that is used for the unfolding
- Record 21 the chi-square per degree of freedom value obtained in the tab “Default Spectrum”
- Record 22 the mean relative error obtained in the tab “Default Spectrum”
- Record 23 the name of the UMESTRAT output files
- Record 24 the chi-square per degree of freedom value obtained in the tab “Unfolding MAXED”
- Record 25 the mean relative error obtained in the tab “Unfolding MAXED”

- Record 26 an integer value which show if the UMESTRAT unfolded spectrum was computed by using the chi-square per degree of freedom computed in the tab “Chi-Square” (1) or a freely chosen chi-square per degree of freedom (2)
- Record 27 the chi-square per degree of freedom value used for the UMESTRAT computation



# References

---

- [Agarwal, 1991] Agarwal, B.K. (1991), X-ray spectroscopy, Second Edition. Springer-Verlag.
- [Bearden, 1967] Bearden, J.A. (1967), X-ray wavelengths. *Rev. Mod. Phys.* 39(1):78-124. doi:10.1103/RevModPhys.39.78.
- [Berger, 1987] Berger, M.J. and Hubbell, J.H. (1987), XCOM: Photon Cross Sections on a Personal Computer. Report NBSIR 87-3597 (National Bureau of Standards, Gaithersburg, MD).
- [Bethe, 1934] Bethe, H.A. and Heitler, W. (1934), On the Stopping of Fast Particles and on the Creation of Positive Electrons. *Proc. R. Soc.* 146(A):83-112. doi:10.1098/rspa.1934.0140.
- [Biggs, 1975] Biggs, F.; Mendelsohn, L.B. and Mann, J.B. (1975), Hartree-Fock Compton profiles for the elements. *Atomic Data and Nuclear Data Tables* 16:210-309. doi:10.1016/0092-640X(75)90030-3.
- [Bishop, 1969] Bishop, H.E. and Riviere, J.C. (1969), Estimates of the Efficiencies of Production and Detection of Electron-Excited Auger Emission. *J. Appl. Phys.* 40:1740. doi:10.1063/1.1657841.
- [Boltzmann, 1964] Boltzmann, L. (1964), *Lectures on Gas Theory* Tr. by Brush, S. G. University of California Press.
- [Bote, 2008]. Bote, D. and Salvat, F. (2008), Calculations of inner-shell ionization by electron impact with the distorted-wave and plane-wave Born approximations. *Phys. Rev. A* 77,042701. doi:http://dx.doi.org/10.1103/PhysRevA.77.042701.



- [Byrd, 1995] Byrd, R.H.; Lu, P.; Nocedal, J. and Zhu, C. (1995), A limited memory algorithm for bound constrained optimization. *SIAM J. Sci. Comput.* 16(5):1190-1208. doi:10.1137/0916069.
- [Carlson, 1975] Carlson, T.A. (1975), *Photoelectron and Auger Spectroscopy*. (Plenum Press, New York and London).
- [Compton, 1923] Compton, A.H. (1923), A quantum theory of the scattering of X-rays by light elements. *Phys. Rev.* 21(5):483-502. doi:10.1103/PhysRev.21.483.
- [Cullen, 1989] Cullen, D.E.; Chen, M.H.; Hubbell, J.H.; Perkins, S.T.; Plechaty, E.F.; Rathkopf, J.A. and Scofield, J.H. (1989), *Tables and Graphs of Photon-Interaction Cross Sections from 10 eV to 100 GeV Derived from the LLNL Evaluated Photon Data Library (EPDL)*. Lawrence Livermore National Laboratory Report UCRL-5400, 6(A-B).
- [Cullen, 1997] Cullen, D.E.; Hubbell, J.H. and Kissel, L. (1997), *EPDL97 The evaluated photon data library '97 version*. Report UCRL-50400, 6:rev.5
- [Di Giulio, 2011] Di Giulio, E. (2011) *Applicazione del principio della massima entropia al processo di deconvoluzione della risposta del detector*. MA Thesis, Faculty of Engineering, University of Bologna.
- [de Laeter, 1988] de Laeter, J.R. (1988), Atomic weights of the elements. *J. Phys. Chem.* 17:1791-1793. doi:10.1063/1.555816.
- [Deslattes, 2003] Deslattes, R.D.; Kessler, E.G.; Indelicato, P.; de Billy, L.; Lindroth, E. and Anton, J. (2003), X-ray transition energies: new approach to a comprehensive evaluation. *Rev. Mod. Phys.* 75:35-99. doi:http://dx.doi.org/10.1103/RevModPhys.75.35.

- [DuMond, 1929] DuMond, J.E.W. (1929), Compton modified line structure and its relation to the electron theory of solid bodies. *Phys. Rev.* 33:643-658.
- [DuMond, 1930] DuMond, J.E.W. (1930), Breadth of Compton Modified Line. *Phys. Rev.* 36(1):146-147. doi:<http://dx.doi.org/10.1103/PhysRev.36.146>.
- [DuMond, 1933] DuMond, J.E.W. (1933), The linear momenta of electrons in atoms and in solid bodies as revealed by X-ray scattering. *Rev. Mod. Phys.* 5:1-33.
- [Ebel, 1971] Ebel, H.; Landler, F. and Dirschmid, H. (1971), Zur anregung charakterischer Rontgen-Strahlung durch Photoelektronen. *Z. Naturforsch.* 26(A):927-928.
- [Evans, 1955] Evans, R.D. (1955), *The Atomic Nucleus*. McGraw-Hill.
- [Evans, 1958] Evans, R.D. (1955), Compton effect. In *Handbuch der Physik*, Springer, Vol. 34:218.
- [Fernandez, 1989] Fernandez, J.E. (1989), XRF intensity in the frame of the transport theory. *X-ray Spectrom.* 18:271-279. doi:10.1002/xrs.1300180607.
- [Fernandez, 1992] Fernandez, J.E. (1992), Rayleigh and Compton scattering contributions to X-ray fluorescence intensity. *X-ray Spectrom.* 21(2):57-68. doi:10.1002/xrs.1300210204.
- [Fernandez, 2007-1] Fernandez, J.E. (2007), Multiple scattering of photons using the Boltzmann transport equation. *Nuc. Inst. Meth. Phys. Res.* 263(B1):7-21. doi:10.1016/j.nimb.2007.04.171.

- [Fernandez, 2007-2] Fernandez, J.E.; Scot, V.; Guidetti, A. and Badiali, M. (2007), Multiple scattering corrections for density profile unfolding from Compton scattering signals in reflection geometry. *Nuc. Instr. Meth. Phys. Res. A*580:77–80. doi:10.1016/j.nima.2007.05.018.
- [Fernandez, 2009] Fernandez, J.E. and Scot, V. (2009), Simulation of the detector response function with the code MCSHAPE. *Rad. Phys. Chem.* 78(10):882-887. doi:10.1016/j.radphyschem.2009.04.018.
- [Fernandez, 2013] Fernandez, J.E.; Scot, V.; Verardi, L. and Salvat, F. (2013), Electron contribution to photon transport in coupled photon-electron problems: inner-shell impact ionization correction to XRF. *X-ray Spectrom.* 42(4):189-196. doi:10.1002/xrs.2473.
- [Fernandez, 2014-1] Fernandez, J.E.; Scot, V. and Di Giulio, E. (2014), Spectrum unfolding in X-ray spectrometry using the maximum entropy method. *Rad. Phys. Chem.* 95:154-157. doi:10.1016/j.radphyschem.2012.12.026.
- [Fernandez, 2014-2] Fernandez, J.E.; Scot, V.; Verardi, L. and Salvat, F. (2014), Detailed calculation of inner-shell impact ionization to use in photon transport codes. *Rad. Phys. Chem.* 95:22-25. doi:10.1016/j.radphyschem.2012.12.030.
- [Fernandez, 2014-3] Fernandez, J.E.; Scot, V. and Sabbatucci, L. (2014), Modeling tool for detector resolution and incomplete charge collection. *X-ray Spectrom.* (In Press).
- [Haug, 1975] Haug, E. (1975), Bremsstrahlung and pair production in the field of free electrons. *Z. Naturforsch.* 30A:1099-1113.
- [Heitler, 1954] Heitler, W. (1954), *The Quantum Theory of Radiation*. Oxford Univ. Press.

- [Hirayama, 2005] Hirayama, H. and Namito, Y. (2005), Experimental data from measurements at the BL-14C, KEK. Private communication.
- [Hubbell, 1975] Hubbell, J.H.; Veigele, Wm.J.; Briggs, E.A.; Brown, R.T.; Cromer, D.T. and Howerton R.J. (1975), Atomic Form Factors, Incoherent Scattering Functions, and Photon Scattering Cross Sections. *J. Phys. Chem. Ref. Data.* 4(3):471-538. doi:10.1063/1.555554.
- [Hubbell, 1980] Hubbell, J.H.; Gimm, H.A. and Overbo, I. (1980), Pair, triplet, and total atomic cross sections (and mass attenuation coefficients) for 1 MeV-100 GeV photons in elements  $Z = 1$  to 100. *J. Phys. Chem. Ref. Data* 9:1023-1147. doi:10.1063/1.555629.
- [Hussein, 2011] Hussein, E.M.A. (2011), Computed radiation imaging: physics and mathematics of forward and inverse problem. Elsevier.
- [Kirkpatrick, 1945] Kirkpatrick, P. and Wiedmann, L. (1945), Theoretical continuous X-ray energy and polarization. *Phys. Rev.* 67:321-339. doi:10.1103/PhysRev.67.321.
- [Kissel, 1983] Kissel L.; Quarles, C.A. and Pratt, R.H. (1983), Shape functions for atomic-field bremsstrahlung from electrons of kinetic energy 1-500 keV on selected neutral atoms  $1 \leq Z \leq 92$ . *At. Data Nucl. Data Tables* 28:381-460. doi:10.1016/0092-640X(83)90001-3.
- [Klein, 1929] Klein, O. and Nishina, Y. (1929), Über die Streuung von Strahlung durch freie Elektronen nach der neuen relativistischen Quantendynamik von Dirac. *Z. Phys.* 52(11-12):853-869. doi:10.1007/BF01366453.

- [Koch, 1959] Koch, H.W. and Motz, J.W. (1959), Bremsstrahlung cross-section formulas and related data. *Rev. Mod. Phys.* 31:920-955. doi:<http://dx.doi.org/10.1103/RevModPhys.31.920>.
- [Knoll, 2000] Knoll, G.F. (2000), Radiation detection and measurement, third edition. John Wiley & Sons.
- [Matzke, 2002] Matzke, M. (2002), Propagation of uncertainties in unfolding procedures. *Nucl. Instrum. Meth. Phys. Res.* 476A:230-241. doi:10.1016/S0168-9002(01)01438-3.
- [Mayol, 1990] Mayol, R. and Salvat, F. (1990), Cross sections for K-shell ionization by electron impact. *J. Phys. B: At. Mol. Opt. Phys.* 23:2117-2130. doi:<http://dx.doi.org/10.1103/PhysRevA.86.042701>.
- [McElroy, 1967] McElroy, W.N.; Berg, S.; Crockett, T. and Hawkins, R.G. (1967), A computer-automated iterative method for neutron flux spectra determination by foil activation. U.S. Air Force Weapons Laboratory Report AFWL-TR-67-41, Kirkland AFB, NM.
- [McMaster, 1969] McMaster, W.H.; Kerr del Grande, N.; Mallett, J.H. and Hubbell, J.H. (1969), Compilation of X-ray cross-sections. Lawrence Livermore National Laboratory Report UCRL-50174, Sect. 2, Rev. 1.
- [Namito, 2000] Namito, Y.; Hirayama, H. and Ban, S. (2000), Improvements of low energy photon transport for EGS5. In: Proceedings of the Second International Workshop on EGS, KEK Proceedings 200-20:11-22.
- [Pavlinisky, 1994] Pavlinisky, G.V. and Dukhanin, A.Yu. (1994), Calculation of photo- and auger electron contribution to X-ray fluorescence excitation of elements with low atomic number. *X-Ray Spectrom.* 23:221-228. doi:10.1002/xrs.1300230507.

- [Pavlinsky, 2014] Pavlinsky, G.V. and Portnoy, A.Yu. (2014), The role of Compton scattering in the low-Z elements X-ray fluorescence formation. *X-ray Spectrom.* 43:118–121. doi:10.1002/xrs.2525.
- [Perkins, 1991] Perkins, S.T.; Cullen, D.E.; Chen, M.H.; Hubbell, J.H.; Rathkopf, J. and Scofield, J. (1991), Tables and graphs of atomic subshell and relaxation data derived from the LLNL evaluated atomic data library (EADL).  $Z = 1-100$ . Report UCRL-50400 vol. 30 (Lawrence Livermore National Laboratory, Livermore, CA).
- [Pratt, 1973] Pratt, R.H.; Ron, A. and Tseng, H.K. (1973), Atomic photoelectric effect above 10 keV. *Rev. Mod. Phys.* 45:273-325. Erratum: *ibid.* 45:663-664. doi:10.1103/RevModPhys.45.273.
- [Pratt, 1977] Pratt, R.H.; Tseng, H.K.; Lee, C.M. and Kissel, L. (1977), Bremsstrahlung energy spectra from electrons of kinetic energy  $1 \text{ keV} \leq T_1 \leq 2000 \text{ keV}$  incident on neutral atoms  $2 \leq Z \leq 92$ . *At. Data Nucl. Data Tables* 20:175-209. Erratum: *ibid.* 26(1981):477-481. doi:10.1016/0092-640X(77)90045-6.
- [Press, 1996] Press, W.H.; Teukolsky, S.A.; Vetterling, W.T. and Flannery, B.P. (1996), *Numerical recipes in FORTRAN: the art of scientific computing*. Second edition. ISBN 0-521-43064-X.
- [Reginatto, 1999] Reginatto, M. and Godhagen, P. (1999), Maxed, a computer code for maximum entropy Deconvolution of multisphere neutron spectrometer data. *Health Phys.* 77:579-583. doi:10.1097/00004032-199911000-00012.
- [Reginatto, 2003] Reginatto, M. (2003), The “multi-channel” unfolding programs in the UMG package: MXD\_MC33 GRV\_MC33 and IQU\_MC33, UMG package version 3.3. Physikalisch Technische Bundesanstalt (PTB).
- [Ribberfors, 1975] Ribberfors, R. (1975), Relationship of the relativistic Compton to the momentum distribution of bound electron states. *Phys. Rev. B*, 12(6):2067-2074. doi:10.1103/PhysRevB.12.2067.

- [Saloman, 1988] Saloman, E.B.; Hubbell, J.H. and Scofield, J.H. (1988), X-ray attenuation cross sections for energies 100 eV to 100 keV and elements  $Z = 1$  to  $Z = 92$ . *At. Data Nucl. Data Tables* 38:1-197. doi:10.1016/0092-640X(88)90044-7.
- [Salvat, 2009] Salvat, F. and Fernandez-Varea, J.M. (2009), Overview of physical interaction models for photon and electron transport used in Monte Carlo codes. *Metrologia* 46(2):S112. doi:10.1088/0026-1394/46/2/S08.
- [Salvat, 2011] Salvat, F.; Fernández-Varea, J.M. and Sempau J. (2011), PENELOPE-2011, a code system for Monte Carlo simulation of electron and photon transport. *NEA Data Bank NEA/NSC/DOC(2011)5*, OECD.
- [Scofield, 1973] Scofield, J.H. (1973), Theoretical photoionization cross sections from 1 to 1500 keV. Lawrence Livermore National Laboratory Rep. UCRL-51326. doi:10.2172/4545040.
- [Seltzer, 1985] Seltzer, S.M. and Berger, M.J. (1985), Bremsstrahlung spectra from electron interactions with screened atomic nuclei and orbital electrons. *Nucl. Instrum. Meth.* B12:95-134. doi:10.1016/0168-583X(85)90707-4.
- [Seltzer, 1986] Seltzer S.M. and Berger, M.J. (1986), Bremsstrahlung energy spectra from electrons with kinetic energy 1 keV-10 GeV incident on screened nuclei and orbital electrons of neutral atoms with  $Z = 1-100$ . *At. Data Nucl. Data Tables* 35:345-418. doi:10.1016/0092-640X(86)90014-8.
- [Smith, 1975] Smith, Jr.V.H.; Thakkar, A.J. and Chapman, D.C. (1975), A new analytical approximation to atomic incoherent X-ray scattering intensities, *Acta Cryst.* A31:391-392. doi:10.1107/S056773947500085X.
- [Statham, 1976] Statham, P.J. (1976), The generation, absorption and anisotropy of thick target bremsstrahlung and the implications for quantitative energy dispersive analysis. *X-Ray Spectrom.* 5:154-168. doi:10.1002/xrs.1300050310.

- [Stoev, 1991] Stoev, K.N. (1991), Theoretical calculation of secondary X-ray fluorescence due to Compton electrons. *J. Phys. D: Appl. Phys.* 25:131-138. doi:10.1088/0022-3727/25/2/001.
- [Stutz, 2014] Stutz, G.E. (2014), Compton scattering cross section for inner-shell electrons in the relativistic impulse approximation. *Nucl. Instr. Meth. B.* 319:8-16. doi:10.1016/j.nimb.2013.11.001.
- [Thomson, 1903] Thomson, J.J. (1903), *Conduction of electricity through gasses*. Second Edition. Cambridge At the University Press.
- [Tsai, 1974] Tsai, Y.S. (1974), Pair production and bremsstrahlung of charged leptons. *Rev. Mod. Phys.* 46(4):815-851. doi:10.1103/RevModPhys.46.815.
- [Van Grieken, 2001] Van Grieken, R.E. and Markowicz, A.A. (2001), *Handbook of X-ray spectrometry*, Second Edition. CRC Press.
- [Veigele, 1966] Veigele, W.J.; Tracy, P.T. and Henry, E.M. (1966), Compton effect and electron binding. *Am. J. Phys.* 34:1116-1121. doi:10.1119/1.1972521.
- [Waller, 1929] Waller, I. and Hartree, D.R. (1929), On the intensity of total scattering by X-ray. *Proc. Roy. Soc. A.* 124:119-142.





# Other Ph.D. activities

---

## Seminaries

Progetto ed Utilizzo del Combustibile Nucleare, Leveque, J.P., University of Bologna (Italy).

Ventures in Radiation Dosimetry, Bradley, D., University of Bologna (Italy).

## Workshops

Advanced XRD Application, University of Bologna.

Joint ITCP-IAEA Workshop on Advanced Synchrotron Radiation Based X-ray Spectrometry Technique, Abdus Salam International Centre for Theoretical Physics (ICTP), Trieste (Italy).

## Conferences

9<sup>th</sup> International Topical Meeting on Industrial Radiation and Radioisotope Measurement Applications (IRRMA-9), Valencia (Spain).

15<sup>th</sup> European Conference on X-Ray Spectrometry (EXRS-2014), Bologna (Italy).

14th European Conference on X-Ray Spectrometry (EXRS-2012), Wien (Austria).

## Courses

Tecniche di ottimizzazione in ambiente HPC, CINECA, Bologna (Italy).

Introduzione al Fortran 90, CINECA, Bologna (Italy).

Introduzione alla programmazione OpenMP, CINECA, Bologna (Italy).

21th Summer School on Parallel Computing, CINECA, Bologna (Italy).

Scintillation Detector, Sherer, U., University of Bologna (Italy).

Availability function and Thermodynamic efficiency, Alves, L.S. de B., University of Bologna (Italy).

Testing the stability of a fluid system, Zanchini, E., University of Bologna (Italy).

Use of a symbolic mathematical code for convection-diffusion problem, Sphaier, L.A., University of Bologna (Italy).

Metodi di controllo ed ottimizzazione, Manservigi, S., University of Bologna (Italy).

Modellazione numerica con COMSOL Multiphysics: esempi applicativi, Lazzari, S., University of Bologna (Italy).

Equazioni cinetiche e fondamenti statistici del trasporto, Mostacci, D., and Molinari, V., University of Bologna (Italy).

Fisica dei raggi X e luce di sincrotrone, Boscherini, F., University of Bologna (Italy).

Fisica della materia e della radiazione, Boscherini, F., University of Bologna (Italy).

10th Advanced School on Parallel Computing, CINECA, Bologna (Italy).

## Publications

“Evaluation of Bremsstrahlung Contribution to Photon Transport in Coupled Photon-Electron Problems”, J.E. Fernandez, V. Scot, E. Di Giulio, F. Salvat, Radiation Physics and Chemistry (submitted 2014).

“Bremsstrahlung Contribution to Photon Transport in Coupled Photon-Electron Problems”, J.E. Fernandez, V. Scot, E. Di Giulio, F. Salvat, X-Ray Spectrometry (submitted 2014).

“Improvement of the detector resolution in x-ray spectrometry by using the maximum entropy method”, J.E. Fernandez, V. Scot, E. Di Giulio, L. Sabbatucci, Radiation Physics and Chemistry (submitted 2014).

“Spectrum unfolding in X-ray spectrometry using the maximum entropy method” J.E. Fernandez, V. Scot, and E. Di Giulio, (2014), Radiation Physics and Chemistry, Volume 95, 154-157, ISSN 0969-806 X.

## Other activities

Member of the local organizing committee of the European Conference on X-Ray Spectrometry (EXRS-2014), Bologna (Italy).



# Acknowledgements

---

I would like to express my special appreciation and thanks to my tutor Professor Jorge Eduardo Fernandez for encouraging my research with patience and perseverance and for allowing me to grow in my work experiences. I would also like to thank my colleagues Ing. Viviana Scot and Ing. Lorenzo Sabbatucci for the precious support given to this work. A special thanks to my family for all of the sacrifices made on my behalf.